

# Electromagnetic Drift Waves

IN A U G U R A L D I S S E R T A T I O N

zur

Erlangung des akademischen Grades eines

doctor rerum naturalium (Dr. rer. nat.)

an der Mathematisch-Naturwissenschaftlichen Fakultät

der

Ernst-Moritz-Arndt-Universität Greifswald

vorgelegt von

Stefan Ullrich

geboren am 26.09.1978

in Greifswald

Greifswald, im November 2010

Dekan:

Prof. Dr. K. Fesser

1. Gutachter:

Prof. Dr. Thomas Klinger

Tag der Promotion: 27.04.2011

# Abstract

In the rf-plasma of the linear magnetized VINETA experiment, different types of low-frequency waves are observed. The emphasis in this work is on the interaction mechanism between drift waves on the one and kinetic Alfvén waves on the other hand. In the peaked density profile of the plasma column generated by a helicon source with the typical parameters  $n_0 = 5 \cdot 10^{18} \text{ m}^{-3}$  and  $T_e = 2 \text{ eV}$ , drift waves occur as modulation of the plasma density up to 10 %. As gradient driven instability, they draw their energy from the radial density gradients. Alfvén waves as magnetic field fluctuations are stable in the present configuration. They are launched by a magnetic excitation antenna generating a perturbation of the ambient magnetic field of  $\tilde{b}/B_0 \approx 1 \%$ . Parallel conduction currents in the plasma — which are carried by electrons — are common to both wave phenomena. They generate a fluctuating magnetic field which is used to detect both wave types. A  $\tilde{B}$ -detector as standard diagnostic tool is used for this purpose. The challenge are the small induced voltages due to the low wave frequency range of  $f = 1 \dots 50 \text{ kHz}$  in the environment of a fluctuating plasma potential that is several orders of magnitude higher. To record these signals without significant electrostatic pickup, a fully shielded detector design is developed with an integrated amplifier close to the probe head.

Mounted on different positioning systems, such  $\tilde{B}$ -probes are used to characterize both wave phenomena. For Alfvén waves, the dispersion relation is recorded experimentally. It is found to be in good agreement with the prediction of the Hall-MHD theory with included resistive term, accounting for the cold collisional plasma of VINETA. The fluctuating magnetic field pattern — which is subsequently inverted with Ampère’s law — is recorded with azimuthal scans. The resulting current density is concentrated in current filaments, which are helically twisted. For the unstable drift waves, similar investigations are done with simultaneously recorded density fluctuations. In the azimuthal plane, the locations of the parallel current filaments and the fluctuating density are found to be in phase, which supports the predicted drive of parallel currents by pressure gradients. A mutual influence of the two wave types is observed in an interaction experiment. Assuming parallel currents as coupling quantity, an interpretation of the experimental findings is given based on the linear theory of drift waves.

## Zusammenfassung

Im rf-Plasma des linear magnetisierten VINETA-Experiments werden verschiedene Arten von Wellen beobachtet. Der Schwerpunkt dieser Arbeit liegt auf der Wechselwirkung zwischen instabilen Driftwellen auf der einen und stabilen Alfvénwellen auf der anderen Seite. Die Plasmadichte der Helikonentladung ist axialsymmetrisch konzentriert mit typischen Werten von  $n_0 = 5 \cdot 10^{18} \text{ m}^{-3}$  und  $T_e = 2 \text{ eV}$ . Unter diesen Bedingungen treten Driftwellen als Modulation der Plasmadichte bis zu 10 % auf. Als gradientgetriebene Instabilität beziehen Driftwellen im VINETA-Plasma ihre Energie aus dem radialen Dichtegradienten. Alfvénwellen werden als Fluktuationen des Magnetfeldes beobachtet und sind in der vorliegenden Entladung stabil. Sie werden angeregt durch eine magnetische Antenne, welche Störungen von bis zu  $\tilde{b}/B_0 \approx 1\%$  erzeugt. Als gemeinsame Eigenschaft sind beide Wellenphänomene mit parallelen Plasmaströmen verbunden, die durch Elektronen getragen werden. Diese Ströme erzeugen ein fluktuierendes Magnetfeld, das verwendet wird, um beide Wellenarten zu diagnostizieren. Dafür wird eine  $\dot{B}$ -Sonde verwendet. Eine Herausforderung sind die kleinen induzierten Spannungen aufgrund des niedrigen Frequenzbereiches der Wellen von  $f = 1 \dots 50 \text{ kHz}$  in der Umgebung eines um mehrere Größenordnungen stärker fluktuierenden Plasmapotenzials. Um diese Signale ohne nennenswerte elektrostatische Störungen aufzunehmen, wurde ein vollständig geschirmter  $\dot{B}$ -Sensor entwickelt mit einem integrierten Verstärker nahe am Sondenkopf.

Mit einer solchen Sonde, die mit verschiedenen Positionierungssystemen verfahren werden kann, wurden beide Wellenphänomene untersucht. Für Alfvénwellen ist die Dispersionsrelation experimentell bestimmt worden. Es wurde eine gute Übereinstimmung mit der resistiven Hall-MHD-Theorie gefunden. Der Widerstandsterm ist essentiell für die Beschreibung des kalten stoßbehafteten Plasmas in VINETA. Das Wellenmagnetfeld wurde mit azimuthalen Scans vermessen und anschließend mittels Ampèreschen Gesetzes der parallele Strom berechnet. Es resultieren zwei Stromfilamente, die helikal miteinander verdreht sind. Für die selbsterregt auftretenden Driftwellen wurden ähnliche Untersuchungen durchgeführt mit zusätzlich aufgezeichneten Dichtefluktuationen. Die Phase zwischen den parallelen Stromfilamenten und den Dichtemaxima konnte in der azimuthalen Ebene nahe Null bestimmt werden, was den durch die Theorie vorhergesagten Stromtrieb durch parallele Dichtegradienten stützt. In einem Wechselwirkungsexperiment konnte die gegenseitige Beeinflussung beider Wellentypen beobachtet werden. Als Kopplungsgröße werden die parallelen Ströme vorgeschlagen, die mit beiden Wellentypen einhergehen. Die präsentierte Interpretation der experimentellen Resultate basiert auf der linearen Driftwellentheorie.

# Contents

<b>Abstract</b>	<b>i</b>
<b>Zusammenfassung</b>	<b>ii</b>
<b>1 Introduction</b>	<b>1</b>
<b>2 Diagnostics and signal processing</b>	<b>6</b>
2.1 The VINETA experiment . . . . .	6
2.2 Magnetic probes . . . . .	7
2.2.1 Requirements for magnetic probes . . . . .	8
2.2.2 Available sensor types . . . . .	9
2.2.3 Design of the $\dot{B}$ -detector . . . . .	14
2.2.4 Calibration of the $\dot{B}$ -probe . . . . .	17
2.2.5 Test of the $\dot{B}$ -detector . . . . .	20
2.3 Langmuir probes . . . . .	22
2.4 Interferometer . . . . .	25
2.5 Alfvén wave excitation and detection . . . . .	27
2.5.1 Excitation antenna . . . . .	28
2.5.2 Low-frequency drive . . . . .	29
2.5.3 High frequency drive . . . . .	31
2.6 Wave field reconstruction and signal processing . . . . .	32
<b>3 Theoretic background</b>	<b>37</b>
3.1 Alfvén waves . . . . .	37
3.1.1 Ideal MHD . . . . .	37
3.1.2 MHD with Hall term . . . . .	40
3.1.3 MHD with Hall term and resistivity . . . . .	42
3.1.4 Spatial structure of Alfvén waves . . . . .	45
3.1.5 Shear AW as solution of Hall-MDH model . . . . .	49
3.1.6 Shear and fast AW as solution of Hall-MHD model . . . . .	50
3.2 Drift instability . . . . .	51

3.2.1	Drift wave instability mechanism . . . . .	52
3.2.2	Basic equations of two-fluid theory . . . . .	53
3.2.3	The Hasegawa-Wakatani model . . . . .	56
3.2.4	Nonlinear model: Hasegawa-Mima . . . . .	59
<b>4</b>	<b>Experimental Alfvén wave investigations</b>	<b>62</b>
4.1	Basic properties of Alfvén waves in VINETA . . . . .	62
4.1.1	Spatial field pattern of Alfvén waves . . . . .	62
4.1.2	Propagation parallel to the magnetic field . . . . .	64
4.1.3	Alfvén wave dispersion relation . . . . .	65
4.1.4	Influence of $B_0$ on phase velocity . . . . .	67
4.1.5	Influence of $n_e$ on phase velocity . . . . .	68
4.1.6	Influence of ion mass on phase velocity . . . . .	69
4.2	Currents of Alfvén waves . . . . .	71
4.2.1	Currents parallel and perpendicular to $B_0$ . . . . .	71
4.2.2	Idealization: parallel current filaments . . . . .	73
4.2.3	Explicit time dependence of the current . . . . .	74
4.2.4	Convective derivative for a moving current filament . . . . .	76
4.2.5	3D-current system of a shear Alfvén wave . . . . .	79
4.3	Rotating current patterns . . . . .	80
4.3.1	Measurement of parallel currents . . . . .	80
4.3.2	Rotational decomposition . . . . .	82
4.3.3	Polarization decomposition . . . . .	86
<b>5</b>	<b>Experimental drift wave investigations</b>	<b>92</b>
5.1	Basic properties of drift waves in VINETA . . . . .	92
5.2	Parallel currents of drift waves . . . . .	94
5.3	Interaction of drift waves and Alfvén waves . . . . .	96
5.3.1	Observation of drift-Alfvén wave interaction . . . . .	98
5.3.2	Interpretation of the observations . . . . .	104
<b>6</b>	<b>Summary and conclusions</b>	<b>107</b>
<b>A</b>	<b>Dispersion relation for resistive Alfvén waves</b>	<b>110</b>
	<b>Bibliography</b>	<b>113</b>
	<b>List of Publications</b>	<b>124</b>

# Chapter 1

## Introduction

Plasmas support a whole wealth of waves and instabilities. In many situations it is possible to treat the plasma components — electrons and ions — as intersecting fluids [1, p.3]. Each of those individual fluid components support wave phenomena, similar to neutral fluids or gases [2]. In a plasma additionally the condition of quasi neutrality has to be satisfied [3]. This condition states that there can be no accumulation of net charge at any location in the plasma. Hence, there can be electric currents in the plasma with the condition that the current density divergence of different currents balance each other at any point

$$\sum n \nabla j_n = 0 \quad n - \text{plasma components} \quad (1.1)$$

Currents generate magnetic fields which in turn influence the plasma as a conducting fluid. This is the main difference of plasma dynamics compared to neutral fluid dynamics. In the latter case, energy is transferred between adjacent fluid cells by viscosity only. Plasma dynamics are characterized by a long range interaction via a collective response to electromagnetic fields.

Large-scale interactions in plasmas are observed e.g. in space plasmas. An example is the ejection of matter from the sun, known as prominences or solar flares [4]. A solar flare occurs, if the dipole magnetic field of a pair of sunspots links with the interstellar magnetic field. The energy release in this process is given by the magnetic field energy, in particular the plasma volume is accelerated away from the sun [5] and magnetic energy is transferred to kinetic energy. Another example of such energy transfer is the scenario for heating the sun's corona [6]. It involves Alfvén waves in the magnetized plasma near the sun [7], which are generated from below the sun's surface and dissipate their energy in the corona by resonant wave damping.

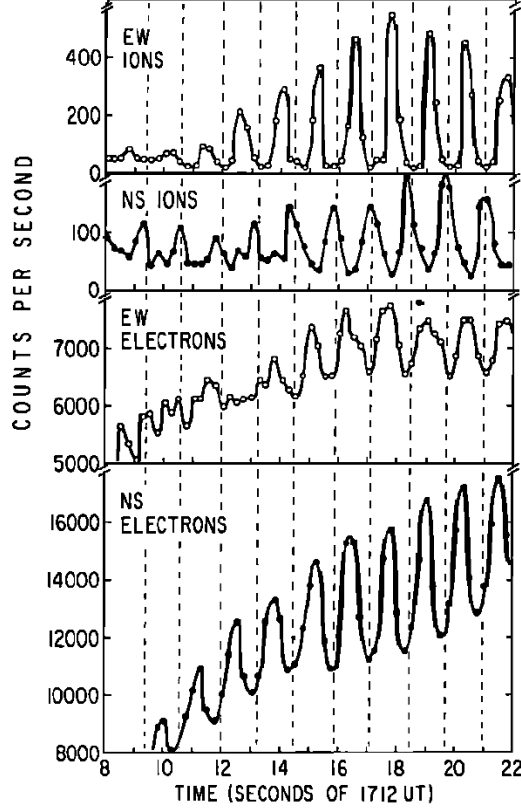


Figure 1.1: Shear Alfvén wave in earth magnetosphere taken from Ref.[8]. Data were recorded by energy analyzers for electrons and ions aboard the geostationary satellite ATS 6. Details are given in Ref.[9]. Simultaneous acquisition in North-South (NS) and East-West (EW) direction for the two species with analyzers gated to 30 eV yield the time resolved counting rates shown in the 4 diagrams.

Two frequency ranges are distinguished in magnetized plasmas. If alternating electromagnetic fields are applied to charged particles with periods much shorter than the gyration time, there will be no net displacement after one gyration period. Only if the periods of fluctuating fields are comparable or longer than the gyration period there will be a collective effect in terms of a resulting current. For the ions, this transition is quantitatively set by the ion-cyclotron frequency

$$\omega_{ci} = \frac{eB_0}{m_i} , \quad (1.2)$$

where  $B_0$  denotes the ambient magnetic field and  $m_i$  the ion mass. Plasma waves with frequencies up to the ion-cyclotron frequency involve both electron currents and ion currents. This class of plasma waves was predicted by Hannes Alfvén in 1942 [10]. Their ubiquitous role in space plasmas is addressed by Gekelman [11]. A nice measurement of shear Alfvén waves in a space plasma is shown in Fig. 1, taken from Ref. [8]. In this in-situ measurement, the time varying electron and ion fluxes were directly measured with particle detectors along (North-South) and across (East-West) the ambient magnetic field. The output signal was proportional to the electric current carried by the corresponding species. In the example shown above,

---

a coherent wave is observed at  $f = 0.75$  Hz, corresponding to  $2\pi f = 0.33\omega_{ci}$ . The fluctuation amplitude for ions is significantly larger in the perpendicular direction when compared to the parallel direction, opposite to the electron count. These findings directly correspond to the theoretically expected properties of shear Alfvén waves: The wave can exist up to  $\omega = \omega_{ci}$  and a parallel electron flux (mainly NS) is balanced by a perpendicular ion flux (mainly EW). The time series of the two fluxes are in phase owing to quasi-neutrality. The wavelength in the example is derived from the linear dispersion relation of shear Alfvén waves to  $\lambda = 2600$  km. Such long wave lengths would be difficult to handle in laboratory experiments, where the geometrical dimension is typically limited to just a few meters. In toroidal plasma experiments, however, Alfvén eigenmodes are observed due to the periodicity of the magnetic field topology with very long connection lengths [12].

Another wave phenomenon in the frequency range below the ion-cyclotron frequency are drift waves with some similarities in the processes involved. The main distinction between drift waves and Alfvén waves is the stability aspect. Drift waves are instabilities drawing energy from a density gradient, whereas Alfvén waves occur as damped waves in a homogeneously magnetized plasma. A recent example for drift waves in space plasmas is given by Sundkvist and Bale [13]. At the boundary between the low density plasma of the magnetosphere and the high density plasma of the solar wind, a density gradient forms in the so-called magnetosheath. The electrons escape from regions of increased plasma density parallel to the ambient magnetic field. The ions react to the resulting potential perturbation with currents perpendicular to the ambient magnetic field. As an instability the drift wave can enter a turbulent state [14]. By convecting plasma in regions with density gradients this leads to cross-field transport [15, 16]. It is crucial in fusion experiments, where turbulent drift-Alfvén waves are a possible source for the strong anomalous transport, which limits the heat isolation [17].

It is a challenge to complement measurements of naturally occurring low-frequency waves in space plasmas by experimental investigations in laboratory plasmas. Laboratory experiments allow for highly resolved spatio-temporal observation of all fluctuating wave quantities, in contrast to satellite or rocket measurements, which can probe the wave fields only along their trajectory. Additionally, in a laboratory environment it is possible to actively influence the wave under investigation. But how can a laboratory experiment be suitable for the large spatial scales of waves in space plasma? Cramer writes in his book:

*One of the greatest difficulties one encounters in trying to relate Alfvén waves in space to laboratory observations is the shocking difference in time and length scales. It is hard to believe that physics of wave propagation could be the same, but it is. [18, p.9]*

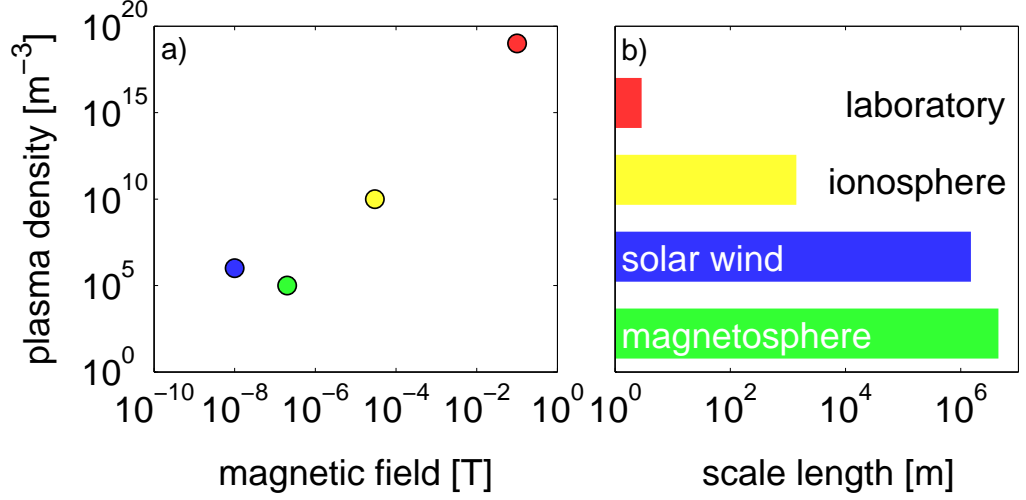


Figure 1.2: Four examples for plasmas from table 1.1 where Alfvén waves are observed. In (a) the different plasmas are shown in the parameter room spanned by the background magnetic field strength and the plasma density. Typical wave lengths of observed Alfvén waves are shown in (b).

The two important parameters making low-frequency wave phenomena accessible in laboratory-scale experiments are the ambient magnetic field  $B_0$  and the plasma density  $n$ . As seen in Fig. 1.2 (a) the two parameters span several orders of magnitudes in different plasmas where Alfvén waves are observed. The corresponding scale length in Fig. 1.2 (b) of Alfvén waves is decreased for increased ambient magnetic field  $B_0$  and increased plasma density  $n$ . Both parameters are chosen relatively high in the laboratory experiment VINETA, where the experiments of the present work are conducted. In this way, a spatial scale for low-frequency waves in the order of the machine length is achieved. The resulting time scales are still well accessible with standard data-acquisition techniques.

Alfvén waves must be excited with an appropriate setup. In Alfvén physics, magnetic field fluctuations and fluctuating currents are of major importance. Both quantities have been used in laboratory experiments to launch Alfvén waves [19, 20]. The fluctuating magnetic field associated with Alfvén waves can be measured with magnetic field sensors, in particular  $\vec{B}$ -probes [21]. If the wave field is recorded spatially resolved, the fluctuating currents can be reconstructed from the fluctuating magnetic field with Ampère’s law. Since for laboratory plasmas the Alfvén wave frequencies are in the kHz-range, the  $\vec{B}$ -probe has to be optimized to high sensitivity and good signal-to-noise ratio.

Low-frequency magnetic perturbations propagate in VINETA along the ambient mag-

---

Table 1.1: Typical spatial and temporal scales for Alfvén waves in different near-earth, space and laboratory plasmas. The plasma parameters density  $n$ , gas sort and ambient magnetic field  $B_0$  set the property of an Alfvén wave in terms of their velocity  $v_A$ , their period duration  $T$  and their wave length  $\lambda$ . For the three space plasma cases the density and the magnetic field are taken from [18, 22–24], the values for the laboratory plasma represent the situation in VINETA (see below).

region	$n$ [ $\text{m}^{-3}$ ]	gas	$B_0$ [T]	$v_A$ [m/s]	$T$ [s]	$\lambda$ [m]
ionosphere	$1 \cdot 10^{10}$	H	$30 \cdot 10^{-6}$	$6.6 \cdot 10^6$	$2.2 \cdot 10^{-3}$	$1.4 \cdot 10^3$
magnetosphere	$1 \cdot 10^5$	H	$200 \cdot 10^{-9}$	$1.4 \cdot 10^7$	$320 \cdot 10^{-3}$	$4.5 \cdot 10^6$
solar wind	$1 \cdot 10^6$	H	$10 \cdot 10^{-9}$	$2.2 \cdot 10^5$	6.7	$1.5 \cdot 10^6$
laboratory	$1 \cdot 10^{19}$	Ar	$100 \cdot 10^{-3}$	$1.1 \cdot 10^5$	$26 \cdot 10^{-6}$	2.9

---

netic field [25]. An issue addressed in this thesis is their proper identification as shear Alfvén waves. Evidence is found by comparing experimentally obtained dispersion relations with theory. Another issue is the precise characterization of the spatial structure of Alfvén waves in terms of the underlying current pattern. In conjunction with the corresponding current pattern of drift waves the interaction of both wave types will be discussed.

The present thesis is organized as follows: Chapter 2 gives an overview of the VINETA experiment and the used diagnostic systems. In particular, the wave excitation system for driving Alfvén waves and the development of a highly sensitive detector for the fluctuating magnetic field are presented. In chapter 3, the theoretical background for drift and Alfvén waves is given, with emphasis on the fluctuating currents of the two wave types. For Alfvén waves, a spatio-temporal description is presented based on a resistive Hall-magnetohydrodynamic model (MHD). The derived dispersion relation has two branches, one for shear and one for fast Alfvén waves. The experimental findings are compiled in chapter 4 for Alfvén waves and in chapter 5 for drift waves. The excited waves are characterized in terms of their dispersion relation and identified as Alfvén waves. For both drift and Alfvén waves, spatio-temporally resolved magnetic field fluctuations are recorded. From those the parallel component of the current density is derived. It is found to be located at similar spatial locations with comparable absolute values for both wave types. This finding motivates a coupling experiment for drift and Alfvén waves, discussed in the last section of chapter 5.

# Chapter 2

## Diagnostics and signal processing

### 2.1 The VINETA experiment

The experiments presented in this thesis are performed in the linear magnetized plasma of VINETA with a vessel length of 4.5 m and a diameter of 0.4 m. A schematic drawing is given in Fig. 2.1. The plasma is generated by a rf-helicon source [26–28]. This discharge type is based on the non-resonant absorption of helicon waves [29], where the absorption layer is predicted to be detached from the source region [30]. Helicon sources are extremely efficient: A few kilowatt are sufficient to sustain plasmas with densities  $n \gtrsim 10^{19} \text{ m}^{-3}$ . Therefore, this type of plasma source is widely used in low-temperature plasma physics [31, 32], in plasma processing [33], and in advanced plasma propulsion [34, 35]. However, the specific mechanism of plasma heating using helicon waves is still subject of intense discussion [36, 37]. At VINETA, a  $m = 1$ -antenna [38] is used for helicon wave excitation. The antenna, located at one end of the vacuum chamber, is placed on a pyrex extension with a length of 0.5 m and a diameter of 0.1 m. The input power is generated by a rf-amplifier, capable of delivering up to 6 kW at the used frequency of 13.56 MHz. The amplifier is connected to the antenna via a  $\pi$ -matching network. The helicon discharge mode is typically reached at power levels above 1.8 kW. At lower power levels, the discharge is in the capacitive and in the inductive mode respectively [39].

The ambient magnetic field  $B_0$  of VINETA is generated by 33 magnetic coils, powered by 4 DC-power supplies. They allow operation at any level in the range  $B_0 = 0 \dots 103 \text{ mT}$ . Three additional coils in the antenna region allow switching between fringed magnetic field lines and homogeneous field lines at the helicon source. If turned off, the magnetic field has a gradient in the source region. Due to magnetic mapping, the plasma is then concentrated in the center of the vessel [40].

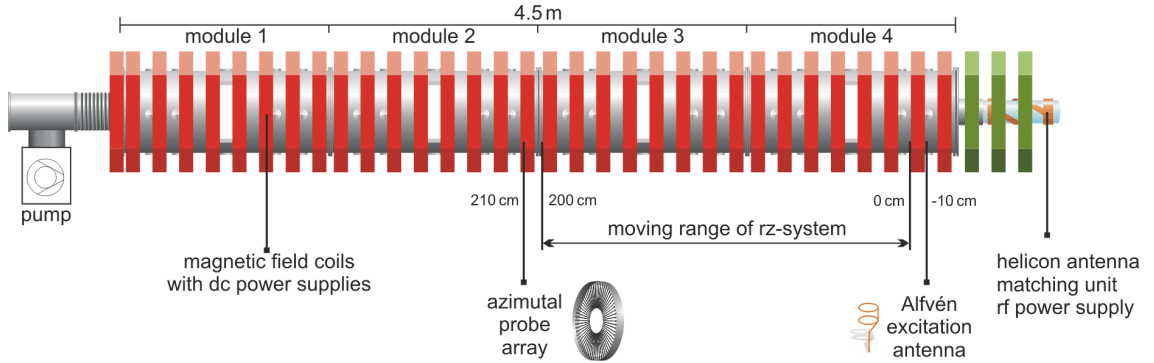


Figure 2.1: Schematic view of the VINETA experiment including the positions of the used systems for wave excitation and detection.

The configuration with homogenous source magnetic field is used for all presented experiments.

Three types of positioning systems for the VINETA experiment provide access to the plasma at different spatial positions. Each of those systems is equipped with a standard mount for the used probes with a couple of integrated feedthrough lines. The simplest positioning system is an **r**-system, capable of moving horizontally corresponding to the radial direction. Two independent **xy**-systems allow to access azimuthal planes of the cylindrical plasma. The labeling as ‘**xy**’- instead of ‘**rφ**’-system corresponds to the cartesian directions of horizontal and vertical movement of these systems. Finally, an **rz**-system which is mounted inside the vessel gives access to the radial-axial plane in VINETA.

Complementary to recording data by repositioning one probe, arrays of probes can be used. For VINETA an azimuthal 1D-array consisting of 64 Langmuir probes is available. It spans the azimuthal direction  $\theta = 0 \dots 2\pi$  at a predefined radius  $r$  and is capable of detecting the fluctuating plasma density [41]. All channels are simultaneously recorded with a 64-channel data acquisition system with a digitizing rate of up to 1.25 MHz.

## 2.2 Magnetic probes

For the detection of magnetic fluctuations in VINETA, a probe was developed and optimized to investigate coherent drift waves and drift wave turbulence on the one hand and Alfvén waves on the other hand. A salient issue was the possibility to record the three magnetic field components independently from each other with reasonable crosstalk attenuation.

### 2.2.1 Requirements for magnetic probes

There are two main design criteria for a magnetic probe: the frequency range of operation and the sensitivity in terms of minimum detectable field strength  $|\vec{b}|$ . The physical entity under investigation defines the two parameters as target-setting of the probe design. Drift waves in VINETA occur as coherent fluctuations of plasma parameters in the frequency range  $f = 1 \dots 10$  kHz, depending on their azimuthal mode number [42]. In the case of drift turbulence [43], the upper frequency limit is about 50 kHz. Alfvén waves (AW) occur as shear and fast AW. They exist in the frequency range up to the ion-cyclotron frequency

$$\omega_{ci} = qB_0/m_i \quad , \quad (2.1)$$

which scales linearly with the ambient magnetic field  $B_0$  and inversely with the ion mass  $m_i$ . For the used gases argon, helium, and hydrogen, the maximum frequencies are  $f_{ci} \leq 40$  kHz, 400 kHz and 1.6 MHz, respectively. Thus, the probe needs to have a frequency response of  $f = 1 \text{ kHz} \dots 2 \text{ MHz}$ . Fluctuating magnetic fields will be labeled with small letter  $b$  in the following. For drift waves, the expected fluctuation amplitude  $b_\perp$ , defining the needed probe sensitivity, can be estimated as follows. Since the plasma is quasineutral, the divergence of perpendicular and parallel current vector components balance:  $\nabla_\perp j_\perp = \nabla_\parallel j_\parallel$ . For drift waves, the perpendicular currents are ion polarization currents

$$j_\perp = j_{\text{pol}} = nm_i \frac{\dot{E}_\perp}{B_0^2} \quad , \quad (2.2)$$

where  $E_\perp$  is the wave electric field. The parallel current component  $j_\parallel$  is the response current to a density perturbation carried by electrons. The derivatives in the balance can be approximated using the characteristic spatial and temporal scales, as

$$\partial_t E \approx \omega E \quad \partial_\perp j_\perp \approx \frac{j_\perp}{\rho_s} \quad \partial_\parallel j_\parallel \approx \frac{j_\parallel}{\lambda_\parallel} \quad , \quad (2.3)$$

where  $\omega$  is the drift wave frequency,  $\rho_s$  the drift scale, defined below in (3.37), and  $\lambda_\parallel$  is a typical parallel scale. Thus, the current divergence balance reads to be

$$\frac{j_\parallel}{\lambda_\parallel} = \frac{nm_i}{\rho_s B_0} \omega \frac{\tilde{\phi}}{\rho_s} \quad , \quad (2.4)$$

$\tilde{\phi}$  denotes the fluctuating plasma potential. Using Ampère's law  $\mu_0 \vec{j} = \vec{\nabla} \times \vec{b} \approx \vec{b}/\rho_s$  and the linearized Boltzmann relation  $\tilde{n} = n_0 e \tilde{\phi} / k_B T_e$ , (2.4) can be rearranged to

$$\frac{b}{B_0} \approx \frac{\omega \lambda_\parallel}{\omega_{ci} \rho_s} \beta \frac{\tilde{n}}{n_0} \quad . \quad (2.5)$$

Here,  $\beta = n_0 k_B T_e / (B_0^2 / 2\mu_0)$  is introduced as ratio of kinetic to magnetic pressure. (2.5) finally allows to estimate the relative magnetic fluctuation amplitude  $\tilde{b}/B_0$ . The plasma- $\beta$  in VINETA has a typical value of  $5 \cdot 10^{-4}$  and the relative fluctuation amplitude of drift waves is typically  $\tilde{n}/n_0 \leq 10\%$ . The first factor in (2.5) is of order unity according to drift ordering (cf. Eq. 3.39). Thus, the relative magnetic fluctuation amplitude is estimated to be  $5 \cdot 10^{-5}$ , which corresponds to an absolute value of  $b = 5 \mu\text{T}$  for an ambient magnetic field of 100 mT. Recent investigations in the torsatron TJ-K with similar plasma parameters as in VINETA have shown similar magnetic fluctuation amplitudes of  $b/B_0 \approx 10^{-6}$  [44].

For Alfvén waves, the magnetic fluctuation amplitude is given by the wave excitation amplitude. The setup used for the experiments can generate perpendicular perturbations up to  $b = 1 \text{ mT}$ . Alfvén waves are damped in the collision-dominated plasma of VINETA with typical damping lengths in the range of 0.6 m [25]. This results in an attenuation of the launched wave to  $b = 1.3 \mu\text{T}$  over a length of 4 m.

To measure the fluctuations in the range of a few microtesla with reasonable signal-to-noise ratio, the probe sensitivity needs to be such that magnetic fluctuations of  $b \geq 10 \text{ nT}$  in the above mentioned frequency range can be detected. Additionally, some technical constraints have to be considered in the probe design. First of all it must be insensitive to electrostatic pickup, since drift waves are associated with fluctuations of the plasma potential in the same frequency range as the magnetic fluctuations [42]. Furthermore the probe has to withstand thermal load from the plasma and its dimensions have to be small compared to plasma dimensions in order to avoid strong perturbations.

### 2.2.2 Available sensor types

A recent review of available sensor types can be found in [45, 46]. It is used to make a preselection of the types to be tested. The sensors are in the following compared based on the range of magnetic field amplitudes they can detect. A summary of 11 sensor types is given in Fig. 2.2. Most of them can be excluded due to the discussed limitations in VINETA. The most obvious criterion is the range of detectable magnetic amplitudes needed for our experiments, four sensor technologies are ruled out accordingly. A second issue is the limitation for the probe head dimension. Hence, sensor types with a need for a large dimensional setup are not suitable. This concerns the optically pumped magnetometer, the nuclear-precession magnetometer, the SQUID magnetometer and the fiber-optic magnetometer. The flux gate magnetometer cannot be used either, since its frequency response is limited to very low frequencies. The remaining two types search coil magnetometer, better known as  $\dot{B}$ -detector, and magneto-resistive magnetometer are seen as possible candidates.

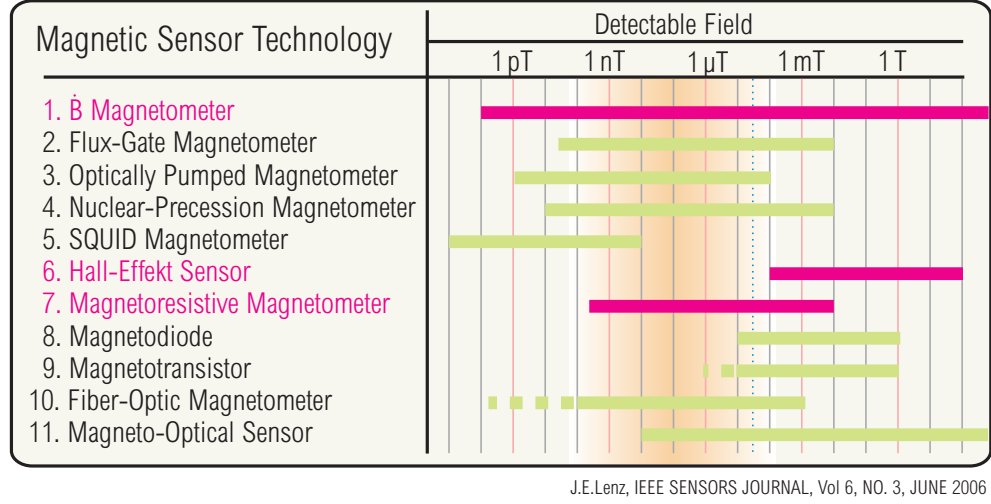


Figure 2.2: Applicability of different sensor types for magnetic fields in terms of detectable amplitudes. The range of interest for waves in VINETA is marked red. Three types were picked out for testing (magenta). To give an intuitive idea about the shown magnitudes, the magnetic field of the Earth is included (blue line). Adapted from [46].

Additionally, the Hall sensor is considered and tested even though its sensitivity is insufficient. However, in previous work it was successfully used as low-frequency magnetic detector in fusion plasmas [47, 48]. The preselection made so far gives only a rough orientation as the available devices are optimized for different purposes by the manufacturer. Tab. 2.1 compiles the three chosen devices.

To compare the sensors, their sensitivity  $S(\omega)$  in units V/T is measured as function of frequency. For this purpose, a test field consisting of two coils with a diameter of 78 mm, four windings each, and 35 mm separated from each other, is used. The scaling of the generated field strength inside this coil arrangement with coil current is numerically and experimentally determined to be  $97.8 \mu\text{T/A}$ . The coil current is typically 20 mA, measured with a shunt of  $50 \Omega$ , resulting in a fluctuating field of  $b = 1.96 \mu\text{T}$ . The sensor calibration is performed by automatically sweeping the frequency as illustrated in Fig. 2.3.

Table 2.1: Chosen sensor devices for detection of magnetic field

manufacturer	device	sensor type	dimension [mm <sup>3</sup> ]
Infineon	KSY14	Hall	6
Honeywell	HMC1001	magneto-resistive	80
home-made	coil N=1000	$\dot{B}$ -detector	38

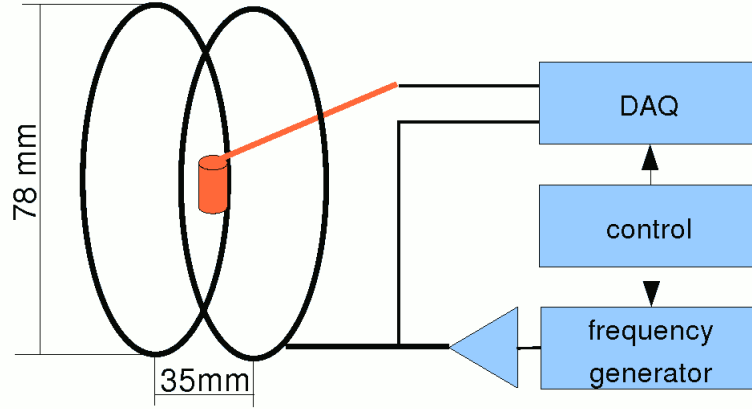


Figure 2.3: Setup for calibrating magnetic field probes. The sinusoidally fluctuating field in-between the two coils is sensed by the probe and recorded with an oscilloscope. A broad frequency range of typically 100 Hz . . . 2 MHz is covered by automatically setting horizontal and vertical deflections as well as the driving frequency.

The obtained sensitivity  $S(\omega)$  alone is not meaningful for comparing different sensors. Using external or internal amplifiers,  $S$  can take any value for the same device and is not connected to the smallest detectable field strength. The smallest detectable amplitude is actually limited by the noise figure of a certain device. It is measured by recording the sensor signal of 100 ms duration with a high sampling rate of  $f_{\text{smp}} = 10$  MHz. The power spectral density of this signal, obtained by Fourier transformation and subsequent averaging, is a frequency-resolved measure for the noise density

$$u_{\text{noise}}(\omega) = \frac{1}{2\pi} \int U_{\text{noise}}(t) e^{-i\omega t} dt . \quad (2.6)$$

If a certain bin width of  $\Delta f$  is assumed, the spectral density can be expressed as

$$U_{\text{noise}}(\omega) = u_{\text{noise}} \cdot \Delta f . \quad (2.7)$$

In this way, it is possible to define the signal-to-noise ratio for a given magnetic field amplitude  $b_0$  as

$$\text{SNR} = 20 \log \left( \frac{S(\omega) b_0}{U_{\text{noise}}(\omega)} \right) . \quad (2.8)$$

In the following a bin width of  $\Delta f = 100$  Hz is assumed. This is equal to an integration time of 10 ms and limits the observable fluctuations to frequencies above 100 Hz in agreement with the specifications given in Sec. 2.2.1. The frequency-resolved result for the three devices is presented in Fig. 2.4 in terms of (a)  $S(\omega)$  and (b)  $\text{SNR}(\omega)$ . It will be discussed for each device in the following paragraphs.

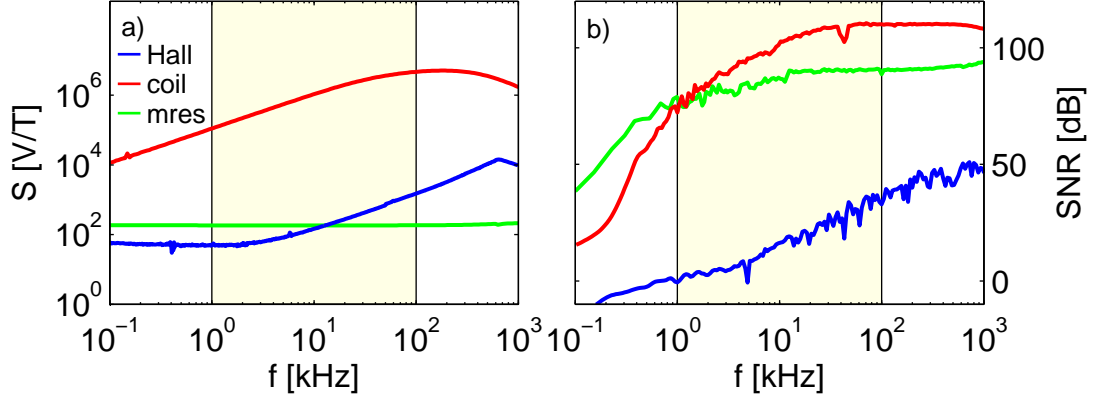


Figure 2.4: Frequency response of the tested Hall sensor, the magneto-resistive sensor and the  $\dot{B}$ -detector with low noise amplifier. The frequency-resolved sensitivity of the devices is given in (a). The signal-to-noise ratio SNR in (b) is a measure for the lowest detectable magnetic field. The SNR is calculated for an assumed fluctuating field amplitude of  $b = 1 \mu\text{T}$  and the noise spectral density generated by the sensors.

### $\dot{B}$ -detector

The simplest approach to detect fluctuating magnetic fields is the induction coil, also known as  $\dot{B}$ -detector. For use in plasmas, they are kind of a standard [21]. The principle is based on Faraday's induction law. The output voltage  $U_{\text{ind}}$  of a coil is given by

$$\oint_C \vec{E} \cdot d\vec{l} = -\frac{d}{dt} \int_A \vec{b} \cdot d\vec{A} \quad (2.9)$$

$$U_{\text{ind}} = -N A \dot{b} \quad (2.10)$$

$U_{\text{ind}}$  depends linearly on the number of windings  $N$ , the coil area  $A$  and the time derivative of the fluctuating magnetic field  $b$ . If the time dependency of  $b$  is harmonic, the induced voltage is

$$U_{\text{ind}}(\omega) = -N A b_0 \omega \cos(\omega t) \quad (2.11)$$

which scales linearly with the frequency. For gaining high sensitivity, the number of windings  $N$  and the area  $A$  can be adapted, although this might be in contradiction with the constraint of small sensor dimension.

For a  $\dot{B}$ -detector with  $N = 1000$ , the sensitivity  $S$  is recorded as shown in Fig. 2.4 (a). It has a linear dependency for low frequencies up to 10 kHz, a maximum around 200 kHz, and decreases for higher frequencies. At 1 kHz, the sensitivity has a value of  $S = 100 \text{ mV}/\mu\text{T}$ . For the low frequency range, the measured dependency is as

expected from (2.10) with  $S = -NA\omega$ . At higher frequencies, the coil shows resonance and the simple description given in (2.10) is not valid any more. The resonance circuit consisting of the parasitic capacity and the coil inductance is damped with an external termination resistor of  $R = 2\text{ k}\Omega$ . The result is a broadening of the resonance peak to the observed sensitivity maximum around 200 kHz.

### Magneto-resistive sensor

A magneto-resistive sensor [49] is based on the change of the resistance of a material in a magnetic field

$$R = R(b) \quad , \quad (2.12)$$

which is usually very small. Therefore, most of the available devices are equipped with an internal amplifier. The output voltage is directly proportional to the magnetic field. An important issue is magnetical saturation of the material, which can lead to a changed sensitivity, e.g. in the ambient magnetic field of plasma devices.

The most promising device based on the magneto-resistive effect in terms of sensitivity was found to be the HMC1001, produced by the company Honeywell. The result of the frequency response measurement in Fig. 2.4 (a) is an almost perfect characteristic with constant sensitivity of  $S = 0.2\text{ mV}/\mu\text{T}$  over the entire frequency range.

### Hall sensor

A current transverse to the magnetic field is deflected due to the Lorentz force and generates in the direction of deflection a potential difference of

$$U_{\text{Hall}} = A_H \frac{Ib}{d} \quad . \quad (2.13)$$

This effect is named Hall effect.  $A_H$  is the Hall constant of the material,  $I$  the transverse current,  $b$  the magnetic field and  $d$  the dimension of the current channel. The generated voltage fluctuations are directly proportional to the fluctuating magnetic field.

For the chosen device KSY14 (Infineon), the measured frequency response is shown in Fig. 2.4 (a). For  $f \leq 1\text{ kHz}$ , the sensitivity is constant with  $S = 0.07\text{ mV}/\mu\text{T}$ . After a transition range from  $f = 1 \dots 10\text{ kHz}$ , the sensitivity rises with frequency linearly up to  $f = 700\text{ kHz}$ . The slope of  $S(f)$  is similar to the  $\dot{B}$ -detector with the same value of 3 dB per octave. This is an indicator for the dominance of induced

voltages, possibly in the internal wiring of the Hall sensor. Hence, the sensor does not give reliable results for frequencies  $f > 10$  kHz.

### Comparison of the three sensor types

The limitation of the sensors is mainly determined by the frequency-dependent noise. For a given integration time  $\Delta t$ , a signal  $b(\omega_0)$  is detectable only if the corresponding sensor output voltage is larger than the noise amplitude at the same frequency  $\omega_0$ . Hence, a good measure for the sensor performance is the signal-to-noise ratio (cf. Eq. 2.8), taking into account sensitivity and noise amplitude as shown in Fig. 2.4 (b). An amplitude of the fluctuating magnetic field of  $1 \mu\text{T}$  is assumed for the calculation of the signal-to-noise ratio from the recorded noise spectrum. This was found to be a realistic wave amplitude in VINETA (cf. Sec. 4.1.1).

For the magneto-resistive sensor, the signal-to-noise ratio ranges from 79 dB at 1 kHz to 94 dB at 1 MHz. The frequency dependence is attributed mainly to the measured noise spectrum, since the sensitivity was determined to be constant. In the case of the  $\dot{B}$ -detector, the signal-to-noise ratio is defined by both the sensitivity and the noise spectrum with 76 dB at 1 kHz and 108 dB at 1 MHz. For the Hall sensor, the frequency dependence of the signal-to-noise ratio is also determined by the sensitivity and noise spectrum with values of 0 dB at 1 kHz and 48 dB at 1 MHz. That means, the frequency response of the  $\dot{B}$ -detector and magnetoresistive detectors is better than that of the Hall sensor. The  $\dot{B}$ -detector is chosen for the measurements of magnetic fluctuations in VINETA because it has the best signal-to-noise ratio.

### 2.2.3 Design of the $\dot{B}$ -detector

The wave magnetic field under investigation  $\vec{b} = (b_x, b_y, b_z)'$  requires the usage of a 3-axis  $\dot{B}$ -detector. Its design can be inferred from Fig. 2.5. Teflon, which is heat proof and can be used in vacuum, has been chosen as base material. Two small coils with a diameter of 3 mm and a length of 8 mm are perpendicularly arranged in a teflon body. They record the fluctuating magnetic fields  $b_x$  and  $b_y$ . The third component  $b_z$  is detected by two coils which are located close to the  $b_x$  and  $b_y$  coil on both sides. This avoids asymmetry in the determination of  $b_z$ . Each of the four coils is wound with approximately 1000 windings with enamelled copper wire of  $50 \mu\text{m}$  diameter. The leads are twisted and connected to a differential amplifier located in the probe shaft, 20 cm apart from the probe head inside the vacuum vessel. The whole  $\dot{B}$ -probe, from the probe head to the amplifiers, is fully shielded against electric pickup. While the head is surrounded by a brass cylinder, the 4 twisted

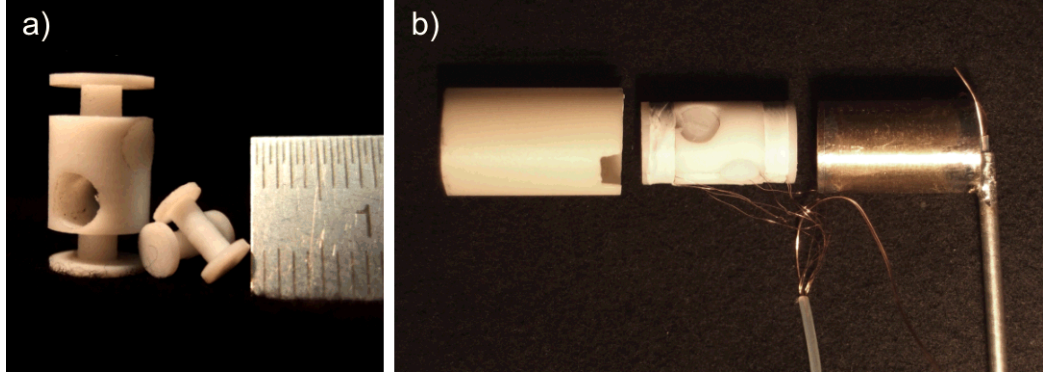


Figure 2.5: Design of a three-axis  $\dot{B}$ -detector. The probe body, made of tefflon, is shown in a). It has two perpendicular oriented bore-holes with a diameter of  $d = 3$  mm, housing the two small coils for the magnetic directions  $b_x$  and  $b_y$ . The third coil for  $b_z$  is split up into two parts, which are integrated into the tefflon body. A ready wound probe head (b, middle), connected to the amplifiers via 4 twisted pair lines, is electrically shielded with a brass cylinder (b, right). The probe is isolated from the plasma by a ceramic tube (b, left). A temperature sensor (PT100) for heat monitoring is located in the brass cylinder (not visible).

coil leads run in a stainless steel tube which is connected to an aluminium box housing the four amplifiers. To prevent perturbation of the plasma by introducing an electric conductor, all parts facing the plasma are covered with ceramic. The cylindrical probe head including the ceramic has a diameter of  $d = 10$  mm and a length of  $l = 18$  mm. In addition to the already mentioned parts it also contains a temperature sensor to monitor the heat load and prevent the coils from thermal damage. The leads of the four coils are connected to low-noise differential amplifiers of type THAT1512 via an input circuit, as shown in Fig. 2.6. Due to its parasitic capacity, the coil is actually a parallel resonance circuit. Its resonance frequency is smaller than 1 MHz and must be damped to avoid a sharp resonance peak in the sensitivity. One task of the input circuit is the damping of this resonance with the two 1 k $\Omega$  resistors. Another task is the rejection of signal components at the plasma generation frequency 13.56 MHz. This is achieved with an LC low-pass filter with a cut-off frequency of 1 MHz, followed by two LC-absorption circuits at 13.56 MHz and 27.12 MHz for the first and second harmonic. The filter has a fully symmetric design to be appropriate for the symmetric signal from the coil and the symmetric input of the amplifier.

The measured transfer function of the filter is shown in Fig. 2.7. For frequencies up to 1 MHz, the amplification is close to 1 and only a small phase shift  $\Delta\phi \ll \pi/2$  is introduced. At the absorption frequency  $f = 13.56$  MHz the attenuation is -95 dB and at the second harmonic it is -69 dB.

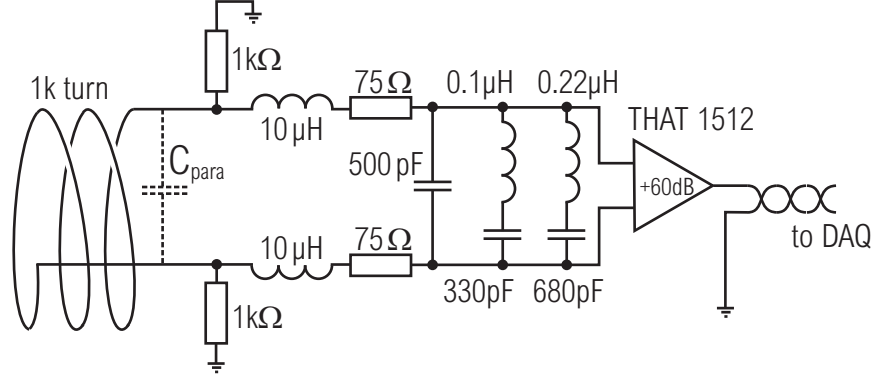


Figure 2.6: Electronic connection of one detection coil to the low-noise amplifier. The self-resonance of the coil is damped by two resistors with  $1\text{ k}\Omega$ . Additionally, a filter is integrated to reject the helicon source rf-frequency of  $13.56\text{ MHz}$  and its second harmonic. The amplification of the signal is set to  $60\text{ dB}$ , allowing the direct connection of the output to a data acquisition system without any additional external amplification.

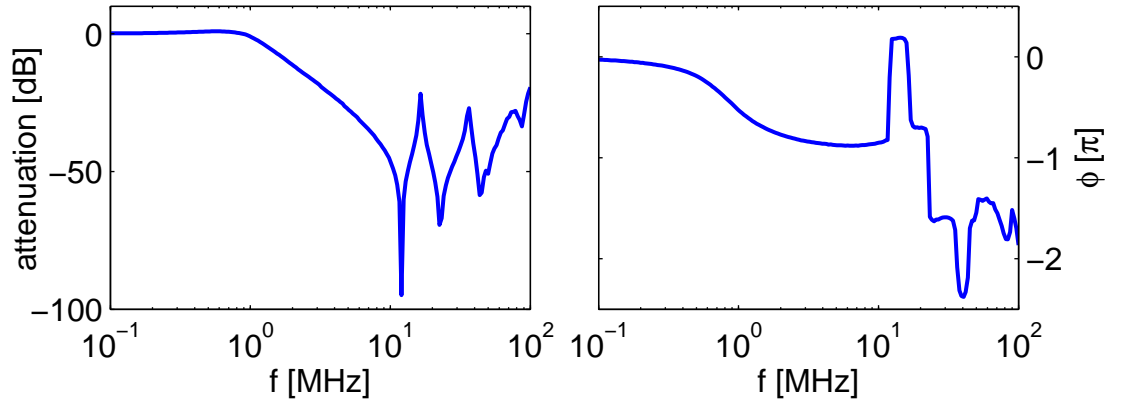


Figure 2.7: Complex transfer function of the filters used in-between the  $\dot{B}$ -probe head and the low-noise amplifiers, one for each channel. A filter consists of an LRC-lowpass with a transit frequency of  $f = 1\text{ MHz}$ , followed by two notch filters at  $13.56\text{ MHz}$  and  $27.12\text{ MHz}$ .

### 2.2.4 Calibration of the $\dot{B}$ -probe

The  $\dot{B}$ -probe delivers four output voltages containing the information of the three-dimensional magnetic field at the probe position. The frequency response of all four coils is to be absolutely calibrated. To correct for any misalignment of the coils inside the probe head, a directional calibration is done in a second step. The sensitivity as frequency dependent function of a single magnetic sensor is given by

$$S_\omega = U_\omega / b_\omega \quad (2.14)$$

Assuming a time varying magnetic field in the direction of the coil surface normal with a single Fourier component,  $b(t) = b_0 \exp(i\omega t)$  yields for the output voltage

$$U(t) = N \, d\Phi / dt = N A \dot{b}(t) \quad (2.15)$$

$$= N A i \omega b(t) \equiv S_\omega b(t) \quad (2.16)$$

with the number of windings  $N$  and the effective area  $A$  as coil parameters. To include deviations from the ideal case, the function  $S_\omega$  is recorded experimentally. A typical calibration curve for the  $\dot{B}$ -probe is shown in Fig. 2.8. The measured sensitivity has a linear characteristic for frequencies in the range below 10 kHz, just as in the ideal case. At higher frequencies, the self-resonance of the coil caused by the inductivity in parallel to the parasitic inter-winding capacity determines the sensitivity maximum at around 200 kHz. For even higher frequencies,  $S_\omega$  is determined by the amplifier characteristic since its bandwidth is limited to 1 MHz. This causes an attenuation in the amplitude and a phase deviation from the ideal  $\phi = \pi/2$ .

The above procedure of calibration via  $S_\omega$  is not convenient if incoherent signals of the fluctuating magnetic field are considered. Instead, an integration over time of the signal  $U(t) \sim \dot{b}(t)$  prior to the frequency calibration can be done. From a measured signal  $U(t)$ , an integrated version  $U^{\text{int}}$  is numerically obtained as

$$U^{\text{int}}(t) = \int_0^t U(t') \, dt' \quad \leftrightarrow \quad \frac{dU^{\text{int}}}{dt} = U(t) \quad (2.17)$$

To calibrate this signal, a sensitivity  $S_\omega^{\text{int}}$  can be defined in the same way as it was done for  $U(t)$  in (2.14). The relation between the two sensitivities is found by Fourier transformation of (2.17)

$$U_\omega = \frac{1}{2\pi} \int_0^T \frac{dU^{\text{int}}}{dt} e^{-i\omega t} \, dt = i\omega U_\omega^{\text{int}} \quad \rightarrow \quad S_\omega^{\text{int}} = \frac{S_\omega}{i\omega} \quad (2.18)$$

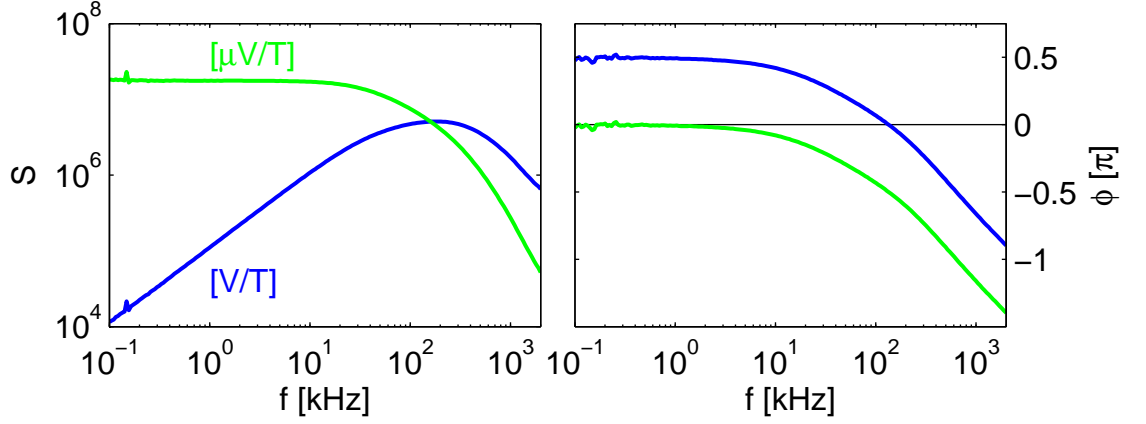


Figure 2.8: Calibration of a used  $\dot{B}$ -detector in terms of sensitivity and phase run in the range from 100 Hz...2 MHz (blue). Integrating the timeseries prior to further processing leads to a different calibration (green) with almost no frequency dependency below 10 kHz.

The linear slope  $\sim \omega$  and the phase shift by  $\pi/2$  of  $S_\omega$  do not occur for  $S_\omega^{\text{int}}$ . In the ideal case, it is a constant. By integration of the signal from a  $\dot{B}$ -probe, a signal directly proportional to the magnetic field fluctuations is obtained. The conversion to units of magnetic field is done by multiplication with a constant. For the  $\dot{B}$ -probe, the frequency characteristic of the complex  $S_\omega^{\text{int}}$  is included in Fig. 2.8. In the low-frequency range  $f \leq 10$  kHz, the amplitude characteristic is almost constant with a phase close to 0. The absolute value of the sensitivity here is  $S_\omega^{\text{int}} = 17$  V/T. This is several orders of magnitude higher than  $S_\omega$ , which compensates the attenuation of the signal by the integration.

The output voltage of an individual coil is influenced by the specific orientation of the coil and the coil geometry. Hence, the direct use of the calibrated signals from the  $\dot{B}$ -probe is not accurate. The two mentioned effects are compensated by a directional calibration tensor. The only requirement for this approach is the orientation of the coil surface normals in such a way that they span a non-degenerated three-dimensional space. The resulting magnetic field can be expressed as

$$b_x = S_1^x U_1 + S_2^x U_2 + \dots S_n^x U_n \quad (2.19)$$

$$b_y = S_1^y U_1 + S_2^y U_2 + \dots S_n^y U_n \quad (2.20)$$

$$b_z = S_1^z U_1 + S_2^z U_2 + \dots S_n^z U_n, \quad (2.21)$$

or in short

$$\vec{b} = A_{\text{cal}} \vec{U}. \quad (2.22)$$

The number  $n$  of coils is four in the case of our  $\dot{B}$ -probe. Each component of  $A_{\text{cal}}$  converts a voltage to a magnetic field and is thus a sensitivity. The tensor can be

split into two parts

$$A_{\text{cal}} = A_{\text{dcal}} A_{\text{fcal}} \quad , \quad (2.23)$$

where  $A_{\text{dcal}}$  is a  $3 \times 3$  matrix for directional calibration and  $A_{\text{fcal}}$  a  $3 \times n$  matrix for frequency calibration. The latter one has  $n$  nonzero elements which are derived from the frequency calibration described above, one for each coil. Experimentally, the matrix  $A_{\text{dcal}}$  is obtained by comparing the measured magnetic field  $\vec{b}_{\text{meas}} = A_{\text{fcal}} \vec{U}$  with the theoretically derived field  $\vec{b}$  of a well defined cylindrical test field. Since this vector equation has three components and  $A_{\text{dcal}}$  has 9 elements, three spatial points of the test field have to be determined. They have to be chosen in such a way that the involved magnetic field vectors span a non-degenerated three-dimensional space to form 3 linearly independent equations. This can be written as

$$\begin{pmatrix} b_x^1 & b_x^2 & b_x^2 \\ b_y^1 & b_y^2 & b_y^2 \\ b_z^1 & b_z^2 & b_z^2 \end{pmatrix} = \begin{pmatrix} A_{11} & A_{12} & A_{13} \\ A_{21} & A_{22} & A_{23} \\ A_{31} & A_{32} & A_{33} \end{pmatrix} \begin{pmatrix} b_{mx}^1 & b_{mx}^2 & b_{mx}^2 \\ b_{my}^1 & b_{my}^2 & b_{my}^2 \\ b_{mz}^1 & b_{mz}^2 & b_{mz}^2 \end{pmatrix} \quad . \quad (2.24)$$

The unknown directional calibration matrix is obtained by multiplying the inverse of the matrix of the measured magnetic field  $b_m$  from the right

$$A_{\text{dcal}} = \hat{b} \cdot \hat{b}_m^{-1} \quad . \quad (2.25)$$

For this calibration, an azimuthal plane in front of the cylindrical coil is scanned with the magnetic sensor with a spatial resolution of 1 cm. To ensure the linear independence of the equations, three magnetic field vectors are chosen out of the scanned plane, spanning a parallelepiped ( $\vec{b}_1, \vec{b}_2, \vec{b}_3$ ) with a volume above a certain threshold.  $A_{\text{dcal}}$  is calculated several times in this way to extract the error of this procedure for every component.

An example of a calibration scan is given in Fig. 2.9. The diagrams in the middle column show the calculated field. It has a maximum in the  $z$ -component along the axis of the coil and flips from positive to negative values for the perpendicular components  $b_x$  and  $b_y$ . The three components of the measured field in the first column are shifted and tilted in comparison with the theoretical field and the perpendicular components are exchanged. All these artifacts are automatically removed by the robust directional calibration procedure including the correct order of the channels: As shown in the right column the calibrated field well reproduces the theoretical one. Since the calibration matrix  $A_{\text{dcal}}$  is calculated from only three magnetic vectors out of the plane, this procedure is not a fit from the measured to the theoretical derived magnetic field.

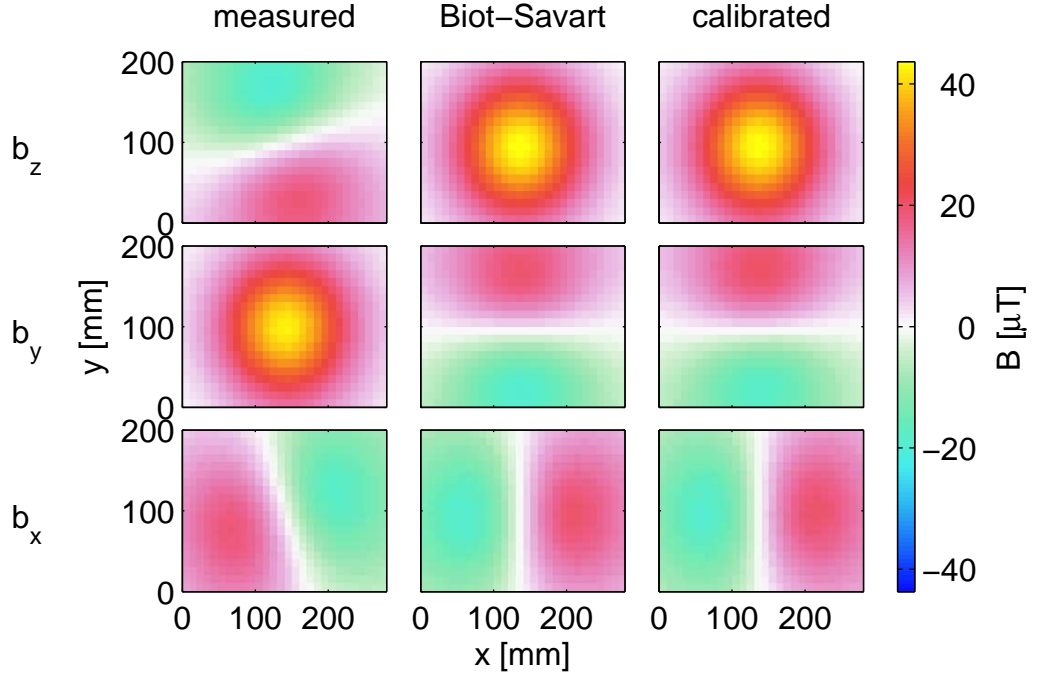


Figure 2.9: Directional calibration of three-axis  $\dot{B}$  detector based on a comparison of the measured and the calculated field of a cylindrical coil. In the left column, the three measured magnetic components  $b_x, b_y, b_z$  are shown in an azimuthal plane in front of the test field coil. The components of the magnetic field, calculated by the Biot-Savart law, in the same plane are shown in the middle column. The components of the magnetic field after the application of the calibration are shown in the right column.

### 2.2.5 Test of the $\dot{B}$ -detector

In addition to the sensitivity, the capacitive pickup rejection is crucial for measuring small magnetic fields in the plasma. The probe is therefore fully shielded as described above. To measure the remaining effect of the pickup, the probe is placed in a plate capacitor with an inter-plate distance of 15 mm. Using an amplifier, electric fields with 5 V/cm are generated inside the capacitor in a frequency range up to 2 MHz. The output voltage of the  $\dot{B}$ -probe is shown in Fig. 2.10. It has a linear slope up to  $f = 100$  Hz, saturates, and then decreases. The output voltage for a magnetic fluctuation of  $1 \mu\text{T}$  of the respective frequency range is included to allow for comparison. It represents a typical wave amplitude and is 20...40 dB larger than the pickup. Although this is already a reasonable value for the signal-to-noise ratio, the origin of measured pickup amplitude is most likely the magnetic field of the electric wires connecting the capacitor. An estimation is included in Fig. 2.10. It

considers the frequency response of the  $\dot{B}$ -detector and the current into the capacitor  $I = \omega U/C$ . The measured signal agrees quite well with this estimate. Hence, the real capacitive pickup is significantly smaller than the measured values and can therefore be neglected.

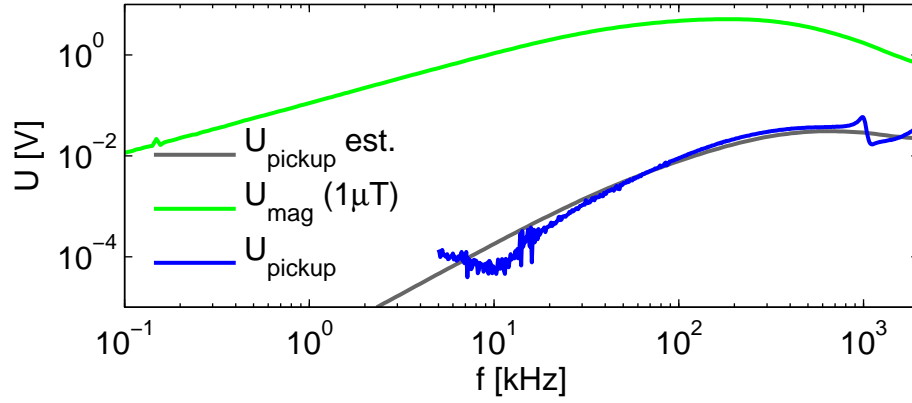


Figure 2.10: Frequency resolved electrostatic pickup measurement (blue) of a  $\dot{B}$ -probe in an electric field of 5 V/cm. For comparison, the expected output voltage for a magnetic field of 1  $\mu$ T at the respective frequency is shown (green). Also included is the estimated voltage output from the magnetic field generated by the currents into the test field capacitor (gray).

A first test of the calibrated  $\dot{B}$ -detector is shown in Fig. 2.11. In VINETA, an operation regime with coherent drift waves is found by variation of the ambient magnetic field  $B_0$  and the neutral gas pressure  $p$ . Magnetic fluctuations are recorded with  $\dot{B}$ -detectors simultaneously at two separate spatial positions in the density gradient. In the amplitude spectrum in Fig. 2.11 (a) the peak of the coherent drift wave at a frequency  $f_0 = 2.2$  kHz is clearly separated from other signal components. The cross phase in Fig. 2.11 (b) at that frequency is well defined. A second harmonic at  $f_1 = 4.4$  kHz is observed with a smaller power spectral density. For comparison a second time series with the same plasma conditions is recorded with one of the  $\dot{B}$ -detectors rotated by 180°. The resulting power spectral density is slightly changed only. The crossphase in the two measurements differs significantly, i.e. a clear phase shift about  $\pi$  is observed for  $f_0$  and  $f_1$ . The observed phase shift after rotating the probe demonstrates that electrostatic pickup can be neglected.

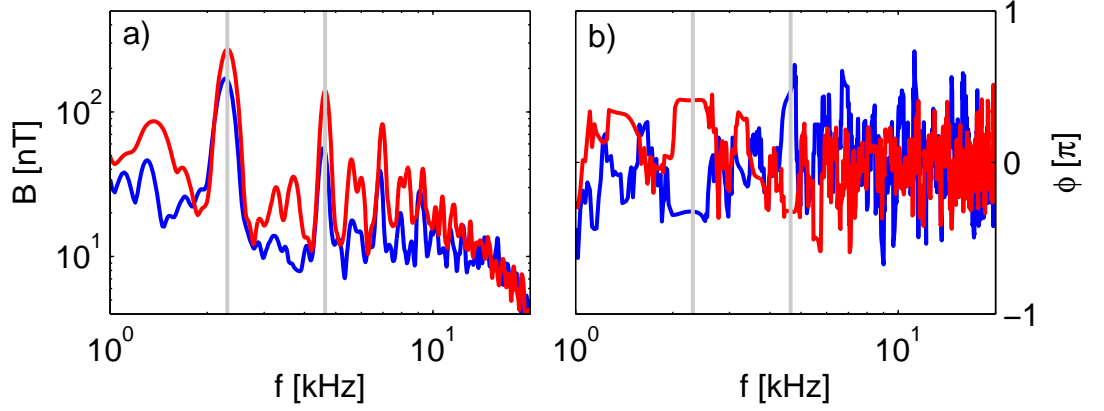


Figure 2.11: Test of  $\dot{B}$ -probe in the plasma. The detector is placed in the density gradient, where a coherent drift wave at 2.3 kHz is observed with its higher harmonics. A second measurement is recorded with the probe rotated by  $180^\circ$  (red line). (a) shows the power spectral density for the two cases, (b) shows the phase of the magnetic signal relative to the signal from a reference probe.

### 2.3 Langmuir probes

The low temperature plasma in VINETA is well accessible with Langmuir probes. This diagnostic was proposed by Mott-Smith and Langmuir in 1926 [50] and is now a standard method to measure different plasma parameters [51], i.e. the plasma density  $n$ , the electron temperature  $T_e$ , and the plasma potential  $\Phi_p$ . The principle of Langmuir probes is based on a small electrode, introduced into the plasma. From the measurement of the current-voltage characteristic the above plasma parameters are obtained as follows. Quasineutrality  $n_i \approx n_e$  is assumed with a thermalized ion and electron population. The energy distribution function of the electrons is a Maxwellian

$$f(v) = n \left( \frac{m_e}{2\pi T_e} \right)^{3/2} \exp \left( -\frac{m_e v^2}{2k_B T_e} \right) , \quad (2.26)$$

Ions have a similar energy distribution function, but often with much smaller temperatures  $T_i \ll T_e$  [25]. In VINETA ion temperatures are in the range of 0.1 eV [52] and electron temperatures are in the range 3-5 eV [53].

#### Ion saturation range

If the probe is biased negatively with respect to the plasma potential  $\Phi$ , it repels electrons and attracts ions. A sheath with an extend of the order of several Debye

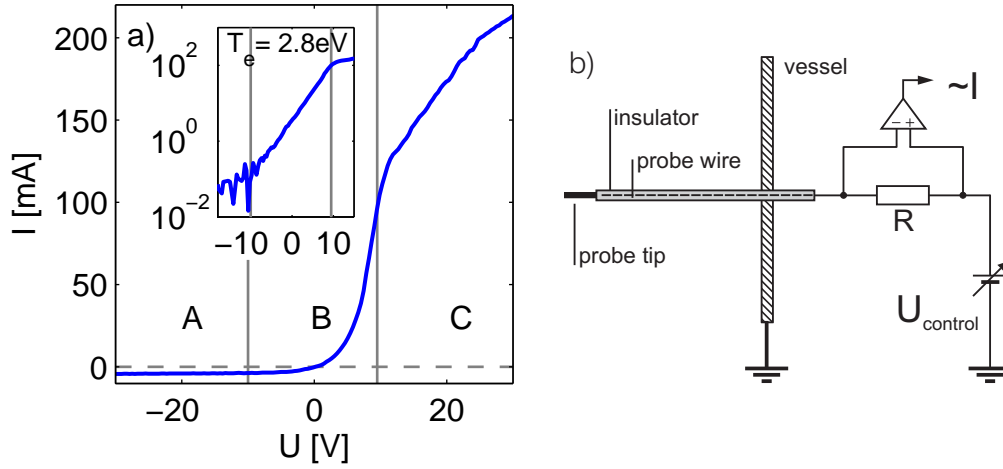


Figure 2.12: Measurement and evaluation of a Langmuir probe characteristic. The probe is biased in the range  $U_p = -100 \dots 100 \text{ V}$ . (b) the current flow in the plasma is picked up with a shunt resistor and recorded with a high impedance isolation amplifier. The obtained current-voltage characteristic (a) can be divided into 3 parts: the ion saturation range (A), the electron current range (B) and the electron saturation range (C). For thermal electrons the characteristic in the transition range is exponential. The inset of (b) shows a semilogarithmic plot after subtraction of the ion saturation current.

length  $\lambda_D$  is formed. Inside the sheath, the probe potential is not shielded out and almost all electrons are expelled. The ions are attracted by the negative potential of the probe tip. The probe current, carried by the ions only, is given by the Bohm-criterion for a stable sheath [54]

$$j_i = 0.61 n_e e \sqrt{\frac{k_B T_e}{m_i}} . \quad (2.27)$$

The ion saturation current density  $j_i$  is proportional to the electron density and the square root of the electron temperature.

### Electron current range

If the probe is negatively biased with respect to the plasma potential but in the range of the potential equivalent of the electron temperature, electrons partly reach the probe tip surface depending on their kinetic energy. The electron density is then given by the Boltzmann equation

$$n_e = n_{e0} \exp \left( \frac{U - \Phi_p}{k_B T_e} \right) . \quad (2.28)$$

Here  $n_{e0}$  is the electron density at the sheath edge. For a Maxwellian velocity distribution function  $f(v)$ , the electron current to a probe with surface  $S$  is

$$I(U) = -S n_e(U) e v = -S n_e(U) e \int_0^\infty v f(v) dv = -S n_{e0} e \sqrt{\frac{T_e}{2\pi m_e}} \exp \left( \frac{U - \Phi_p}{k_B T_e} \right) , \quad (2.29)$$

The resulting exponential probe current characteristic  $I(U)$  is shown in Fig. 2.12 (a, inset) for a typical plasma in VINETA. From  $I(U)$  the electron temperature  $T_e$  can be determined. According to [55] (2.29) can be rewritten for arbitrary energy distribution functions as

$$I(U) = -\frac{2\pi e}{m_e^2} \int_{eU}^\infty (W - eV) f(W) dW , \quad (2.30)$$

where  $W$  denotes the kinetic energy of the electrons  $W = m_e v^2/2$ . An anisotropy is introduced in a magnetized plasma via a magnetic field  $B_0$ . Here the sheath has different spatial extents parallel and perpendicular to  $B_0$ . This is taken into account in a kinetic probe theory by introducing different energy dissipation lengths for electrons parallel and perpendicular to  $B_0$  [56]. The probe current is expressed as

$$I(U) = C \int_{eU}^\infty R_{Le} W f(W) dW , \quad (2.31)$$

where  $R_{Le}$  is the energy-dependent lamor radius of the electrons and  $C$  is a geometrical factor depending on whether the probe is oriented parallel or perpendicular to the magnetic field. This kinetic theory has been used to determine the electron temperature for the magnetized plasma in VINETA with an assumed Maxwellian energy distribution function.

### Electron saturation range

If the probe is positively biased with respect to the plasma potential  $\Phi_p$ , the probe current is given by all electrons in the energy distribution function. In particular for  $U = \Phi_p$  (2.29) yields the electron saturation current

$$I_{e,\text{sat}} = -S n_{e0} e \sqrt{\frac{T_e}{2\pi m_e}} . \quad (2.32)$$

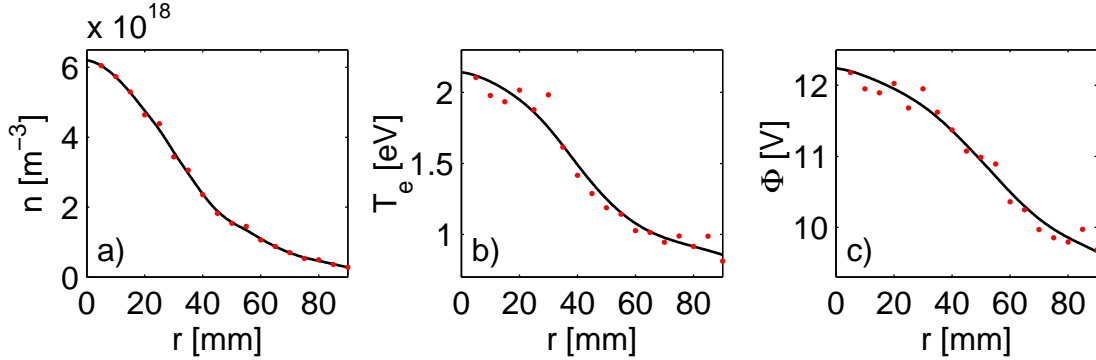


Figure 2.13: Radial profiles of (a) plasma density  $n$ , (b) electron temperature  $T_e$  and (c) plasma potential  $\Phi$  for a helicon plasma with an ambient magnetic field of 48 mT.

This of course an idealized description and is not observed in experiment. For  $U > \Phi_p$ , the current rises almost linearly with increasing voltage, as seen in Fig. 2.12 (range C). This is due to the growing sheath with increased voltage, which is not considered in (2.32).

### Probe measurements of plasma profiles in VINETA

A Langmuir probe is placed on a positioning system to move the probe along the radial coordinate of the plasma cylinder. At a chosen number of positions, current-voltage characteristics are recorded and the plasma density, the electron temperature, and the plasma potential are determined as described above. The density profile  $n(r)$  in Fig. 2.13 (a) has a maximum  $n_0 = 8.6 \cdot 10^{18} \text{ m}^{-3}$  in the center and decreases at a distance of  $r = 70 \text{ mm}$  to  $4.2 \cdot 10^{17} \text{ m}^{-3}$ . The temperature profile  $T_e(r)$  in Fig. 2.13 (b) is also peaked with a value of 3 eV in the center and 2 eV at  $r = 70 \text{ mm}$ . The plasma potential in Fig. 2.13 (c) has only a weak radial dependence with values between +10 V and +12 V. Such profiles are typical for helicon discharges [40].

## 2.4 Interferometer

The heterodyne microwave interferometer used on VINETA measures the change in optical path length for a microwaves beam directed perpendicular to the ambient magnetic field. The probing wave propagates in the plasma as O-mode [57] with the wave electric field directed parallel to  $B_0$ . Thus, the probing wave has the same

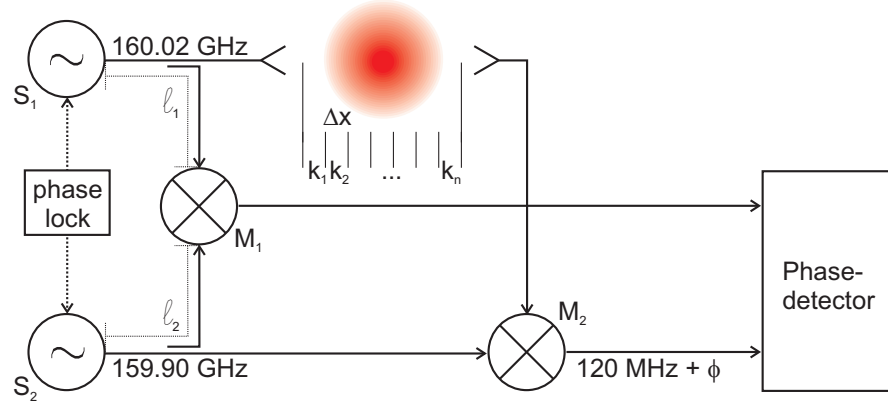


Figure 2.14: Principle of the microwave interferometer. The probing 160.02 GHz beam is mixed with the 159.90 GHz reference twice, before and after passing the plasma. The phase difference caused by the change in optical path length occurs in the 120 MHz intermediate frequency.

dispersion relation as a wave in an unmagnetized plasma [58]

$$k(\omega) = \frac{1}{c} \sqrt{\omega^2 - \omega_p^2} \quad \text{with} \quad \omega_p = \sqrt{\frac{e^2 n}{m_e \epsilon_0}} \quad (2.33)$$

the plasma frequency. An O-mode with frequency  $\omega$  propagates below the critical density  $n_c$

$$n_c = \frac{\omega^2 m_e \epsilon_0}{e} . \quad (2.34)$$

The peak density VINETA is  $n = 2 \cdot 10^{19} \text{ m}^{-3}$ , which is equivalent to a plasma frequency  $f_p = 39.8 \text{ GHz}$ . The interferometer was chosen to operate at a significantly higher frequency  $f = 160 \text{ GHz}$  to avoid diffraction of the probing wave. The basic setup of the interferometer is shown in Fig. 2.14. Two phase-locked harmonic signals are generated with a small frequency difference. The first one with  $f = 159.90 \text{ GHz}$  is used as reference with a phase at the input mixer  $M_1$  of

$$\phi = k \Delta l_1 - \omega_1 t = \frac{\omega_1 \Delta l_1}{c} - \omega_1 t . \quad (2.35)$$

It is mixed with the second signal at  $f = 160.02 \text{ GHz}$ , which results in a harmonic signal at  $f = 120 \text{ MHz}$  with the phase

$$\Delta \phi_1(t) = \frac{\omega_1 l_1 - \omega_2 l_2}{c} - (\omega_1 - \omega_2) t . \quad (2.36)$$

The quantities  $l_1$  and  $l_2$  are the path lengths from the signal generators to the mixer  $M_1$ . The second signal at  $f = 160.02 \text{ GHz}$  is passed through the plasma as dispersive

medium. The phase at the input of mixer  $M_2$  is the sum of phase shifts along the distances  $\Delta x$ , as illustrated in Fig. 2.14. This can be written in integral form as

$$\phi_2 = \int_{x_0}^{x_1} k(x) dx - \omega_2 t = \int_{x_0}^{x_1} \frac{1}{c} \sqrt{\omega_2^2 - \omega_p^2(x)} dx - \omega_2 t . \quad (2.37)$$

Replacing the frequencies with the associated densities and expanding the square root for small  $n/n_c$  yields

$$\phi_2 = \frac{\omega_2}{2cn_c} \int_{x_0}^{x_1} n(x) dx - \omega_2 t . \quad (2.38)$$

Thus, the phase difference in the measurement leg of the interferometer is

$$\Delta\phi_2(t) = \frac{\omega_1 l_3 - \omega_2 l_4}{c} - \frac{\omega_2}{2cn_c} \int_{x_0}^{x_1} n(x) dx + (\omega_1 - \omega_2)t , \quad (2.39)$$

with the path length  $l_3$  from signal generator  $S_1$  to the plasma and then further to mixer  $M_2$ , and  $l_4$  from  $S_2$  to  $M_2$ . The two time-dependent phase differences  $\Delta\phi_1$  and  $\Delta\phi_2$  which are in fact harmonic signals at 120 MHz are finally passed to the phase detector. It measures the time lag between zeros of the two signals, which is proportional to the overall phase shift

$$\Delta\phi = \phi_0 - \frac{\omega_2}{2cn_c} \int_{x_0}^{x_1} n(x) dx . \quad (2.40)$$

Despite an offset  $\phi_0$  due to different signal path lengths,  $\Delta\phi$  is a measure for the line-integrated plasma density. A typical time series of the interferometer signal is shown in Fig. 2.15 (a). It shows the interferometer signal during the plasma pulse spanning  $t = 100 \dots 500$  ms. For the times when plasma is turned on and off the interferometer signal is a step function with the line-integrated density as step height of  $\int n dl = 3.0 \cdot 10^{17} \text{ m}^{-2}$ . In Fig. 2.15 (b) this value is used to calibrate a radial density profile measured with a probe measurement.

## 2.5 Alfvén wave excitation and detection

The investigation of Alfvén waves in the VINETA- plasma requires the generation and detection of perpendicular magnetic field perturbations. The excitation system

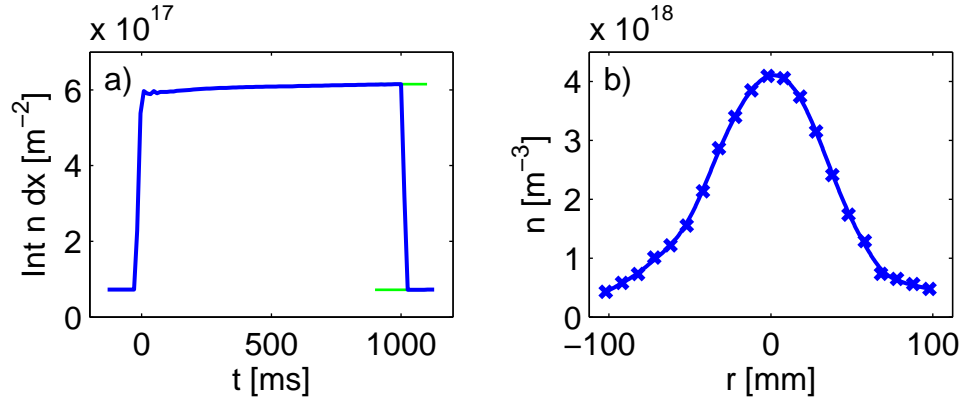


Figure 2.15: Plasma density measured with the interferometer and with a Langmuir probe. The plasma is turned on and off at 0 ms and 1000 ms, respectively, causing an 1 s-impuls in the interferometer signal (a). The impuls height (green bars) is the line-integrated plasma density, which is used to calibrate the plasma density profile measured with a Langmuir probe (b) to absolute density values.

must be able to generate waves with amplitudes large enough to be detected after propagation and damping with a reasonable signal-to-noise ratio. The detector used for this purpose was discussed in Sec. 2.2. Subsequently the wave excitation system is described.

### 2.5.1 Excitation antenna

The wave is excited by a magnetic field which is generated by an antenna located in the plasma. To avoid large disturbances, it consists of two coils placed around the plasma center, where the wave is to be launched. A three-dimensional sketch of the two coils is shown in Fig. 2.16 (a). The antenna is made of  $d = 1.5$  mm copper wire. The windings are insulated against each other and against the plasma with ceramics. The distance between both loops is chosen to be 35 mm to surround the plasma column with a diameter about 30 mm (cf. Sec. 2.3). Both loops have a diameter of  $d = 34$  mm and are wound with the same orientation to act in the same direction. The magnetic field of the excitation antenna in the plane indicated in the sketch is numerically calculated using Biot-Savart's law for a nominal current of 1 A. The resulting magnetic field is shown in Fig. 2.16 (b) and (c). The main component in the plasma center is in the  $y$ -direction with an absolute value of  $104.7 \, \mu\text{T/A}$ . This value changes only slightly inside the antenna volume but strongly decreases outside within a few centimeters. As shown below, wave lengths parallel to the ambient magnetic field are in the range of meters, so the excitation antenna can

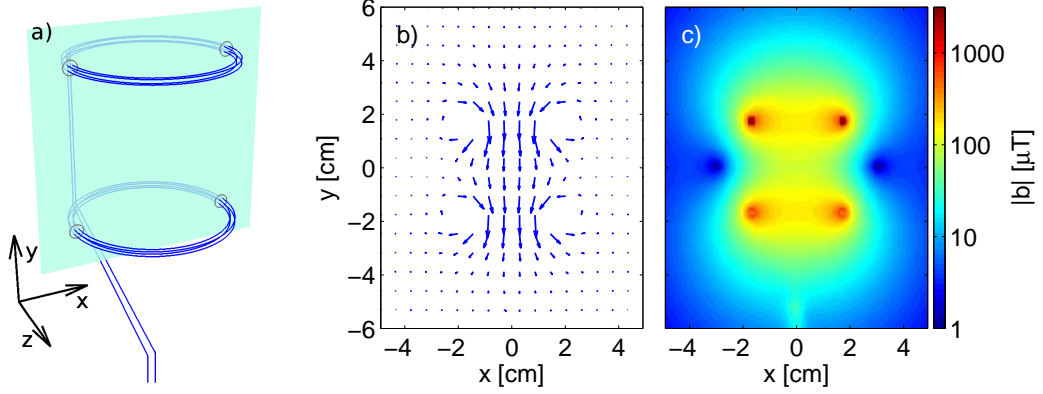


Figure 2.16: (a) sketch of exciter antenna, consisting of two conductor loops and supply lines. In the depicted plane, the magnetic field is calculated for  $I = 1$  A, shown in vector field representation (b) and as absolute value (c).

be considered as a point source for those waves. The frequency range of wave generation depends on the ion-cyclotron frequency and is chosen to be in the range  $f = 0.1 \dots 1.3 \omega_{ci}$  to cover low-frequency effects  $\omega \ll \omega_{ci}$  as well as wave properties around the resonance at  $\omega \sim \omega_{ci}$ . For the three ion species considered, argon, helium and hydrogen, the overall frequency range is 4 kHz  $\dots$  2 MHz, assuming an ambient magnetic field up to  $B_0 = 102$  mT. The broad frequency range, spanning almost three decades, makes it necessary to use two different amplifiers and three different matching networks to operate the excitation antenna.

### 2.5.2 Low-frequency drive

In the low-frequency range up to 50 kHz, a stereo audio amplifier (Omnitronic P3000) with an output power of  $P = 3$  kW at a frequency of  $f = 1$  kHz in bridged mode is used as drive. Its  $4 \Omega$  output impedance must be matched to the low impedance of the exciter antenna with  $R_{DC} = 4.48$  m $\Omega$  to ensure efficient power coupling. It is assumed that the dynamic resistance  $R_{AC}$  is equal to the direct current resistance  $R_{DC}$ . The difference is the irradiated power, which was found to be negligible. The impedance matching is done with the network shown in Fig. 2.17 (a). Its main element is an iron-core transformer with 158 windings on the primary and 12 windings on the secondary side. The usage of a ferrite core transformer was considered but not successful since all tested materials were driven into magnetical saturation at the needed power levels. Besides matching the different impedances, the purpose of the network is to make a galvanic separation between the amplifier and the exciter.

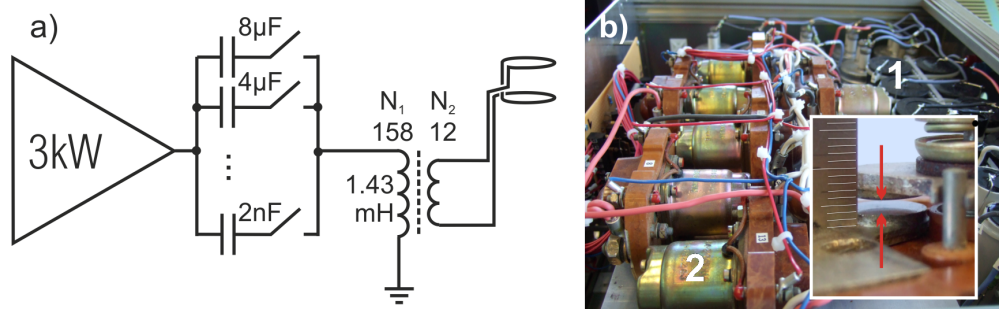


Figure 2.17: (a) Setup of excitation antenna and impedance matching network in the frequency range up to 50 kHz. (b) The photograph shows the switchable capacitor bank with the row of different oil paper capacitors (1) and the relays used as switches (2) with an inter-contact distance of 2 mm (inset) to prevent electrical breakdown in open state.

This turned out to be important since the exciter antenna is not perfectly insulated against the plasma by the ceramic. If operated at a certain potential, the plasma was found to be strongly perturbed. Thus, an electrically floating exciter with its potential determined by the plasma itself is an important requirement in the design of the matching unit.

The transformer converts the peak output current of the amplifier  $I_{\max} = \sqrt{3\text{kW}/4\Omega} = 27.4\text{ A}_{\text{eff}}$  by the transformation factor  $N_1/N_2 = 13.2$ , a maximum current amplitude of 414 A is measured in the antenna. This is somewhat smaller than the theoretically expected value of 511 A due to ohmic losses. The high current in the antenna can be achieved only by compensating the inductive reactants of the transformer with the connected excitation antenna. Otherwise the operation is limited by the highest amplifier output voltage of 150 V. The inductivity of the antenna is  $L = 1.43\text{ mH}$ , resulting in a voltage at the primary transformer winding of  $U = I_{\max}\omega L = 3.5\text{ kV}$  for  $f = 10\text{ kHz}$ . By introducing a serial capacity as shown in Fig. 2.17(a), a resonance circuit is formed for matching. The value of this capacitance depends on the frequency as  $C = 1/(4\pi^2 f^2 L)$ , resulting in required capacitances in the range  $2\text{ nF} \dots 8\text{ }\mu\text{F}$ . This is achieved with 13 switchable capacitors in a dual cascade spanning  $\log_{10}(2^{13}) = 3.9$  decades. A photo of this capacitor box is shown in Fig. 2.17(b).

To allow automatic frequency tuning, computer controlled operation of the capacitor bank is implemented by using high-power high-voltage relays as switches. The resulting maximum current in the secondary winding of the transformer, which is proportional to the generated magnetic field strength, is in fact frequency dependent, as shown in Fig. 2.19. Up to 20 kHz, a magnitude of  $\geq 10\text{ mT}$  can be generated, decreasing by approximately 2 orders of magnitude from 20 to 50 kHz. Reasons are

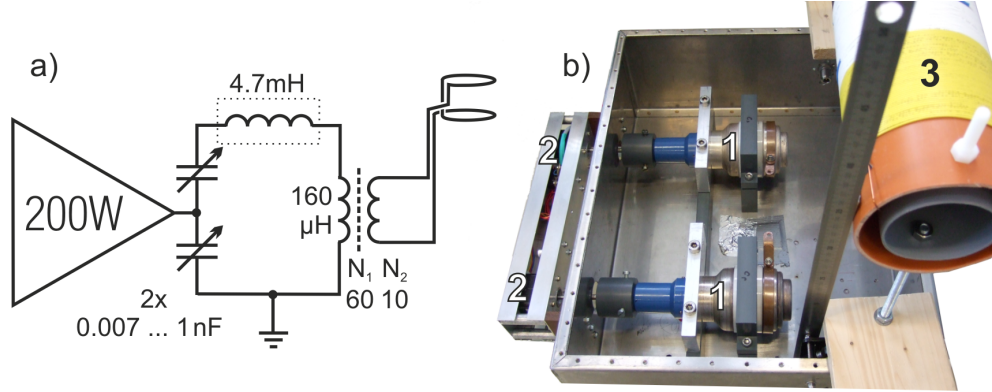


Figure 2.18: Matching circuit used for the high frequency range 500 kHz...2 MHz (a). The photography of the unit (b) shows the selenoid (3) and the tunable vacuum caps (1) which are operated by stepper motors (2).

the frequency limitation of the audio amplifier and the rising losses in the iron-core transformer, which is actually optimized for 50 Hz.

### 2.5.3 High frequency drive

An rf-amplifier (ENI, 200 W, 50  $\Omega$ ) is used to drive the exciter antenna at higher frequencies up to 2 MHz. The main element of the matching network is here a ring-core transformer with acceptable losses for the present frequencies. The transformer again galvanically separates the antenna from the amplifier and transforms the impedance by a moderate ratio of  $N_1/N_2 = 60/10$ . The needed transfer ratio of  $50 \Omega / 4.48 \text{ m}\Omega \approx 10000$  can not be accomplished by the transformer alone. Instead, the transfer ratio is achieved with a resonance circuit consisting of two variable vacuum capacitors with  $C=1 \text{ nF}$  each and the primary winding of the transformer as inductivity. A sketch of the circuit is given in Fig.2.18. The frequency range of matching is  $f = 500 \text{ kHz} \dots 2 \text{ MHz}$ . By using an additional inductance with  $L = 4.7 \text{ mH}$ , a lowering of the frequency range to  $f = 70 \text{ kHz} \dots 350 \text{ kHz}$  is achieved.

The performance of the matching circuits for middle and high frequencies in terms of the highest magnetic field in the exciter antenna is less good when compared to the low-frequency circuit (cf. Fig.2.19). For the high-frequency range one obtains a magnitude of about 1 mT. For the intermediate frequency range, the value is even smaller. The main reasons are high losses the transformer and in the additional inductivity.

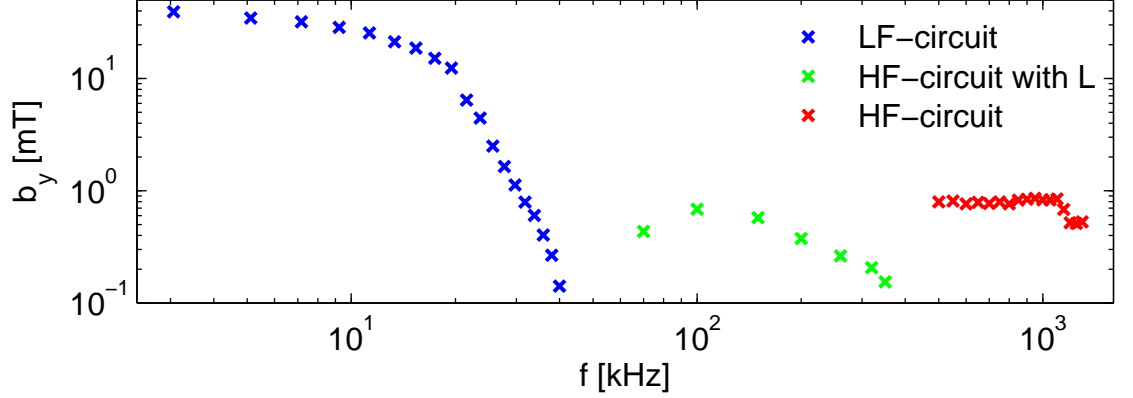


Figure 2.19: Maximum perturbation amplitude of AW excitation setup. To cover the whole frequency range  $f = 4 \text{ kHz} \dots 2 \text{ MHz}$ , three setups are used.

## 2.6 Wave field reconstruction and signal processing

Two wave phenomena are studied in the present thesis. Firstly drift waves (cf. Sec. 3.2) are observed as density fluctuations  $\tilde{n}$ . They propagate in cylindrical geometry in azimuthal direction. Secondly Alfvén waves propagate parallel to  $B_0$  as perpendicular magnetic field perturbations (cf. Sec. 3.1).

### Simultaneous sampling with probe array

One possibility to sample a wave field is the recording of the fluctuating quantity simultaneously at different spatial positions. In the case of drift waves, this is done with an azimuthal probe array [41]. It allows one to record the wave dynamics in space and time at a predefined radial position  $r$ . In the present work the probe array covers 64 positions in the azimuthal direction. A typical coherent mode recorded with this array is shown in Fig. 2.20 (a).

For  $t = 0 \text{ ms}$ , seven density maxima are observed in azimuthal direction. This yields a mode number  $m = 7$ , where the connection to the azimuthal wave vector is given by  $m = k_\phi r$ . The mode propagation results in a stripe pattern typical for a propagating wave. The phase velocity is defined as  $v_{ph} = \omega/k = r\omega/m$ . A convenient way to extract the frequency as well as the mode number is a two-dimensional Fourier transform of the wave data  $n(t, \phi)$ , defined as

$$\hat{n}(\omega, m) = \frac{1}{2\pi T} \int_0^{2\pi} \int_0^T n(t, \phi) e^{i(m\phi - \omega t)} d\phi dt, \quad (2.41)$$

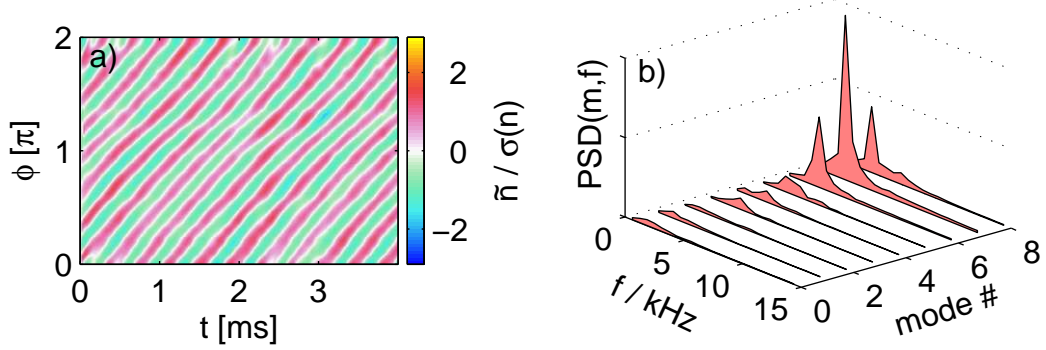


Figure 2.20: Azimuthally propagating drift mode with  $m = 7$ . The associated density fluctuations presented in (a) are recorded with the azimuthal 64 probe array at a radial position of  $r = 30$  mm. The discharge parameters are  $p = 0.23$  Pa and  $B_0 = 48$  mT. Fourier transformation of the recorded density  $n(t, \theta)$  yields the frequency mode number spectrum in (b).

where  $T$  is the duration of the transformed sample. The power spectrum is obtained in the usual way from the Fourier transform after suitable ensemble averaging [59]. The resulting frequency-wave number spectrum in Fig. 2.20 (b) has a dominating peak at  $m = 7$  and at  $f = 2.8$  kHz, as expected. All other spectral components are small. In more complex cases as just one coherent mode, the frequency-mode number spectrum reveals the individual amplitudes of all spectral components.

### Two-probe technique

For coherent waves it is unnecessary to employ a large number of probes. In this case, the wave field can be probed point-by-point with one of two probes, where the other one is fixed and serves as phase reference. This technique is applied to both wave types. For drift waves, the reference signal is obtained from a fixed Langmuir probe in the density gradient region and a movable Langmuir probe is scanned in the azimuthal plane with a positioning system. For Alfvén waves, the  $\vec{B}$ -probes described in Sec. 2.2 are applied. Since the wave is externally excited, the reference signal is derived from the periodically driven antenna current. The positioning of the movable probe is done in the radial-axial plane, to record the axial propagation direction.

An example for the observation of propagating Alfvén waves is given in Fig. 2.21. The excitation antenna is placed on the axis of the cylindrical vessel at the one end of the device, as shown in Fig. 2.21 (a). Alfvén waves generated at the antenna prop-

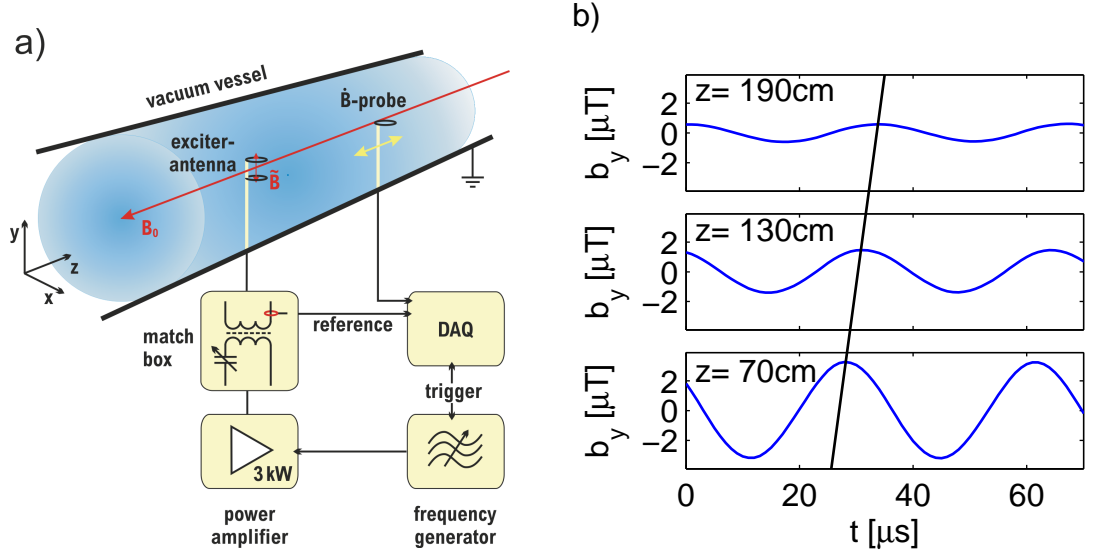


Figure 2.21: (a) setup for spatially resolved measurement of Alfvén waves. The driven wave is detected by a sensor mounted on a positioning system. Wave generation and data recording are started via a trigger system during the discharge. (b) magnetic fluctuations of the wave field, separated from other fluctuations by conditional averaging, have spatially dependent amplitudes and phases.

agate mainly parallel to the ambient magnetic field. The associated magnetic field fluctuations are recorded with a magnetic field sensor mounted on the rz-positioning system. Repositioning of the sensor is done during the off-times of the plasma, which is generated with a duty cycle  $\approx 2\text{ s}$ . Fig. 2.21 (b) shows three time series of  $b_y(t)$  after preprocessing as described in Sec. 2.6. They are recorded at different distances to the launching antenna. The amplitude of  $b_y(t)$  decreases for increasing distances  $z$  and the phase difference to the reference signal increases. Hence, the magnetic field perturbation propagates from the antenna position as damped wave.

### Signal processing of wave field data

The first step in the signal processing is the probe specific calibration (cf. Sec. 2.2.4). After that, the signal from a probe contains besides the actual wave field fluctuations other signal components. These may include broad-band noise and signals from other simultaneously occurring events. Fourier decomposition provides a possible way to separate those from the desired signal. Assuming a coherent wave, components of the wave field are concentrated in a narrow frequency band with higher harmonics. The amplitudes are usually higher than any present broad band fluctuations. One

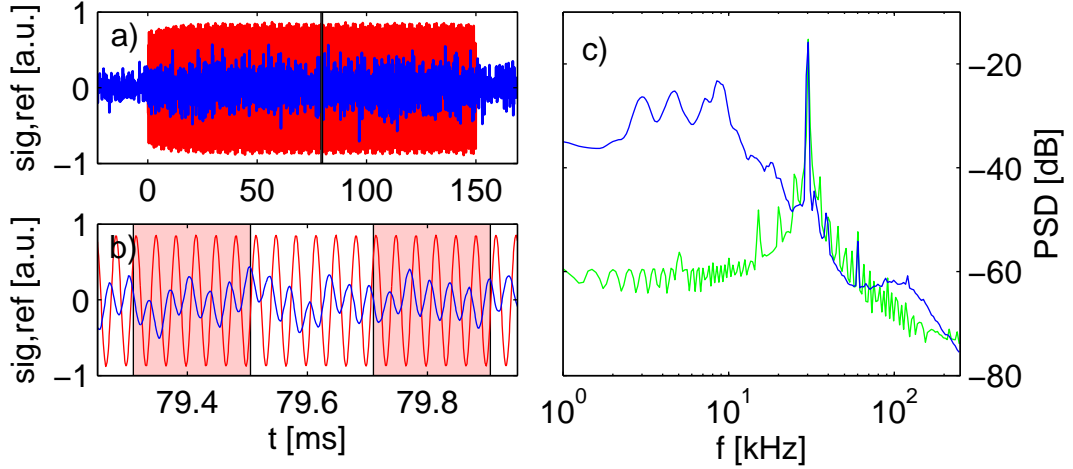


Figure 2.22: Effect of conditional averaging. Within the original time series (a) of signal (blue) and reference (red), trigger points are detected at a certain level of the reference. They define time segments of the signal which are to be averaged, shown in (b), with a shorter time base. In (c), the spectra of the original time series (blue) and the conditional averaged one (green) are compared.

method to separate the wave field from other fluctuations is to consider only the spectral peak at the excitation frequency  $\omega_0$

$$b_j^{\omega_0} = \frac{1}{T} \int_{-T/2}^{T/2} b_j(t) e^{-i\omega_0 t} dt \quad j \in x, y, z \quad . \quad (2.42)$$

The recorded time series  $b_j(t)$  is reduced to a single complex number  $b_j^{\omega_0}$  with amplitude and phase relative to the reference signal.  $T$  is the time length of the recorded time series and defines the band width of this narrow band pass filter as bin width of the Fourier transform  $\Delta f = 1/T$ .

Another possibility to distinguish between wave field and other signal components is conditional averaging, that is applied in the time domain [60]. It is not restricted to harmonic signals, the only requirement is a repetitive wave form in time. A trigger condition in terms of an amplitude window around integer multiples of the standard deviation  $\sigma$  is applied to the reference time series  $U_{\text{ref}}(t)$ . It defines a series of discrete trigger times  $t_0 \dots t_N$ . Segments around them  $t_i - \Delta t/2 \dots t_i + \Delta t/2$  are expected to contain the repeated wave form in the reference as well as in the signal  $U_{\text{sig}}(t)$ , the latter possibly attenuated and time shifted. Averaging yields

$$U(t) = \sum_{i=1}^N U_{\text{sig}} \left( t_i - \frac{\Delta t}{2} \dots t_i + \frac{\Delta t}{2} \right) \quad ,$$

a new time series of length  $\Delta t$  containing only signal parts coherent with the initial wave form. This process is visualized for the Alfvén wave experiment with excitation antenna and detector positioned field-aligned at  $x = 0$ ,  $y = 0$  and  $\Delta z = 190$  cm in Fig. 2.22 (a) and (b). The trigger level is set to  $1.0\sigma$  with a segment length of  $\Delta t = 200\ \mu\text{s}$ . The spectra of the original signal and the conditional averaged signal are compared in Fig. 2.22 (c). Although the component of the original time series at the wave excitation frequency  $f_{\text{exc}} = 30\text{ kHz}$  is dominant, a broad spectral background is present, mainly in the range below 10 kHz. This corresponds to the jumpy run of the sinusoidal time series in Fig. 2.22 (b). Conditional averaging leads to a strong suppression of these low frequency parts, as can be inferred from the spectrum. The absolute value of the main component, on the other hand, is unchanged. Hence, conditional averaging is equivalent to narrow bandpass filtering.

# Chapter 3

## Theoretic background

### 3.1 Alfvén waves

Alfvén waves are observed in magnetized plasmas as magnetic field perturbations that propagate along the ambient magnetic field  $B_0$ . The wave frequency  $\omega$  is restricted to be smaller than the ion-cyclotron frequency  $\omega_{ci} = eB_0/m_i$ , at which Alfvén waves experience a resonance. This wave type was theoretically predicted by Hannes Alfvén in 1942 [10] using a plasma fluid description. Alfvén waves are not only observed in plasmas but may also occur in conducting fluids. In fact the first experimental observations were made in liquid mercury [61, 62] and liquid sodium [63]. Alfvén waves are observed in magnetized plasma experiments [32, 64, 65] and in space plasmas [66–68].

#### 3.1.1 Ideal MHD

Alfvén waves (AWs) can be described within the framework of the ideal MHD model [1, p.95]. The plasma is treated as a conducting fluid with zero resistivity. The basic equations are the linearized fluid equation of motion with neglected convective derivative and the generalized Ohm’s law

$$\rho \frac{\partial \vec{v}}{\partial t} = \vec{j} \times \vec{B}_0 \quad ; \quad \vec{E} + \vec{v} \times \vec{B}_0 = 0 \quad . \quad (3.1)$$

The fluctuating quantities are the velocity of the plasma  $\vec{v}$ , the current density  $\vec{j}$ , and the electric field  $\vec{E}$ . The mass density  $\rho$  and the ambient magnetic field  $\vec{B}_0$  are constant quantities. The gyration of ions is not included in the ideal MHD picture

but significantly influences the properties of AW especially close to the resonance at  $\omega_{ci}$  [69]. Hence, the ideal MHD-description is valid only in the limit  $\omega \ll \omega_{ci}$ . The system in (3.1) is closed by Faraday's law and Ampère's law (with neglected displacement current  $1/c^2 \partial \vec{E} / \partial t$ ).

$$\vec{\nabla} \times \vec{b} = \mu_0 \vec{j} \quad (3.2)$$

$$\vec{\nabla} \times \vec{E} = -\frac{\partial \vec{b}}{\partial t} . \quad (3.3)$$

$\vec{b}$  denotes the fluctuating part of the magnetic field  $\vec{B} = \vec{B}_0 + \vec{b}$ . The resulting system of four coupled first-order linear differential equations with constant coefficients can be solved with a plane wave ansatz

$$\vec{A}(\vec{r}, t) = \vec{A}_0 e^{i(\vec{k} \cdot \vec{x} - \omega t)} , \quad (3.4)$$

where  $\vec{A}$  is any of the fluctuating quantities magnetic field  $\vec{b}$ , electric field  $\vec{E}$ , or current density  $\vec{j}$ . Choosing the ambient magnetic field  $B_0$  in  $z$ -direction, without loss of generality Eqs. (3.1) read to be

$$\begin{aligned} -i\omega\rho v_x &= j_y B_0 & E_x &= -v_y B_0 \\ i\omega\rho v_y &= j_x B_0 & E_y &= v_x B_0 \\ v_z &= 0 & E_z &= 0 \end{aligned} . \quad (3.5)$$

Eliminating the velocity components leads to

$$-i\omega E_y / v_A^2 = \mu_0 j_y \quad (3.6)$$

$$-i\omega E_x / v_A^2 = \mu_0 j_x . \quad (3.7)$$

Here, the Alfvén velocity is introduced as

$$v_A = \frac{B_0}{\sqrt{\mu_0 \rho}} . \quad (3.8)$$

To express  $j_x$  and  $j_y$  in terms of the electric field, Ampère's and Faraday's law in Eqs. (3.2, 3.3) yield

$$\begin{aligned} \mu_0 j_x &= i(k_y b_z - k_z b_y) & -k_z E_y &= \omega b_x \\ \mu_0 j_y &= i(k_z b_x - k_x b_z) & k_z E_x &= \omega b_y \\ \mu_0 j_z &= i(k_x b_y - k_y b_x) & k_x E_y - k_y E_x &= \omega b_z \end{aligned} . \quad (3.9)$$

(3.6) and (3.7) read

$$\begin{aligned} (k_y^2 + k_z^2 - \omega^2 / v_A^2) E_x &= k_x k_y E_y \\ (k_x^2 + k_z^2 - \omega^2 / v_A^2) E_y &= k_x k_y E_x \end{aligned} . \quad (3.10)$$

At this point, it is convenient to introduce the normalized frequency  $f$  and the normalized wave number  $\alpha$  as

$$f = \omega/\omega_{ci} \quad \text{and} \quad \vec{\alpha} = \vec{k}v_A/\omega_{ci} . \quad (3.11)$$

With these normalized quantities (3.10) can be written as

$$\frac{E_x}{E_y} = \frac{\alpha_x \alpha_y}{\alpha_y^2 + \alpha_z^2 - f^2} \quad \frac{E_y}{E_x} = \frac{\alpha_x \alpha_y}{\alpha_x^2 + \alpha_z^2 - f^2} . \quad (3.12)$$

Eliminating  $E_x/E_y$  leads, after some straightforward manipulations, to an implicit relation for  $f$  and  $\alpha$  with two solutions

$$(f^2 - \alpha_z^2)(f^2 - \alpha^2) = 0 \quad \rightarrow \quad \alpha_z^2 = f^2 \quad \vee \quad \alpha^2 = f^2 . \quad (3.13)$$

In physical quantities, the solutions read to be

$$\begin{aligned} \omega/k &= v_A \cos \theta \\ \omega/k &= v_A \end{aligned} \quad \text{with} \quad v_A = \frac{B}{\sqrt{\mu_0 \rho}} . \quad (3.14)$$

Here, the angle  $\theta$  between the wave vector  $\vec{k}$  and the ambient magnetic field  $\vec{B}_0$  is introduced, which allows one to express the parallel component of the wave vector as  $k_z = k \cos \theta$ . Eqs. (3.14) represent the dispersion relation for low frequency waves in a homogeneous plasma. There are two branches: the first one is the so-called shear AW, and the second one is the compressional or fast AW [18]. The phase velocity  $v_{ph} = \omega/k$  is always larger for the fast AW than for the shear AW unless the wave vector  $\vec{k}$  is parallel to  $B_0$  where the two velocities become equal. The group velocity of a propagating wave is defined as

$$\vec{v}_g = \frac{\partial \omega}{\partial \vec{k}} = \vec{e}_x \frac{\partial \omega}{\partial k_x} + \vec{e}_y \frac{\partial \omega}{\partial k_y} + \vec{e}_z \frac{\partial \omega}{\partial k_z} , \quad (3.15)$$

yielding for shear AWs

$$\vec{v}_g = \vec{e}_z v_A . \quad (3.16)$$

Hence, wave packets propagate at the Alfvén velocity  $v_A$  along the ambient magnetic field. Since Eqs. (3.13) are quadratic in  $\omega$ , there exist two solutions  $\vec{k} = \pm v_A \vec{k}$ . The physical meaning is that there is no difference between wave propagation along or opposite to the magnetic field direction. The non-vanishing phase velocity perpendicular to the ambient magnetic field  $B_0$  describes shear AWs on different magnetic field lines with phase differences. A wave field of this form is equivalent to a wave propagating under an angle  $\theta$ , although there is no flow of information across the magnetic field. In the case of fast AWs, the group velocity is  $\vec{v}_g = (v_A^2/\omega)\vec{k}$ . An initial perturbation will propagate isotropically along and across the magnetic field with an absolute value  $v_g = |v_A|$ .

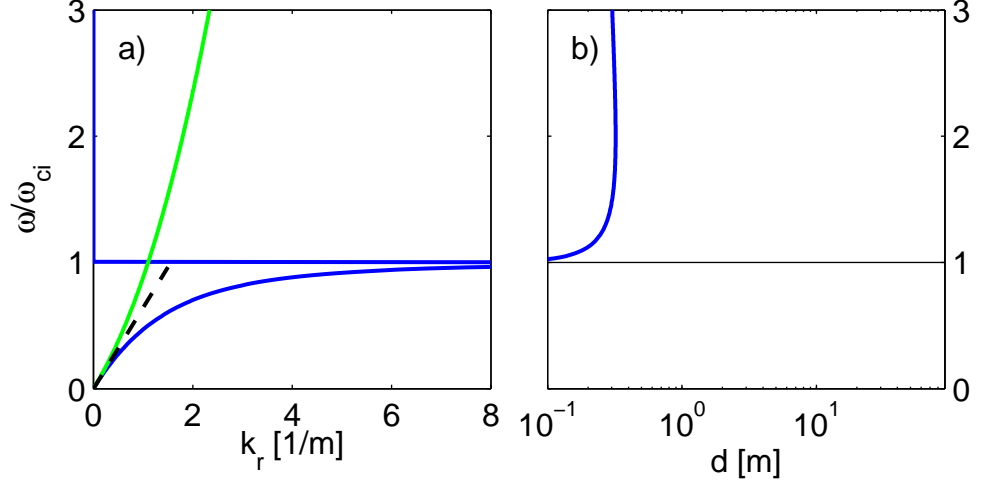


Figure 3.1: (a) Real part of dispersion relation  $k_r(\omega)$  for shear Alfvén waves (blue), fast Alfvén waves (green), and for both waves in the low-frequency limit  $\omega \ll \omega_{ci}$  (dashed). (b) Imaginary part of dispersion relation  $k_i(\omega)$  expressed as damping length  $d = 1/(k_i)$ . For fast waves  $k_i \equiv 0 \rightarrow d = \infty$ .

### 3.1.2 MHD with Hall term

To describe AW in a frequency range close to the ion-cyclotron frequency, the ideal MHD model must be extended by considering the Hall term in the generalized Ohm's law [18]

$$\vec{E} + \vec{v} \times \vec{B} = \frac{1}{ne} \vec{j} \times \vec{B} . \quad (3.17)$$

With this extension, the model is the simplest non-dissipative two-fluid description of a plasma [70]. The Hall term describes electric fields arising from the deflection of ions and electrons to opposite directions when they are located in a current filament immersed in a magnetic field. This effect is mainly attributed to the ions, since they are much heavier than the electrons and have a larger larmor radius. In this way the ion gyro motion enters the model. The Hall-MHD description was successfully applied to fusion [71] and space plasmas [72], where processes at frequencies close to the ion-cyclotron resonance are considered.

The steps to derive the dispersion relation are the same as for the ideal MHD. The details of the calculation are compiled in Appendix A. The result is an implicit relation in the form of a polynomial of 4th degree for  $f$  and  $\alpha$

$$f^4 - f^2(\alpha^2 + \alpha^2 \alpha_z^2 + \alpha_z^2) + \alpha^2 \alpha_z^2 = 0 . \quad (3.18)$$

It is possible to solve the equation analytically. Only the special case of propagation parallel to the magnetic field  $\alpha = \alpha_z$  will be further discussed. The dispersion

relation can be separated into two solutions

$$f^4 - f^2(2\alpha_z^2 + \alpha_z^4) + \alpha_z^4 = 0 \quad (3.19)$$

$$\rightarrow \alpha_{z1}^2 = f^2/(1-f) \quad (3.20)$$

$$\vee \alpha_{z2}^2 = f^2/(1+f) . \quad (3.21)$$

The result is similar to the ideal MHD dispersion (3.13), but with correction terms of the type  $1/(1 \pm f)$ . A diagram of the two solutions for shear and fast AW is shown in Fig. 3.1 (a). For shear AW, the additional factor  $1/(1-f)$  has a pole for  $f = 1$  or  $\omega = \omega_{ci}$ . At this frequency, the wave vector diverges  $k \rightarrow \infty$  and the wave length is infinitely short  $\lambda = 0$ , i.e. the shear AW experiences a resonance at the ion-cyclotron frequency. In contrast, the  $1/(1+f)$  correction in the dispersion relation of fast AWs changes the ideal MHD dispersion only slightly. Instead of a linear dependence  $k(\omega) = \omega/v_A$ , the wave number  $k$  is now quadratic in  $\omega$  with reduced  $k$ -values for a given frequency. (3.19) finds the dispersion relation implicitly. Solutions for  $\omega$  or for  $k$  have different physical pictures: Predefining a real-valued  $k$  results in a possibly complex frequency  $\omega = \omega_r + i\omega_i$ , which represents a *temporally* damped wave with a damping time  $1/\omega_i$ . Conversely, a complex wave vector  $k = k_r + ik_i$  is obtained assuming a real-valued frequency  $\omega$ . The wave is then *spatially* damped with a damping length of  $d = 1/k_i$ . For fast or shear AWs in the low-frequency limit the frequency and wave number are both real-valued. Only for frequencies  $\omega \geq \omega_{ci}$  the AW-dispersion relation for shear AWs (3.20) yields either an imaginary  $k$  or  $\omega$ . Considering a real-valued frequency, the wave is then evanescent with a damping length  $d = 1/k_i$ , as shown in Fig. 3.1 (b). The asymptotic behavior of  $d$  for large frequencies  $f \gg 1$  is determined by neglecting the unity in the denominator of (3.20)

$$\alpha_z^2 = f^2/(1-f) \xrightarrow{f \gg 1} -f \quad \leftrightarrow \quad \alpha_z = i\sqrt{f} . \quad (3.22)$$

By using the normalization introduced in (3.11), the damping length reads

$$d = \frac{1}{k_i} = \frac{v_A}{\omega_{ci} \Im(\alpha_z)} \xrightarrow{f \gg 1} \frac{v_A}{\sqrt{\omega_{ci}\omega}} . \quad (3.23)$$

This expression resembles the skin depth, defined as  $\delta = c/\omega_{pe}$ , with  $c$  being the speed of light in vacuum and  $\omega_{pe}$  the electron plasma frequency. In fact, one would expect a damping length  $\delta$  for waves at high frequencies  $\omega_{ci} \ll \omega \ll \omega_{ce}$ . The plasma shields the electric field of a wave with the mobile electrons. In the framework of the Hall-MHD model, the electron-inertia term is neglected, so the skin depth here is attributed only to the ion motion resulting in (3.23).

An important property of electromagnetic waves in general is their polarization, which is often used to identify an observed wave type [8, 24]. The polarization

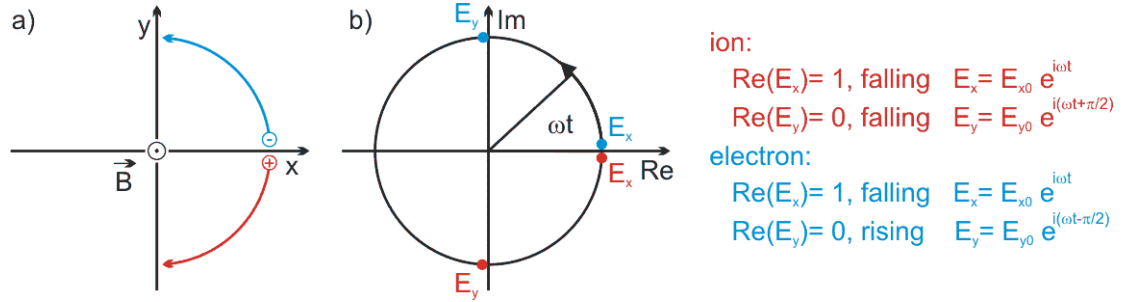


Figure 3.2: (a) Schematic rotation direction of electrons and ions in a magnetic field. (b) Perpendicular components of the electric field for clockwise and counter-clockwise rotation.

is defined as direction of the  $E$ -field vector of the wave, expressed as ratio of the perpendicular vector components. Given by the corresponding dispersion relation (3.19), the ratio of the wave electric field components in (A.15) for AWs propagating along the ambient magnetic fields reads to be

$$\frac{E_x}{E_y} = i \frac{\alpha_z^2 f}{\alpha_z^2 - f^2} = i \frac{f}{1 - f^2/\alpha_z^2} = \begin{cases} +i & \text{shear AW} \\ -i & \text{fast AW} \end{cases} . \quad (3.24)$$

A purely imaginary ratio  $E_x/E_y$  refers to a circularly polarized wave with a rotating wave field vector. A value of  $E_x/E_y = +i$  means left-hand polarization (direction of ion gyration), and  $E_x/E_y = -i$  means right-hand polarization (direction of electron gyration, cf. Fig. 3.2). We conclude, shear AWs are left-hand polarized and fast AW are right-hand polarized.

### 3.1.3 MHD with Hall term and resistivity

No dissipation mechanism is included in either the ideal MHD or the Hall-MHD model. This is not an appropriate description of low-frequency waves in VINETA, since its plasma is typically characterized by a high collision frequency (cf. Sec. 3.2). At least perpendicular to  $B_0$ , the resistivity must be considered in the model since the ion-cyclotron frequency is three orders of magnitude smaller than the Coulomb collision frequency between electrons and ions. The resistivity is included in the generalized Ohm's law as a non-isotropic quantity

$$\vec{E} + \vec{v} \times \vec{B} = \begin{pmatrix} \eta & 0 \\ 0 & \eta \\ 0 & 0 \end{pmatrix} \vec{j} + \frac{1}{ne} \vec{j} \times \vec{B} . \quad (3.25)$$

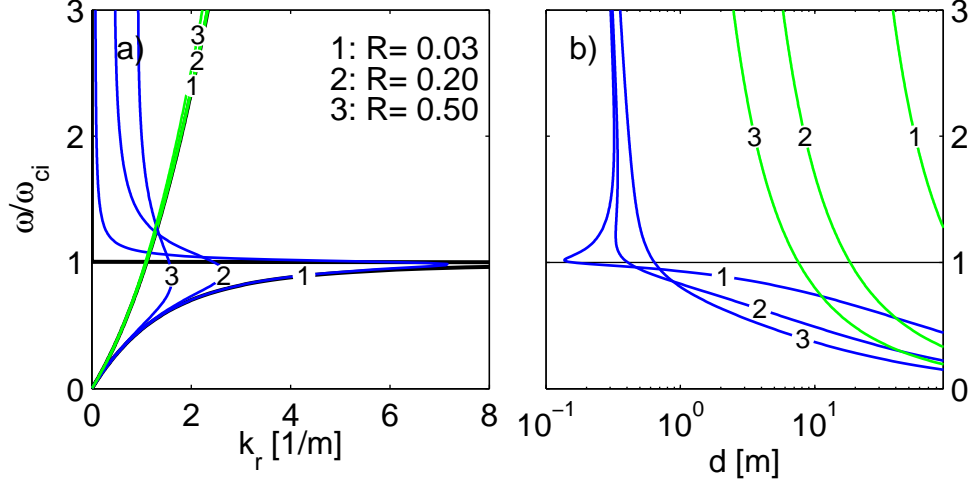


Figure 3.3: Dispersion relation  $k(\omega)$  for shear Alfvén waves (blue) and fast Alfvén waves (green) in the extended MHD theory for different resistivities. Shown are (a) the real part of the dispersion  $k_r$  and (b) the imaginary part expressed as damping length  $d = 1/(ik_i)$ .

Finding a solution of the four coupled differential equations is similar to ideal MHD (cf. Appendix A). The result is the dispersion relation

$$f^4 + f^3 i R (\alpha^2 + \alpha_z^2) - f^2 (\alpha^2 \alpha_z^2 + \alpha^2 + \alpha_z^2 + R^2 \alpha^2 \alpha_z^2) - 2 f i R \alpha^2 \alpha_z^2 + \alpha^2 \alpha_z^2 = 0 \quad , \quad (3.26)$$

with  $R$  denoting the normalized resistivity

$$R = \frac{\eta \omega_{ci}}{\mu_0 v_A^2} \quad . \quad (3.27)$$

In comparison to the collisionless Hall-MHD description, three new terms are present. As polynomial of fourth degree, four solutions are expected. Since analytically cumbersome to obtain, the branches for shear and fast AWs are numerically calculated. Fig. 3.3 shows the dependency of the dispersion relation on the resistivity  $R$  for propagation along the magnetic field ( $\theta = 0$ ). At low frequencies both shear and fast AW experience shorter damping lengths for increased resistivity. At  $\omega = \omega_{ci}$  moderately damped shear AWs with  $R = 0.03$  have a clear minimum of the damping length [branch 1 in Fig. 3.3 (b)], which vanishes for increased plasma resistivity (branch 2 and 3). The shear AW dispersion relation  $\omega(k)$  in Fig. 3.3 (a) remains almost unchanged at low frequencies  $\omega < \omega_{ci}$  by a relatively small resistivity  $R = 0.03$  (branch 1). The maximum wave number  $k$  is finite, associated to a frequency slightly below the ion-cyclotron resonance  $\omega_{ci}$ . The wave number  $k$  is not anymore purely imaginary for  $\omega > \omega_{ci}$ . Resistive shear AW propagate at higher frequencies than  $\omega_{ci}$ , although they are then strongly damped. These effects get more pronounced for increased resistivity. Especially the shift of the highest possible  $k$  to lower frequencies

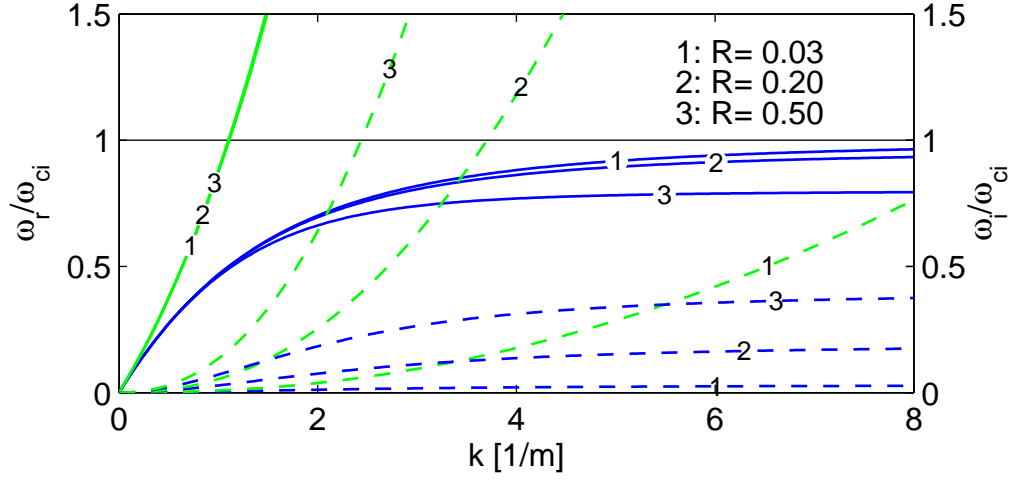


Figure 3.4: Dispersion relation  $\omega(k)$  for shear Alfvén waves (blue) and fast Alfvén waves (green) in extended MHD theory for variation of the resistivity.  $k$  as input parameter is real,  $\omega$  as result complex. The figure shows the real parts of the dispersion  $\omega_r(k)$  as solid lines and the imaginary parts  $\omega_i(k)$  as dashed lines.

becomes more obvious with increased  $R$  and may be interpreted as lowering of the resonance frequency. In the paper of Müller [64] this effect is discussed in detail and attributed to the additional mass loading of ions by ion-neutral collisions. In contrast to shear AWs, resistivity alters the dispersion of the fast AW only slightly. Note that fast AWs have a higher wave length and are less damped for all frequencies, if compared to shear AWs.

In Fig. 3.4 the dispersion relation for shear and fast AW is shown as function  $\omega_r(k)$  with a real-valued wave number  $k$ . The values for  $R$  as parameter are the same as in Fig. 3.3. The imaginary part of the dispersion relation is now expressed as  $\omega_i$ , which can be physically interpreted as an inverse damping time. The phase velocity in the low wave number limit is  $v_A$ , which is concurrent with the ideal MHD description. For higher wave numbers, the frequency stays relatively constant  $\omega \approx \omega_{\max}$  close to the ion-cyclotron resonance frequency. The value for  $\omega_{\max}$  decreases for increasing resistivity. This can be interpreted again as lowering of the wave resonance frequency for increased plasma resistivity. The damping time, on the other hand, decreases with increasing resistivity, as expected.

The propagation angle  $\theta$  of the wave with respect to the ambient magnetic field  $B_0$  has significant influence on the dispersion relation of AWs. The cases  $\theta = 0^\circ$ ,  $50^\circ$ , and  $65^\circ$  are shown for a  $R = 0.1$  in Fig. 3.5. In the limit of small frequencies  $\omega \ll \omega_{ci}$ , the result of the ideal MHD description (cf. Eq. 3.14) is reproduced: For fast AWs, the slope of  $\omega(k)$  and thereby the phase velocity does not change for different angles

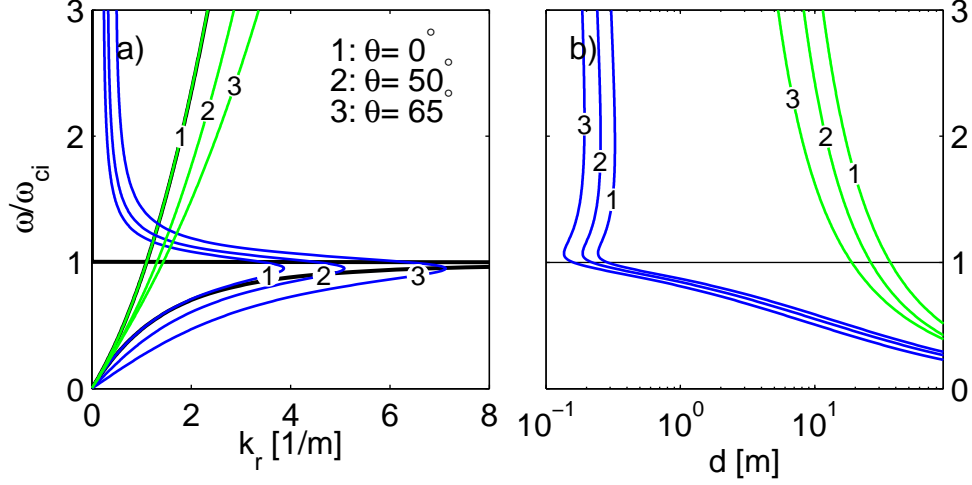


Figure 3.5: Dispersion relation  $k(\omega)$  for shear Alfvén waves (blue) and fast Alfvén waves (green) in extended MHD theory for variation of the angle  $\theta$  between propagation normal and the ambient magnetic field. The figure shows a) the real part of dispersion  $k_r$  and b) the imaginary part expressed as damping length  $d = 1/k_i$  for a small resistivity of  $R = 0.1$ .

(isotropic propagation). In the case of shear AWs the phase velocity decreases for increasing propagation angles, reaching  $v_{ph} = 0$  for  $\theta = 90^\circ$ . Hence, shear AWs do not propagate across the ambient magnetic field. For higher frequencies  $\omega \approx \omega_{ci}$ , the propagation properties of the two wave types change significantly. In Fig. 3.5 (a), a small  $\theta$ -dependency of  $v_{ph}$  is observed for fast AW, breaking the isotropy of non-resistive fast AWs. Shear AWs have a non-zero phase velocity even in the limit  $\theta \rightarrow 90^\circ$  (not shown) and can propagate across the ambient magnetic field. However, the damping is increased for larger angles  $\theta$  ( Fig. 3.5 (b)).

### 3.1.4 Spatial structure of Alfvén waves

The discussed dispersion relations define a solution of the initial system of equations (3.1), (3.2), (3.3). In the following it is numerically solved on a grid in a plane perpendicular to  $B_0$  at a distance  $\Delta z = 2$  m from the excitation point. The dimensions of the plane are chosen to be 4m x 6m. This is much larger than any available laboratory plasma experiment. In the Hall-MHD model an infinite plasma extent is assumed and the extended spatial range is used to include some typical features of the waves. However in a realistic laboratory environment AWs are spatially limited by the plasma boundaries not considered in the model. The space-time evolution of any fluctuating quantity of an AW is described by the plane wave ansatz in (3.4). A vertically fluctuating magnetic field  $b_y$  is considered at the coordinate origin

$x = y = z = 0$  mm. The amplitude was chosen to be  $b_y = 200 \mu\text{T}$ , which is about the experimental excitation amplitude (cf. Sec. 2.5.2). For a point  $\vec{r} = (x, y, z)'$  the  $y$ -component of the fluctuating magnetic field is calculated with the plane wave ansatz. The wave vector  $\vec{k}$  depends on the excitation frequency  $\omega$  and on the propagation angle  $\theta$ . For each point under consideration, it has to be derived separately as

$$\vec{k}(\theta) = |k(\omega)| \cdot \frac{\vec{r}}{r} \quad \text{with} \quad \theta = \arctan\left(\sqrt{x^2 + y^2}/z\right) . \quad (3.28)$$

The magnitude of the wave vector  $|k(\omega)|$  is given by the dispersion relation. For the calculation, the shear AW branch of (3.26) is used. It is obtained from the Hall-MHD model including resistivity. The resulting magnetic fluctuation component  $b_y(x, y, t)$  is shown in Fig. 3.6 (b) for three different time instants. The maximum amplitude is  $8.7 \mu\text{T}$ . For  $0 \mu\text{s}$ ,  $b_y$  has the largest value of  $b_y = 5.5 \mu\text{T}$  in the center of the plane; it is circular symmetric. In  $x$ -direction at  $y = 0$ , the maximum in the center is followed by a minimum of  $b_y = -3.8 \mu\text{T}$  at  $x = 1.18$  m and by a second local maximum with  $b_y = 1.02 \mu\text{T}$  at  $x = 1.92$  m. The component  $b_y$  decreases in amplitude and wave trains follow each other with decreasing distance.

Both effects can be attributed to the dependence of the wave vector  $k(\theta)$  on the propagation angle. It is found to have a value of  $k = 2\pi/1.71 \text{ m} + i/0.65 \text{ m}$  in the center of the plane, which means that the wave is damped to a fraction of  $\exp(2/0.65) = 0.045$  of its original value. For the next maximum at  $x = 1.92$  m, the wave vector has a larger value of  $k = 2\pi/1.47 \text{ m} + i/0.35 \text{ m}$ . Due to the propagation angle of  $\arctan(1.92/2) = 44^\circ$ , the wave length gets smaller and the damping larger (cf. Fig. 3.5). Together with the larger propagation distance of  $\sqrt{2^2 + 1.92^2} \text{ m} = 2.77 \text{ m}$ , the wave is strongly damped to a fraction of 0.003 of the excitation amplitude while the phase is changed by  $2\pi$  in comparison with the propagation in the center. Since  $k$  increases with increasing angle  $\theta$ , the lengths of wave trains in perpendicular direction are consequently decreasing.

From  $b_y$ , the electric field in  $x$ -direction can be estimated with (3.9) as

$$E_x = b_y \cdot \omega/k_z(\omega) . \quad (3.29)$$

For a given frequency, the parallel wave number is independent of the propagation direction. The electric field  $E_x(x, y)$  in Fig. 3.6 (d) has consequently the same spatial structure as  $b_y$ . The maximum value in the center of the plane for  $t = 0 \mu\text{s}$  is  $0.43 \text{ V/m}$ .

The other perpendicular component of the electric field  $E_y$  is calculated with (A.14). In the simplest case of ideal MHD with no resistivity, it can be simplified to

$$E_y/E_x = k_y/k_x . \quad (3.30)$$

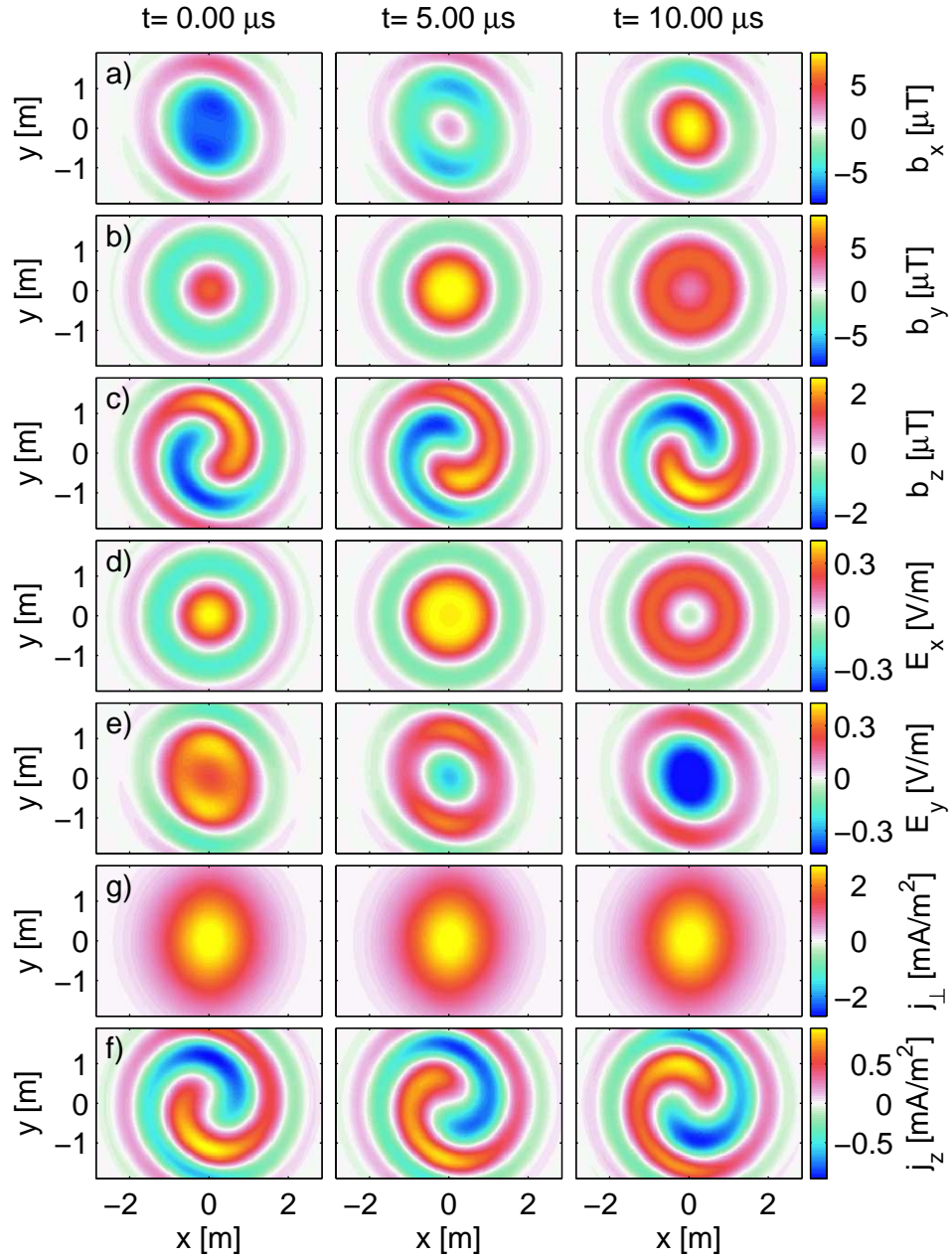


Figure 3.6: Dynamic fields and currents of an AW obtained with the Hall-MHD description including resistivity. The parameters of the model are the frequency  $f = 35 \text{ kHz}$  with  $f/f_{ci} = 0.91$ , the plasma density  $n = 5 \cdot 10^{18} \text{ m}^{-3}$ , the ambient magnetic field  $B_0 = 100 \text{ mT}$ , and the normalized resistivity  $R = 0.1$ . The calculated plane has a distance of  $\Delta z = 2 \text{ m}$  from the excitation in the form of a predefined  $b_y$ -perturbation of  $200 \mu\text{T}$ . From top to bottom, the quantities are the magnetic field components (a, b, c), the perpendicular electric field components (d, e), and the perpendicular and parallel currents (f, g). The time evolution is shown for the three time instants with  $\Delta t = f^{-1} = 5.0 \mu\text{s}$ .

This simple expression already depends on the specific point in the plane since  $k_x = k_x(x)$  and  $k_y = k_y(y)$ . The resulting field  $E_y(x, y)$  is shown in Fig. 3.6 (e). It has no longer the symmetry features of  $E_x$ , instead it displays an elongated structure. Hence, the perpendicular wave lengths depend on the chosen direction within the plane although the distances between maxima and minima are comparable to those of  $E_x$  and  $b_y$ . The maximum value of  $E_y$  is 0.43 V/m as for  $E_x$ . The relation between  $E_y$  and  $b_x$  is (cf. Eq. 3.9)

$$b_x = -E_y \cdot k_z(\omega)/\omega \quad . \quad (3.31)$$

It is again a complex factor that is independent of the position in the plane and results in the same structure for  $b_x(x, y)$  in Fig. 3.6 (a) as for  $E_y(x, y)$  in Fig. 3.6 (e). The maximum value of  $b_x$  is  $8.1 \mu\text{T}$ , which is in the same range of the corresponding component  $b_y$ .

The third component of the magnetic field  $b_z(x, y)$  in Fig. 3.6 (c) is obtained from the perpendicular components of the electric field (cf. Eq. 3.9)

$$b_z = \frac{k_x}{\omega} E_y - \frac{k_y}{\omega} E_x \quad . \quad (3.32)$$

The resulting field has a complex spatial structure. The maximum value is  $b_z = 2.5 \mu\text{T}$  and is, thus, significantly smaller than that for the perpendicular magnetic field components. For each time instant, regions of positive and negative  $b_z$  with a shape of two intersecting spirals can be distinguished. The amplitudes of the spirals decrease for increasing distance from the center of the plane.

The fluctuating magnetic field components are associated with currents given by Ampères law (3.2). The parallel current amplitudes  $j_z(x, y)$  and the perpendicular current amplitude  $j_\perp = \sqrt{j_x^2 + j_y^2}$  are shown in Fig. 3.6 (f) and (g). For the parallel component  $j_z(x, y)$  in Fig. 3.6 (g) a similar spiral-like shape as for  $b_z$  is obtained. The parallel current is bipolar and has a maximum of  $j_z = \pm 0.96 \text{ mA/cm}^2$ . The current density decreases significantly for larger distances from the center of the plane. At  $x = 1.53 \text{ m}$ , it is  $j_z = 0.50 \text{ mA/cm}^2$  and decreases at  $x = 2.64 \text{ m}$  to  $j_z = 0.06 \text{ mA/cm}^2$ . This decrease reflects the increased damping of the shear AW at large propagation angles  $\theta$ . The same holds for the perpendicular current  $j_\perp = \sqrt{j_x^2 + j_y^2}$  (Fig. 3.6 (f)). It is found to have a maximum in the center with a peak value of  $j_\perp = 2.83 \text{ mA/cm}^2$ , decreasing with a similar slope as the parallel current for increased distance from the propagation-axis. The peak value on-axis is significantly larger than that of the parallel current. This underlines the important role of  $j_\perp$  when approaching  $\omega_{ci}$ . A more comprehensive discussion of the current structure of AWs follows in the subsequent Sec. 3.1.5. The  $E_z$  component of the electric field is not shown since it vanishes due to zero parallel resistivity in (3.25).

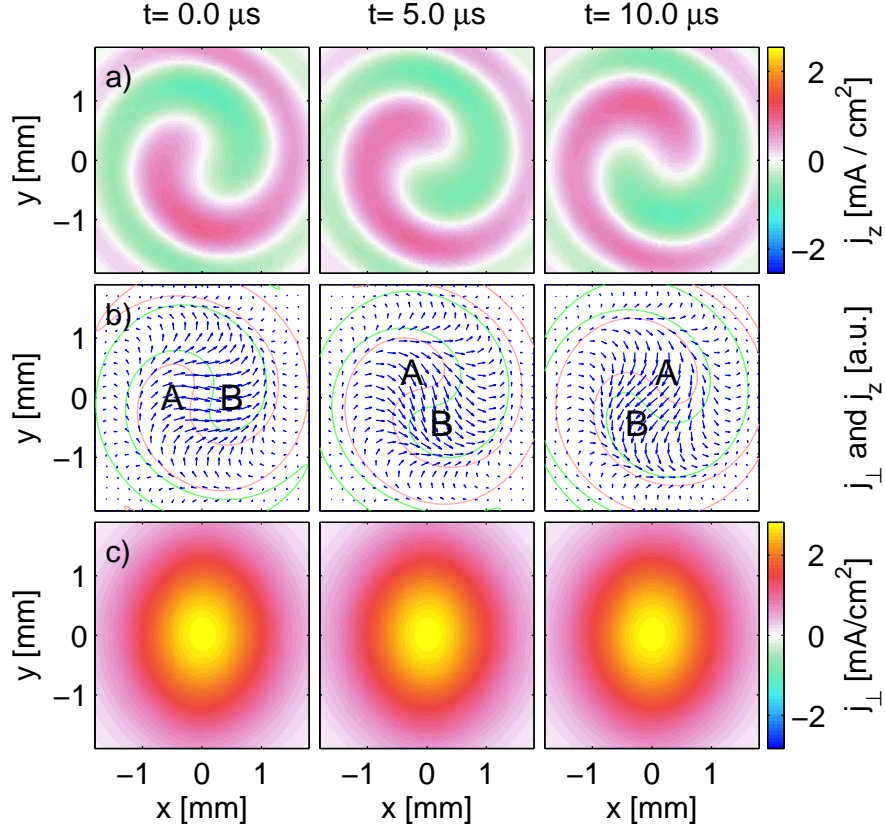


Figure 3.7: The dynamic of parallel and perpendicular currents of shear AWs as obtained from the Hall-MHD description. The parameters of the model are the same as in Fig. 3.6. (a) The parallel currents have the form of a rotating spiral. (b) Vector field representation of  $j_{\perp}$  with isolines of  $j_{\parallel}$  (threshold  $j_{\parallel} = \pm 0.23 \text{ mA/cm}^2$ ). (c) The amplitude of perpendicular currents  $j_{\perp}$  peaks in the center.

### 3.1.5 Shear AW assolution of Hall-MDH model

The solutions of the MHD-equations reveal details of the AW propagation. For a given frequency, all electric and magnetic wave fields can be derived from one fluctuating wave quantity as shown in the last Sec. 3.1.4. In this way an AW is fully determined by the current flows, i.e. electron current parallel and ion polarization current perpendicular to the ambient magnetic field.

The parallel current pattern shown in Fig. 3.6 (f) has a spiral structure with two distinct regions: one with flow in the direction of  $B_0$ , the other with flow in the opposite direction. The spiral current structure rotates in the  $xy$ -plane clockwise,

like the ion gyro direction, characterizing the wave as L-wave. The time dependence of  $j_{\parallel}(t)$  that yields  $E_{\perp}(t)$  is mainly due to the rotation of the structure. Its shape does not significantly change during one period. The decrease of the parallel currents in the outer regions is due to increased damping of the shear AW at large propagation angles  $\theta$ . The damping length for  $\theta = 0$  is  $d = 2.46$  m, decreasing for increasing  $\theta$ . Due to the point source at  $z = 0$ , the pattern forms a cone along the ambient magnetic field in which the shear AW propagates. These so-called Alfvén-cones are a well-known property [73]. The perpendicular currents  $j_{\perp}$  have a peak value of  $2.83 \text{ mA/cm}^2$ . This is approximately three times larger than that of the parallel current for the chosen excitation frequency of  $\omega/\omega_{ci} = 0.91$ . The pattern of perpendicular current amplitude  $|j_{\perp}|$  in the azimuthal plane at  $z = 2$  m is almost rotationally symmetric, without any time dependence. For the time instant  $t = 0 \mu\text{s}$ , the direction of the perpendicular currents can be inferred from Fig. 3.7 (b). The spiral-shaped parallel current structure are superimposed on the vector representation of  $j_{\perp}$  as equicontours. For  $t = 0$  ms the local velocity is directed upwards at position A and downwards at position B. The parallel current flow at these points is out of the plane in A and into the plane in B. In contrast, the local perpendicular currents flow into the same direction (from left to right) at the two points, as can clearly be inferred from Fig. 3.7 (b).

### 3.1.6 Shear and fast AW as solution of Hall-MHD model

Similar to the previous section the Hall-MHD model with resistivity gives insight into the structure of fast AWs. The only difference is the use of the fast AW branch of the dispersion relation (3.26) to obtain  $k(\omega)$  in (3.28). All other steps are the same. The result is shown in Fig. 3.8 (b). For comparison the parallel current of shear AWs is shown in Fig. 3.8 (a). All model parameters are the same as so far discussed, the only difference to Fig. 3.6 is the enlarged spatial area with  $x = \pm 12$  m and  $y = \pm 7$  m to cover significant features of the two wave types.

For the fast AW, the current pattern has a similar shape, but different properties. First of all, the spatial dimensions are larger as expected from the smaller wave vectors in the dispersion. The first two maxima along the  $x$ -axis at  $y = 0$  m have a distance of  $1.14$  m for shear AWs and  $4.39$  m for fast AW. The spatial orientation of the spirals is reversed for fast AWs and the whole structure rotates counterclockwise as expected (cf. Eq. 3.24). The absolute parallel current density for fast AWs has a maximum of  $15.5 \text{ mA/cm}^2$ , located close to the boundary. Fast AWs are much less damped compared with shear AWs (Sec. 3.1.3), which explains the difference in the absolute amplitude of both wave types by one order of magnitude. In contrast to shear AWs fast AWs propagate isotropically along and across the ambient mag-

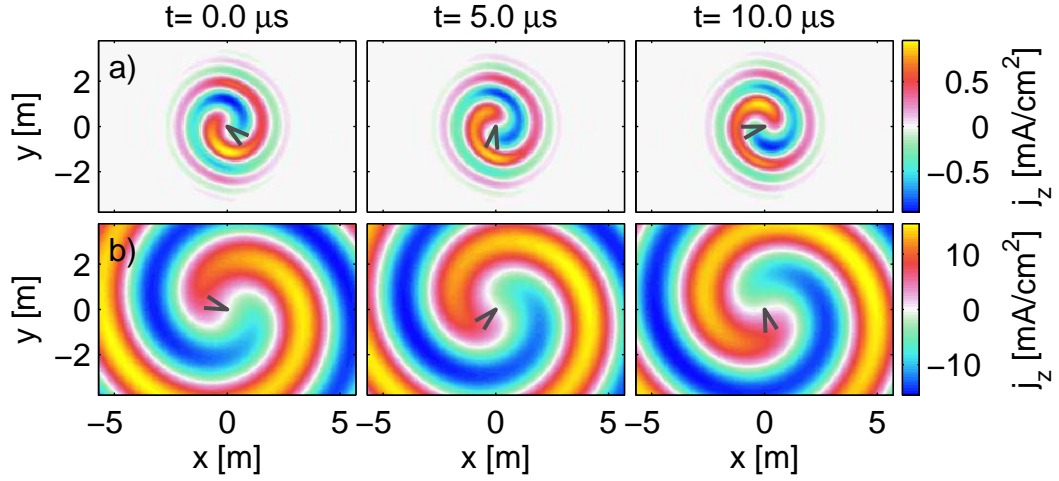


Figure 3.8: Time evolution of parallel currents of shear AW (a) and fast AW (b), calculated with the Hall-MHD model including resistivity. The parameters of the model are the same as in Fig. 3.6.

netic field (cf. Eq. 3.14). Therefore the MHD-solution does not show vanishing wave amplitudes as for shear AWs at larger distances  $> 1$  m from the axis.

## 3.2 Drift instability

Bounded plasmas have gradients in plasma parameters like density or temperature. Those gradients are sources of free energy, able to drive a variety of plasma instabilities [74, 75]. Examples in magnetized plasmas are Kelvin-Helmholtz and Rayleigh-Taylor type instabilities [76, 77] as well as the drift instability [78–80]. Drift waves are of special importance since they occur in the edge regions of thermonuclear fusion plasmas [81, 82]. They are candidates for explaining the anomalous cross-field transport [83]. Plasma fluctuations due to drift instability were observed first in linearly magnetized plasmas [84–86]. In a comprehensive analysis of the fluctuations observed in the plasma of the VINETA experiment [53] drift waves were identified as the instability mechanism [87]. In the following sections, the physical mechanism and a simple model of the drift instability are introduced.

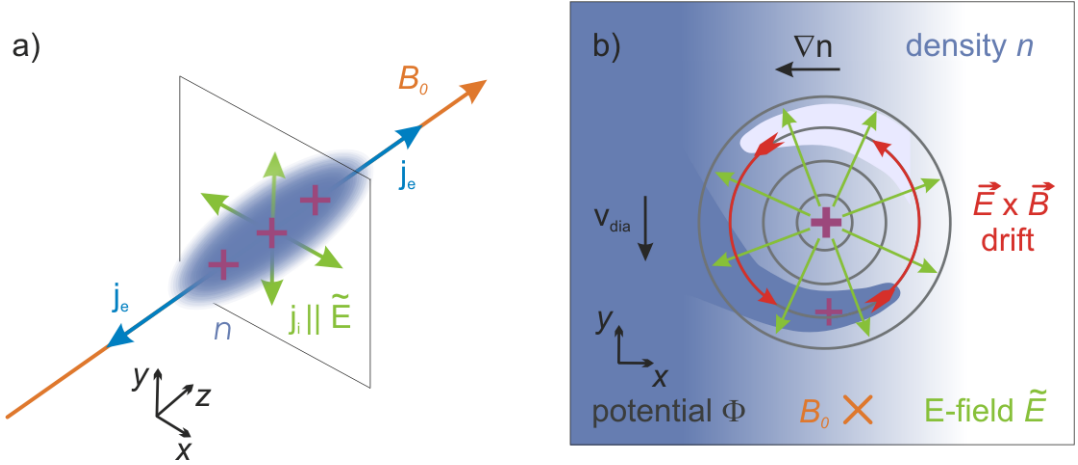


Figure 3.9: Schematic of the drift wave mechanism. The parallel electron current is associated with an ion polarization current in perpendicular direction (a). The resulting potential perturbation  $+\phi$  causes an  $\vec{E} \times \vec{B}$  drift (b).

### 3.2.1 Drift wave instability mechanism

The basic mechanism of the drift instability can be explained in local slab geometry. The starting point is a positive density perturbation  $\tilde{n} > 0$  located in the gradient region of the background density  $n_0(r)$ , as illustrated in Fig. 3.9 (a). The gradient of the plasma density parallel to the magnetic field is a driving force for diffusion of plasma into the regions with lower density. Due to their high mobility, this process is much faster for electrons than for ions resulting a fluctuating positive space charge  $\tilde{\phi} > 0$ . This limits the free electrons motion and drives at the same time a perpendicular ion polarization current, which is proportional to the time derivative of the plasma potential

$$j_{\text{pol}} = \frac{m_i}{eB^2} \dot{\vec{E}}_{\perp} = \frac{m_i}{-eB^2} \nabla_{\perp} \dot{\phi} . \quad (3.33)$$

This current also exists for electrons but is negligible due to their small mass. The space charge is associated with a perpendicular electric field  $\vec{E} = -\nabla_{\perp} \phi$ , as illustrated in Fig. 3.9 (b). The resulting  $\vec{E} \times \vec{B}$  drift convects dense plasma in the density gradient radially outwards. Due to the convection, the initial density perturbation propagates perpendicular to the density gradient in electron diamagnetic drift direction. The phase lag between density and potential perturbation is crucial for the evolution of the instability as discussed below.

### 3.2.2 Basic equations of two-fluid theory

In the two-fluid plasma description [88], drift waves can be described using the continuity equation for ions and electrons

$$\frac{\partial n_\alpha}{\partial t} + \nabla \cdot (n_\alpha \vec{v}) = d_t n_\alpha + n_\alpha \nabla \cdot \vec{v} = 0 \quad (3.34)$$

and the momentum transport equations for ions and electrons

$$nm_\alpha d_t \vec{v}_\alpha = qn(\vec{E} + \vec{v}_\alpha \times \vec{B}) - \nabla p - n\nu_{\alpha n} m_\alpha \vec{v}_\alpha \quad (3.35)$$

with  $\alpha \in \{e, i\}$ . (3.35) balances for each species the acceleration on the left hand side with the acting forces (Lorentz force, pressure gradient, friction with neutrals) on the right hand side. The charge  $q$  is  $\pm e$ , assuming singly ionized ions.

#### Scale parameter of drift waves and drift ordering

Drift waves are driven by the density gradient, which is characterized by the length scale

$$L_n \equiv -\frac{n_0}{\nabla n_0} . \quad (3.36)$$

In some cases, it is more convenient to use the inverse gradient length  $\kappa_n \equiv L_n^{-1}$ . The typical scale length of drift waves is given by the ion Larmor radius taken at the electron temperature

$$\rho_s \equiv \frac{\sqrt{k_B T_e m_i}}{eB} = \frac{c_s}{\omega_{ci}} \quad \text{with} \quad c_s = \sqrt{\frac{k_B T_e}{m_i}} \quad \text{and} \quad \omega_{ci} = \frac{eB_0}{m_i} . \quad (3.37)$$

Based on the drift scale length  $\rho_s$  a normalization can be defined as

$$\hat{l} = \frac{l}{\rho_s} \quad \rightarrow \quad \partial \hat{l} = \frac{1}{\rho_s} \partial l \quad \text{or} \quad \hat{\nabla} = \rho_s \nabla . \quad (3.38)$$

An general estimate of drift wave related quantities is given in [89, p.20], the so-called drift ordering

$$\frac{\omega}{\omega_{ci}} \sim \frac{k_{\parallel}}{k_{\perp}} \sim \frac{\tilde{n}}{n_0} \sim \frac{\rho_s}{L_{\perp}} \sim \frac{e\tilde{\phi}}{k_B T_e} \sim \delta \ll 1 \quad (3.39)$$

with  $\delta$  as smallness parameter. For example, drift wave fluctuations of the plasma density  $\tilde{n}$  are small compared to the equilibrium plasma density  $n_0$ .

### Perpendicular force balance

Crossing the momentum transport equation (3.35) for ions with  $\vec{B}_0$  from the right and assuming  $\vec{v}_i = \vec{v}_\perp$  yields

$$v_{\perp i} = \underbrace{\frac{\vec{E} \times \vec{B}}{B^2}}_{v_E} - \underbrace{\frac{k_B T_i}{enB^2} \nabla n \times \vec{B}}_{v_{\text{dia}}} + \underbrace{\frac{m_i}{eB^2} d_t^{E \times B} E_\perp}_{v_{\text{pol}}} - \underbrace{\frac{\nu_{in} m_i}{eB^2} E_\perp}_{v_{\text{Ped}}} . \quad (3.40)$$

The total perpendicular ion velocity is a superposition of the  $\vec{E} \times \vec{B}$  drift  $v_E$ , the diamagnetic drift  $v_{\text{dia}}$ , the polarization drift  $v_{\text{pol}}$ , and the Pederson current  $v_{\text{Ped}}$  [90]. A well-accepted practise is the replacement of the overall perpendicular velocity  $v_\perp$  in the nonlinear term of the convective derivative by the  $E \times B$  velocity [91]

$$d_t^{E \times B} = \partial_t + \vec{v}_E \cdot \nabla . \quad (3.41)$$

An estimation for  $v_\perp$  can be found in [83, p.9], yielding  $v_E$  as the dominant component of  $v_\perp$  for  $\omega < \omega_{ci}$ . This condition is fulfilled due to the drift ordering (3.39) and the approximation (3.41) can be used in (3.40) for the polarization drift term, allowing an iterative solution of this differential equation in  $v_\perp$ . A similar relation like (3.40) can be derived for the perpendicular electrons velocity. Due to their smaller mass the polarization term and the collision term are neglected.

$$v_{\perp e} = \underbrace{\frac{\vec{E} \times \vec{B}}{B^2}}_{v_E} + \underbrace{\frac{k_B T_e}{enB^2} \nabla n \times \vec{B}}_{v_{\text{dia}}} \quad (3.42)$$

Although the dominant perpendicular velocity  $v_\perp$  is the  $E \times B$  velocity also for electrons, it does not result in a current since it is exactly the same for electrons and ions. The main perpendicular current is the ion polarization current [92].

### Parallel force balance

For electrons and ions at rest, the force balance parallel to  $\vec{B}_0$  is derived from (3.35)

$$m_\alpha d_t \vec{v}_\alpha = q \vec{E} - \frac{1}{n} \nabla p . \quad (3.43)$$

Due to their much smaller mass, the parallel dynamics are fully governed by electrons. Ion motion is of importance only perpendicular to the magnetic field. The

nonlinear term in the convective derivative in (3.35) can be neglected [93, p.75], the parallel component for electrons reads then

$$\underbrace{\frac{m_e}{e}\partial_t j_{\parallel}}_{f_1} = \underbrace{-en\nabla_{\parallel}\phi}_{f_2} + \underbrace{-en\partial_t\psi}_{f_3} - \underbrace{k_B T_e \nabla_{\parallel} n}_{f_4} - \underbrace{-en\eta j_{\parallel}}_{f_5} . \quad (3.44)$$

In this parallel force density balance the electric field is expressed as  $E_{\parallel} = -\nabla\phi - \partial_t\psi$ , where  $\psi$  is the parallel component of the vector potential  $\vec{A}$  of the magnetic field

$$\vec{b} = -\nabla \times \vec{A} \quad \psi \equiv A_{\parallel} . \quad (3.45)$$

Further, the plasma resistivity  $\eta \equiv m_e \nu_{en}/e^2 n$  is introduced. The force density acting on the electrons ( $f_1$ ) consists of four terms: The driving force is the parallel density gradient  $f_4$ . The friction force ( $f_5$ ) damps currents. The fluctuating magnetic field and the corresponding vector potential  $\psi$  in the induction term ( $f_3$ ) are generated by the parallel currents, given by Ampère's law  $\mu_0 j_{\parallel} = \nabla_{\perp}^2 \psi$ . In this way  $f_3$  is determined by  $j_{\parallel}$ , an increased parallel current causes a larger induction force. The term  $f_2$  is the restoring force of the potential  $\phi$ . In the following the magnitude of all terms  $f_{1-5}$  is estimated, partly on the base of drift ordering (3.39). For example the density gradient force is approximately

$$|f_4| = k_B T_e \nabla_{\parallel} n \approx k_B T_e \kappa_{n\parallel} n = \frac{n k_B T_e \mu_0 \kappa_{n\parallel} B^2}{B^2 \mu_0} = \beta \frac{\kappa_{n\parallel} B}{\mu_0} . \quad (3.46)$$

The plasma- $\beta$  is given by  $\beta = n k_B T_e / (\mu_0 B^2)$ , the ratio between kinetic and magnetic pressure. Since the typical spatial scale of the parallel drift dynamics is determined by the machine length [42],  $\kappa_{n\parallel}$  is estimated based on the assumption, that one wave length  $\lambda_{\parallel} = 2\pi/k_{\parallel}$  fits into the discharge chamber. Measured density perturbations are typically small with  $\tilde{n}/n_0 = 10\%$ , so the parallel density is  $n(z) = n_0 + 0.1n_0 \sin(k_{\parallel} z)$ , resulting in an inverse gradient length of  $\kappa_{n\parallel} \approx 0.1k_{\parallel} = 0.16 \text{ m}^{-1}$ . The terms  $f_1 \dots f_5$  in (3.44) can be estimated as above:

$$\begin{array}{llll} f_1 & \approx & \omega/\omega_{ce} & j_{\parallel} B \\ f_2 & \approx & \beta & \kappa_{n\parallel} B/\mu_0 B \\ f_3 & \approx & \beta \omega/\omega_{ci} & j_{\parallel} B \\ f_4 & \approx & \beta & \kappa_{n\parallel} B/\mu_0 B \\ f_5 & \approx & \nu_e/\omega_{ce} & j_{\parallel} B \end{array} . \quad (3.47)$$

For typical plasma parameters in VINETA, the terms are compiled in Tab. 3.1.  $f_1$  has the smallest amplitude of  $7.1 \cdot 10^{-5} \text{ N/m}^{-3}$ , two orders of magnitude smaller than the other ones: Electrons are not significantly accelerated in parallel direction. This

Table 3.1: Parameters and estimation of force densities acting in the parallel momentum transfer equation for electrons (3.44)

input parameters			estimated force densities		
$B_0$	=	0.07 T	$f_1 \approx$	$7.1 \cdot 10^{-5}$	N/m <sup>-3</sup>
$\kappa_{n\parallel}$	=	0.15 m <sup>-1</sup>	$f_2 \approx$	$2.1 \cdot 10^{-1}$	N/m <sup>-3</sup>
$\kappa_{n\perp}$	=	30 m <sup>-1</sup>	$f_3 \approx$	$1.7 \cdot 10^{-3}$	N/m <sup>-3</sup>
$\omega$	=	$1.26 \cdot 10^4$ s <sup>-1</sup>	$f_4 \approx$	$2.1 \cdot 10^{-1}$	N/m <sup>-3</sup>
$\omega_{ci}$	=	$1.69 \cdot 10^5$ s <sup>-1</sup>	$f_5 \approx$	$2.9 \cdot 10^{-2}$	N/m <sup>-3</sup>
$\omega_{ce}$	=	$1.23 \cdot 10^{10}$ s <sup>-1</sup>			
$\nu_{en}$	=	$5 \cdot 10^6$ s <sup>-1</sup>			
$\beta$	=	$3.3 \cdot 10^{-4}$			
$j_{\parallel}$	=	100 mA/m <sup>2</sup>			

justifies approximating of the total time derivative  $d_t$  by the partial time derivative  $\partial_t$  in (3.44). The driving and the restoring force  $f_4$  and  $f_2$  are strongest for the given parameters. A more detailed analysis reveals a small difference between the two terms: The friction force  $f_5 = 2.9 \cdot 10^{-2}$  N/m<sup>-3</sup> is about one order of magnitude smaller than the driving force and dissipates the perturbation energy. The transfer of wave energy into magnetic field fluctuations is given by the induction force  $f_3 = 1.7 \cdot 10^{-3}$  N/m<sup>-3</sup> one order of magnitude smaller than the friction force. It can be neglected in the collision-dominated VINETA plasma. This is different in collisionless plasmas, in which a significant amount of energy is transferred to and from the magnetic field. In this case the drift waves are so-called drift-Alfvén waves [14].

### 3.2.3 The Hasegawa-Wakatani model

The general two-fluid plasma description in (3.34) and (3.35) can be strongly simplified. The full dynamics of drift waves is defined by (i) the drift waves currents under the condition of quasi-neutrality and (ii) the density equation based on one of the continuity equations (3.34).

### drift wave currents

Electron and the ion currents are coupled by the quasineutrality condition  $n_e \approx n_i$ , which can be expressed by combining the two continuity equations (3.34)

$$\nabla \cdot \vec{j} = \nabla_{\perp} \cdot \vec{j}_{\perp} + \nabla_{\parallel} \cdot \vec{j}_{\parallel} = 0 \quad . \quad (3.48)$$

This current-balance with perpendicular currents balancing parallel currents reflects the drift wave mechanism [cf. Fig. 3.9 (a)]. As stated in sec. 3.2.2 the perpendicular current is mostly due to the ion polarization drift  $j_{\perp} = nev_{\text{pol}}$ . In terms of the electric potential  $\phi$  (cf. Eq. 3.40) the current-balance then reads to be

$$\nabla_{\perp} \frac{nm_i}{B_0^2} d_t^{E \times B} \nabla_{\perp} \phi = \nabla_{\parallel} j_{\parallel} \quad (3.49)$$

$$\leftrightarrow \frac{nm_i}{B_0^2} d_t^{E \times B} \Omega = \nabla_{\parallel} j_{\parallel} \quad . \quad (3.50)$$

The vorticity  $\Omega = -\nabla \times \vec{v}_{\perp}$  is introduced as follows. Convection by  $E \times B$  drift yields a vorticity

$$\Omega = -\nabla \times \vec{v}_E = -\nabla \times [\vec{E} \times (\vec{B}/B^2)] = -\nabla_{\perp} \cdot \vec{E}_{\perp}/B = \nabla_{\perp}^2 \phi/B \quad . \quad (3.51)$$

The perpendicular gradient and the total time derivative in (3.49) can be exchanged in drift-ordering [94, p.17]. The parallel electron current divergence on the right-hand side is determined by (3.44). Neglecting the coupling to magnetic perturbations ( $f_3$ ) and the acceleration of electrons ( $f_1$ ), the parallel electron current reads to be

$$j_{\parallel} = \frac{k_B T_e}{e\eta} \nabla_{\parallel} \left( \frac{e\phi}{k_B T_e} - \ln n \right) \quad . \quad (3.52)$$

Substituting the parallel current in (3.50) leads to

$$\frac{m_i n}{B_0^2} d_t^{E \times B} \Omega = \nabla_{\parallel} \frac{k_B T_e}{\eta} \nabla_{\parallel} \left( \frac{e\phi}{k_B T_e} - \ln n \right) \quad . \quad (3.53)$$

This equation is known as vorticity equation of the Hasegawa-Wakatani model [95].

### drift wave density equation

The second equation of the Hasegawa-Wakatani system describes the evolution of the density and can be derived from the electron continuity equation

$$d_t^{E \times B} n = -n \nabla \cdot \vec{v} = -n \underbrace{(\nabla_{\parallel} v_{\parallel} + \nabla_{\perp} \cdot \vec{v}_{\perp})}_{=0} \approx \frac{1}{e} \nabla_{\parallel} j_{\parallel} \quad . \quad (3.54)$$

As stated in sec.3.2.2 the main perpendicular drift is the  $E \times B$  drift, causing the second term in (3.54) to vanish in a constant magnetic field

$$\nabla_{\perp} \vec{v}_{E \times B} = \nabla(\vec{E} \times \vec{B}/B^2) = -\vec{E}(\nabla \times \vec{B}/B^2) + \vec{B}(\nabla \times \vec{E}) = 0 \quad . \quad (3.55)$$

Substituting the parallel current in (3.54) by (3.52) yields

$$d_t^{E \times B} n = \nabla_{\parallel} \frac{k_B T_e}{e\eta} \nabla_{\parallel} \left( \frac{e\phi}{k_B T_e} - \ln n \right) \quad . \quad (3.56)$$

### normalization

The vorticity equation (3.53) and the density equation (3.56) describe the full three dimensional dynamics of drift waves. They are coupled via the term  $\nabla_{\parallel} \ln n$ . By introducing the dimensionless variables

$$\begin{aligned} \hat{t} &= \omega_{ci} t & d_t^{\hat{E} \times B} &= \frac{\rho_s}{c_s} d_t^{E \times B} & \hat{\nu} &= \frac{\nu}{\omega_{ce}} & \hat{\Omega} &= \hat{\nabla}_{\perp}^2 \hat{\phi} \\ \hat{\phi} &= \frac{e\tilde{\phi}}{k_B T_e} & \hat{n} &= \frac{\tilde{n}}{n_c} & \hat{\nabla} &= \rho_s \nabla \end{aligned}$$

with  $n_c$  as typical constant density the system can be transformed into

$$d_t^{\hat{E} \times B} \hat{n} = \hat{\nabla}_{\parallel}^2 (\hat{n} - \hat{\phi}) / \hat{\nu} \quad (3.57)$$

$$d_t^{\hat{E} \times B} \hat{\Omega} = \hat{\nabla}_{\parallel}^2 (\hat{n} - \hat{\phi}) / \hat{\nu} \quad . \quad (3.58)$$

This is known as the Hasegawa-Wakatani model [95]. It is often reduced to two spatial dimensions by predefining a fixed parallel wave number  $\hat{k}_{\parallel}$ . Approximating the parallel gradient as

$$\hat{\nabla}_{\parallel}^2 \approx (\rho_s k_{\parallel})^2 = \hat{k}_{\parallel}^2 \quad (3.59)$$

and expanding the nonlinearity in the advective derivative to first order in  $\delta$  results in the system

$$\hat{\partial}_t \hat{n} + \{\hat{n}, \hat{\phi}\} + \hat{\partial}_y \hat{\phi} \hat{k}_n = C(\hat{n} - \hat{\phi}) \quad (3.60)$$

$$\hat{\partial}_t \hat{\Omega} + \{\hat{\Omega}, \hat{\phi}\} = C(\hat{n} - \hat{\phi}) \quad . \quad (3.61)$$

$C$  is the collisionality with  $C = \hat{k}_{\parallel}^2 / \hat{\nu}$ . The Poisson bracket, defined as  $\{f, g\} = \partial_x f \partial_y g - \partial_y f \partial_x g$ , includes the nonlinearities of order  $\delta$ . After linearization of (3.60) and (3.61), the dispersion relation of drift waves reads in physical units

$$\omega(k) = \frac{\omega^* k_y}{1 + \rho_s^2 k_{\perp}^2} - i \frac{\rho_s^3 \nu}{k_{\parallel}^2 L} \frac{k_{\perp}^2 k_y^2}{1 + \rho_s^2 k_{\perp}^2} = \omega_r - i\gamma \quad . \quad (3.62)$$

Drift waves in the Hasegawa-Wakatani model are dispersive (the real part  $\omega_r$ ) and have a linear growth rate (the imaginary part  $\gamma$ ).

### 3.2.4 Nonlinear model: Hasegawa-Mima

In the limit of vanishing collisionality  $C \rightarrow \infty$  the normalized density and potential fluctuations must be equal  $\hat{n} = \hat{\phi}$  to keep the right hand side of (3.57,3.58) finite. In physical quantities this condition is equivalent to the linearized Boltzmann relation

$$\frac{e\tilde{\phi}}{T_e} = \frac{\tilde{n}}{n_c} . \quad (3.63)$$

That means the response of electrons is adiabatic and there is no phase shift between density and potential fluctuations. Subtracting (3.57) and (3.58) yields

$$\hat{\partial}_t(\hat{\nabla}_\perp^2 \hat{\phi} - \hat{\phi}) - \hat{\kappa}_n \hat{\partial}_y \hat{n}_0 + \{\hat{\phi}, \hat{\nabla}_\perp \hat{\phi}\} = 0 . \quad (3.64)$$

This is the Hasegawa-Mima equation for adiabatic electrons [92, 96]. A plane wave ansatz

$$\phi(\vec{r}, t) = \phi_0 e^{i(\vec{k} \cdot \vec{r} - \omega t)} \quad (3.65)$$

and linearization of (3.64) yields the dispersion relation for drift waves

$$\omega = \frac{\omega^*}{1 + \rho_s^2 k_\perp^2} \quad \text{with} \quad \omega^* = \frac{c_s^2}{\omega_{ci}} \kappa_n k_y . \quad (3.66)$$

This solution is identical to the linearized dispersion relation of the Hasegawa-Wakatani model (3.62) with zero growth rate  $\gamma = 0$ . Assuming wave propagation in  $y$ -direction with  $k_x = 0$ , the group and phase velocities of the drift wave are

$$v_{\text{gr}} = \frac{\partial \omega}{\partial k_y} = \frac{c_s^2 \kappa_n}{\omega_{ci}} \frac{1 - \rho_s^2 k_y^2}{1 + \rho_s^2 k_y^2} \quad (3.67)$$

$$v_{\text{ph}} = \frac{\omega}{k_y} = \frac{c_s^2 \kappa_n}{\omega_{ci}} \frac{1}{1 + \rho_s^2 k_y^2} . \quad (3.68)$$

Both velocities are the same in the vanishing  $k_\phi$ -limit and are equal to the electron diamagnetic drift velocity assuming  $\nabla p \perp B_0$

$$k \rightarrow 0 \quad : \quad v_{\text{gr}} = v_{\text{ph}} = \frac{c_s^2 \kappa_n}{\omega_{ci}} = -\frac{k_B T_e}{m_i} \frac{m_i}{eB} \frac{\nabla n_0}{n_0} = -\frac{\nabla p \times \vec{B}_0}{en_0 B^2} = \vec{v}_{\text{dia},e} . \quad (3.69)$$

A plasma potential profile is not considered in the dispersion relation (3.66), a radial potential profile leads to  $\vec{E} \times \vec{B}$  drift. A plasma column, for example, rotates like a rigid body if  $E(r) = \partial \phi / \partial r$  is a linear function. This results in a Doppler shift that must be taken into account when drift wave frequencies are compared with experiments [42]. Additionally small centrifugal forces occur. These forces are

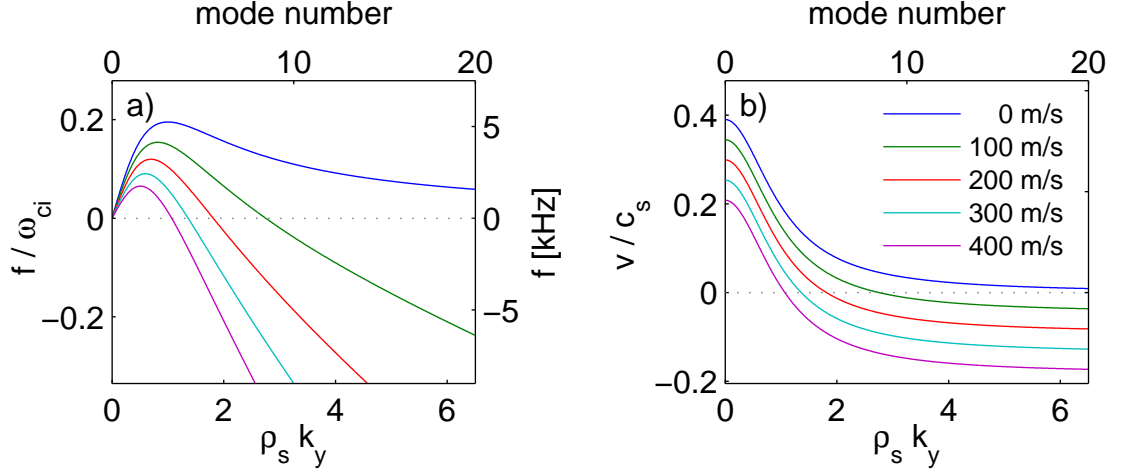


Figure 3.10: Dispersion relation of drift waves obtained with the linearized Hasegawa-Mima model as  $\omega(k)$  in a) and  $v(k)$  in b) with the  $\vec{E} \times \vec{B}$  drift velocity as parameter. Both representations have additional axes, with the wave vector  $k$  expressed as mode number  $m$  and frequency  $f$ . The assumed discharge parameters are  $B_0 = 70$  mT,  $T_e = 2$  eV, and  $\kappa_n = 30 \text{ m}^{-1}$ , resulting in a diamagnetic drift velocity of  $v_{\text{dia}} = 857$  m/s.

taken into account in a numerical simulation of drift waves in VINETA on the basis of an extended Hasegawa-Wakatani model [97](cf. Sec 3.2.3).

In Fig. 3.10, the dispersion relation (3.66) is plotted for a set of typical discharge parameters in VINETA. Doppler shifts due to  $\vec{E} \times \vec{B}$  rotation in the range of  $v_{E \times B} = 0 \dots 400$  m/s are assumed as a parameter. The slope of the dispersion  $\omega(k)$  in Fig. 3.10 (a) in the low  $k$  limit corresponds to a phase velocity of  $v = 0.4 c_s$  for  $v_{E \times B} = 0$ , which is close to the diamagnetic drift velocity  $v_{\text{dia}}$  as expected. The wave frequency starts at zero and reaches its maximum  $f = 0.2 \omega_{ci}$  at  $\rho_s k_y = 1$ . The phase velocity is here  $v = 0.2 c_s$ . For increasing wave number, the phase velocity decreases to  $v = 0.08 c_s$  at  $\rho_s k_y = 2$  and to  $v = 0.01 c_s$  at  $\rho_s k_y = 6$ . If a superimposed  $\vec{E} \times \vec{B}$  drift is considered, the velocity axis is vertically shifted, which corresponds at large  $k$ -values to a more negative slope in the dispersion relation in Fig. 3.10 (a). Hence, in laboratory frame an  $E \times B$  rotation flips the drift wave velocity against the direction of the electron diamagnetic drift velocity for higher mode numbers.

As already described in Sec. 3.2.1, drift waves as instability have a positive growth rate. The dispersion relation (3.66) based on the Hasegawa-Mima model is real valued and does not describe any growth of initially small perturbations. The reason is that adiabatic electrons are assumed in (3.63), which is equivalent to a zero phase shift between potential and density. However, the Hasegawa-Mima model can already be used to study drift wave turbulence, which also develops in this relatively

simple model due to the nonlinearity in the convective derivative. For this purpose, the initial amplitudes must be chosen rather high to be in the nonlinear regime right from the start [98, 99].

# Chapter 4

## Experimental Alfvén wave investigations

### 4.1 Basic properties of Alfvén waves in VINETA

Perturbations of the magnetic field at a certain point in space propagate. Based on wave field measurements the dispersion relation is experimentally recorded and compared with linear Alfvén wave dispersion theory.

#### 4.1.1 Spatial field pattern of Alfvén waves

A fluctuating magnetic field  $b_y(\vec{r}_0, t)$ , generated in the plasma centre  $\vec{r}_0 = 0$ , induces currents flowing along and across the ambient magnetic field  $B_0$ . The magnetic fluctuation propagates and forms a wave field with a complex spatial structure. Depending on the induced currents, all magnetic field components  $b_x(\vec{r}, t)$ ,  $b_y(\vec{r}, t)$ , and  $b_z(\vec{r}, t)$  are influenced. The investigations of the wave field pattern are done in an argon discharge with a magnetic field of  $B_0 = 102 \text{ mT}$ , which yields an ion-cyclotron frequency of  $f_{ci} = 39.2 \text{ kHz}$ . The excitation antenna is operated at  $f = 30 \text{ kHz}$  with an amplitude of  $|b_y| = 78 \mu\text{T}$ . The  $\dot{B}$ -detector (cf. Sec. 2.2) is used to measure the three orthogonal magnetic fluctuation components in the radial-axial plane covering  $x = -70 \dots 70 \text{ mm}$  in radial and  $z = 0 \dots 2000 \text{ mm}$  in axial direction. The excitation antenna is located outside the recording range at  $z = -100 \text{ mm}$  to avoid near field effects from the antenna.

The measurements are done by scanning the spatial plane in consecutive discharges. The exciter antenna is operated for several hundred wave periods and time series of

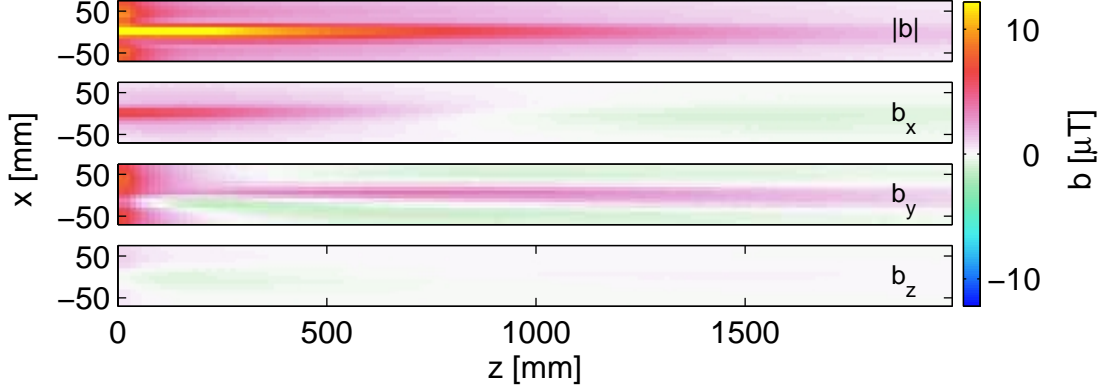


Figure 4.1: Fluctuating magnetic field of an AW in the radial-axial ( $x, z$ )-plane, excited at  $z = -100$  mm with  $\omega/\omega_{ci} = 0.77$  in an argon plasma. The three magnetic components are shown for a fixed time  $t_0$ ; the absolute value  $|\vec{b}|$  is time-averaged.

$b_x(t)$ ,  $b_y(t)$  and  $b_z(t)$  are recorded. As described in Sec. 2.6, only the complex Fourier components at the excitation frequency  $\omega_0$  are considered in the data evaluation to separate the wave field from noise-like fluctuations. The absolutely calibrated data is shown in Fig. 4.1 for a single time instant  $t_0$ . The three components  $b_x$ ,  $b_y$  and  $b_z$  and the time-averaged modulus of the magnetic fluctuation amplitude  $|\vec{b}|$  are shown.  $|\vec{b}|$  is localized over the full observed axial range to a radial extent of  $r = \pm 10$  mm. It decreases from  $13.7 \mu\text{T}$  at  $z = 0$  mm to  $1.36 \mu\text{T}$  at  $z = 2000$  mm, which is equivalent to a damping length  $d = \Delta z / \ln(b_1/b_2) \approx 1$  m. At small distance from the exciter antenna, significant amplitudes of up to  $9 \mu\text{T}$  are observed that extend radially up to  $r = \pm 60$  mm. They are attributed to a superposition of the wave field with the near field of the exciter antenna, which has an extent of a few centimeters. This near field region of the antenna will not further considered. Far away from the antenna, the wave propagates along  $B_0$  in a tube with a diameter similar to the size of the excitation antenna, assuming rotational symmetry. The magnetic fluctuation of the wave is mainly perpendicular to  $B_0$ , owing to strong parallel currents. Currents perpendicular to  $B_0$  would cause parallel magnetic field fluctuations which are found to be much weaker than the perpendicular ones. All currents, parallel as well as perpendicular, are resistively damped by collisions. This leads to a decay of the wave fields with increased propagation distance, as observed e.g. for  $|\vec{b}|$  in Fig. 4.1.

The snapshot of the three magnetic field components in Fig. 4.1 reveals useful information about the spatial dynamics of the wave. In parallel direction, the components  $b_x$  and  $b_y$  show a wave type behavior.  $b_y$  has a maximum of  $2.8 \mu\text{T}$  at  $z = 920$  mm and decays to  $1.1 \mu\text{T}$  at  $z = 2000$  mm.  $b_x$  is  $90^\circ$  out of phase, starts with a positive

value at small  $z$ -values, has a zero passage around  $z = 870$  mm, and reaches a negative value of  $-0.7 \mu\text{T}$  at  $z = 2000$  mm. So the measurement distance of 1200 mm corresponds to a phase shift somewhat smaller than  $\lambda/4$ , corresponding to a wave length of  $\lambda > 5$  m. Besides this distinct structure in  $z$ -direction, both components decrease in radial  $x$ -direction towards the plasma boundary. This is simply due to the peaked density profile (cf. Fig. 2.13), i.e. the wave is supported only in the plasma center.

### 4.1.2 Propagation parallel to the magnetic field

Since the magnetic wave field is localized to the plasma center, the investigation of wave propagation can be limited to the  $z$ -axis at  $x = 0$ . The axial coordinate  $z$  is chosen to be greater than 200 mm to avoid exciter near-field effects. The lowest possible spatial resolution is  $\Delta z = \lambda/2 = 2.5$  m due to the Nyquist-limit. To detect smaller wave lengths, a grid distance of  $\Delta z = 0.3$  m is chosen. This ensures correct wave detection without aliasing down to  $\lambda = 0.6$  m. Six time series are recorded at six different  $z$ -positions in an argon discharge with the same parameters as for the previous radial-axial scan experiment. The obtained wave field  $b_y(t, z)$  is shown in Fig. 4.2 (a) with the time on the abscissa and the  $z$ -coordinate on the ordinate. The color-coded amplitude of the magnetic field component  $b_y$  shows the typical tilted stripe pattern of a propagating wave. The slope of these stripes is a measure for the phase velocity of the wave. The decrease of the amplitude in  $z$ -direction is due to damping. In Fig. 4.2 (a), the amplitude decreases from  $7 \mu\text{T}$  to  $1 \mu\text{T}$  over the covered  $z$ -range, which is nearly the same damping length as in the previous result (Fig. 4.1).

A plane wave can be written in the form

$$b_y(t, z) = b_{y0} e^{-z/d} e^{i(kz - \omega_0 t)} , \quad (4.1)$$

with the two parameters damping length  $d$  and the parallel wave number  $k$ . They are extracted from the measurement  $b_y(t, z)$  via Fourier transform [100, p.35]

$$b_y(\omega_0, z) = \int_{-\infty}^{\infty} b_{y0} e^{-z/d} e^{i(kz - \omega_0 t)} e^{-i\omega t} dt = b_{y0} e^{-z/d} e^{ikz} \begin{cases} 0 & \omega \neq -\omega_0 \\ 1 & \omega = -\omega_0 \end{cases} . \quad (4.2)$$

Fourier coefficients are complex-conjugated for negative and positive frequencies and the  $z$ -dependence of  $b_y$  is

$$|b_y(\omega, z)| = b_{y0} e^{-z/d(\omega)} \quad \phi_{by}(\omega, z) = -k(\omega)z , \quad (4.3)$$

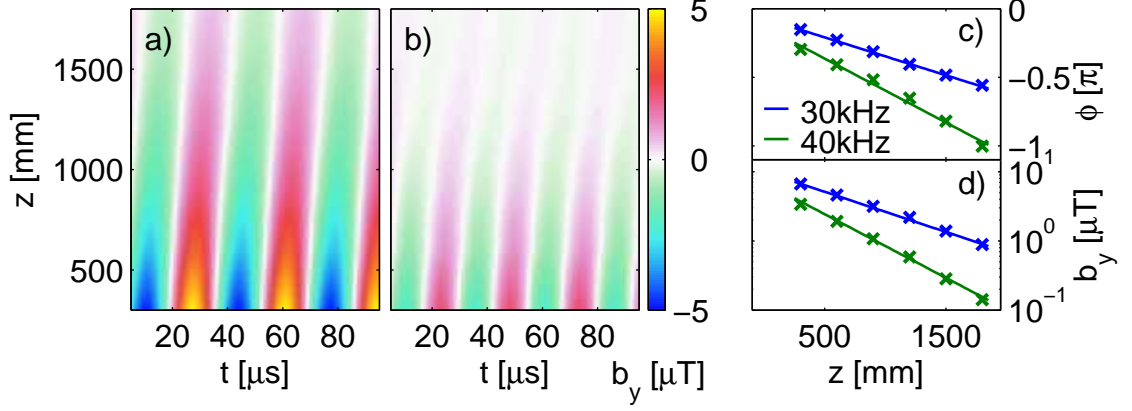


Figure 4.2: Magnetic component  $b_y$  (interpolated) of an AW excited at  $z = -100 \text{ mm}$  in an argon discharge with  $f_{ci} = 39.2 \text{ kHz}$  for  $f = 30 \text{ kHz}$  (a) and  $f = 40 \text{ kHz}$  (b). Axial development of the phase  $\phi$  (c, linear) and of the amplitude  $b_y$  (d, semilogarithmic).

with  $|b_y|$  and  $\phi_{by}$  as amplitude and phase of the complex-valued  $b_y$ . The extracted amplitudes and phases are shown in Fig. 4.2 (c) and Fig. 4.2 (d), respectively. These diagrams show that both the linear dependence for  $\phi(z) = -kz$  and the exponential decay for  $|b_y|$  are well satisfied. The two parameters  $d$  and  $k$  can be extracted from a best fit. Their values for the frequency  $f = 30 \text{ kHz} = 0.77f_{ci}$  are  $\lambda = 2\pi/k = 7.44 \text{ m} \pm 0.13 \text{ m}$  and  $d = 0.82 \text{ m} \pm 0.02 \text{ m}$ , which is in good agreement with the estimates made from the radial-axial scan (Fig. 4.1).

In the same discharge and at the same  $z$ -positions, time series were recorded for a higher excitation frequency of  $f = 40 \text{ kHz} = 1.02f_{ci}$ , very close to the ion-cyclotron frequency. The amplitude of the initial  $b_y$ -perturbation at the excitation antenna is here  $24.8 \mu\text{T}$ . The color-coded amplitude of the magnetic field component  $b_y(t, z)$  is shown in Fig. 4.2 (b). The pattern indicates a propagating wave, too, although the initial amplitude is smaller due to smaller excitation amplitudes. The main difference to the  $f = 30 \text{ kHz}$  case is the reduced velocity, characterized by smaller slope in the propagation pattern. Increased damping is also observed. Both findings can be verified in the Fourier representation Fig. 4.2 (c) and (d). Note that in the  $f = 40 \text{ kHz}$  case the phase fronts are not perfectly straight as assumed for the plane wave ansatz (4.3)

### 4.1.3 Alfvén wave dispersion relation

In the argon discharge described above the wave number  $k$  and the damping length  $d$  are measured for the frequency range  $5 \text{ kHz} \dots 60 \text{ kHz}$ . All three components  $b_x(\omega)$ ,

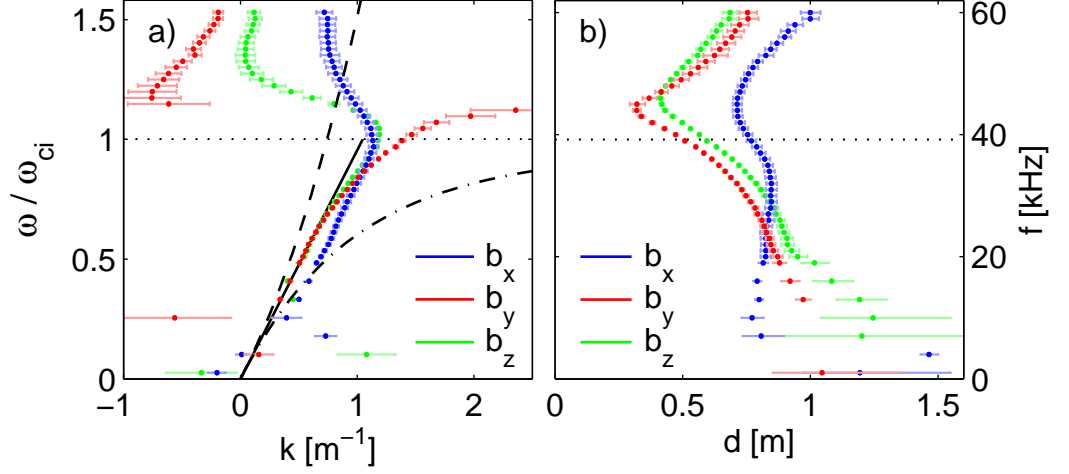


Figure 4.3: Dispersion relation  $\omega(k)$  of the wave measured in argon plasma for  $b_x$  (blue),  $b_y$  (red) and  $b_z$  (green). The real part  $\omega(k)$  is shown in (a) and the imaginary part is expressed as damping length  $d(\omega) = 1/k_i(\omega)$  in (b). For the real part, the dispersion of AWs is included in low-frequency approximation  $\omega \ll \omega_{ci}$  (black), as Hall-MHD description for shear AW (dash-dotted) and as Hall-MHD description for fast AW (dashed).

$b_y(\omega)$ , and  $b_z(\omega)$  are measured. The dispersion relation  $k(\omega)$  is the finger print of the wave type excited. It is complex  $k(\omega) = k_r(\omega) + ik_i(\omega)$ , where the imaginary part relates to the damping length as

$$d = 1/k_i . \quad (4.4)$$

Both real and imaginary part are shown in Fig. 4.3 (a) and (b), respectively. All three magnetic field components have an almost linear dispersion for frequencies around  $\omega_{ci}/2$ , a nonlinear characteristic around  $\omega_{ci}$ , and a random behavior at low frequencies. For  $b_y$  and  $b_z$  the phase and the group velocity match with  $v = 2.35 \cdot 10^5 \text{ m/s}$ . The measured phase velocity decreases for increasing frequencies. At  $\omega > \omega_{ci}$  the wave number has a roll-over point. The negative  $k$ -values correspond to backward propagation. The damping of  $b_y$  and  $b_z$  increases with increasing frequency up to the roll-over point where the trend changes and damping becomes smaller. The dispersion behavior of  $b_x(\omega)$  differs significantly. Well below  $\omega_{ci}$  the dispersion is linear as well but phase and group velocities differ. The roll-over point is located exactly at  $\omega_{ci}$ . The damping of the  $b_x$  component decreases slightly up to approximately  $0.75\omega_{ci}$ , different from  $b_y$  and  $b_z$ .

Some features of the measured dispersion relation indicate the excitation of AWs. The low-frequency range with the randomly distributed  $k$  values is most likely due to the presence of drift waves [42] and is therefore excluded from discussion. For low

frequencies AWs involve only perpendicular magnetic fields [64]. This is consistent with the measured  $b_z$  amplitudes, which are one order of magnitude smaller than the amplitudes of  $b_x$  and  $b_y$  (cf. Fig. 4.1). However, the dispersions of  $b_x$  and  $b_y$  differ significantly from each other. Since there is no preferential direction for AW fields this difference must be caused by the excitation scheme which excites mainly the  $b_y$  component. The basic AW dispersion properties are therefore evaluated taking the  $b_y$  data.

In the low-frequency range, below  $\omega_{ci}/2$ , the phase- and group velocity is  $v = 2.35 \cdot 10^5$  m/s. Taking this as the Alfvén velocity we obtain with the used ambient magnetic field  $B_0 = 102$  mT a mean plasma density  $\bar{n} = 3.5 \cdot 10^{18}$  m $^{-3}$ . This is averaged over the extent of the wave propagation and agrees quite well with the peak plasma density of  $n_e = 4.1 \cdot 10^{18}$  m $^{-3}$  measured with the interferometer and Langmuir probes. In the higher frequency range  $> \omega_{ci}/2$ , no satisfactory agreement with theoretically expected dispersion relations is found, neither with shear AWs nor with fast AWs. Measured  $k$  values are somewhat in-between both dispersion relations and above  $\omega_{ci}$  the values for the different magnetic field components differ significantly from each other. A sharp resonance at  $\omega_{ci}$ , as expected for shear AWs is never observed.

All measured dispersion relations have a pronounced roll-over point. They have an ambiguous relation to the resonance point at  $\omega_{ci}$  since they vary slightly in their frequencies. The roll-over points are always larger in frequency than  $\omega_{ci}$ , which is contrary to the trend to shift the resonance to lower frequencies when collisions with neutral atoms are taken into account [101]. The wave excited in the frequency range around  $\omega_{ci}$  is subject of a more detailed analysis in Sec. 4.3.

#### 4.1.4 Influence of $B_0$ on phase velocity

To investigate the influence of  $B_0$  on the phase velocity of the wave, two dispersion relations are recorded: one at the maximum field strength  $B_0 = 102$  mT and one at  $B_0 = 77$  mT. Without any doubt it would have been desirable to vary  $B_0$  at more than these two levels. However the immense experimental effort of recording one single dispersion relation lead to this very limited number of parameter levels. The two dispersion relations are shown in Fig. 4.4. As already discussed in Sec. 4.1.3 they have similar features, which correspond to the linear scaling of  $v_A$  with  $B_0$ . The expected and the measured phase velocities are compiled in Tab. 4.1.

Reducing  $B_0$  to 75 % of the initial value and taking into account the density decrease results in a decrease of  $v_A$  to 79 %. The measured velocity is reduced to 72 % of the initial value. This is a reasonable agreement between  $v_A$  and  $v_{\text{meas}}$ , where

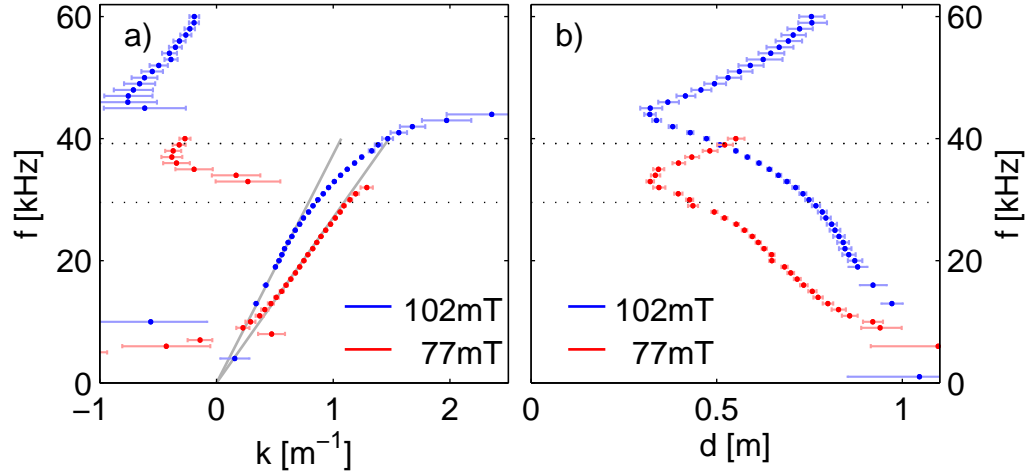


Figure 4.4: Dispersion (a) and damping (b) of AWs in an Argon plasma for two values of ambient magnetic field ( $B_0 = 102 \text{ mT}$ , red curve and  $B_0 = 77 \text{ mT}$ , blue curve). The corresponding ion-cyclotron frequencies  $f_{ci} = 39.2 \text{ kHz}$  and  $f_{ci} = 29.6 \text{ kHz}$  are included as dashed lines.

$B_0$ [mT]	$n$ [ $\text{m}^{-3}$ ]	$v_A$ [m/s]	$v_{\text{meas}}$ [m/s]
102	$4.07 \cdot 10^{18}$	$1.75 \cdot 10^5$	$2.35 \cdot 10^5$
77	$3.71 \cdot 10^{18}$	$1.38 \cdot 10^5$	$1.70 \cdot 10^5$

Table 4.1: Phase velocities of the excited waves for different ambient magnetic fields in an Argon plasma.

the uncertainty is mainly in the density measurement (about 10 %). The absolute difference of the velocities is accounted to the density profile, which is not considered in the definition of  $v_A$  in (3.8).

#### 4.1.5 Influence of $n_e$ on phase velocity

To study the influence of the density on the phase velocity of the wave, two dispersion relations were recorded in Argon plasmas at different rf-input power. The resulting plasma densities differ by a factor 24. The dispersion and damping curves are shown in Fig. 4.5. They show the same qualitative properties as discussed in the case of  $B_0$  variation. The derived measurement results are compiled in Tab. 4.2.

The Alfvén velocity scales with the inverse square root of the plasma density, so the phase velocity is expected to change by a factor  $\sqrt{24} = 4.9$ . The observed change by 4.5 is in good agreement with the expectation.

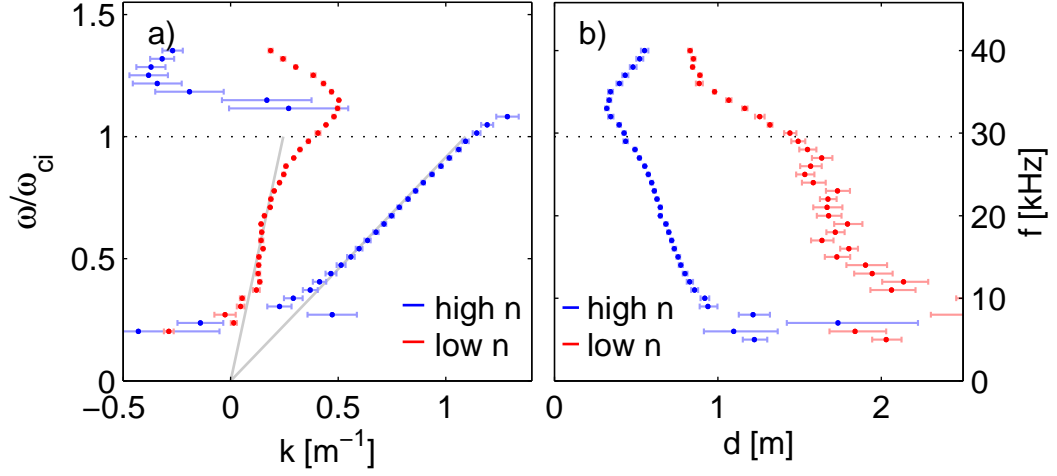


Figure 4.5: Dispersion (a) and damping (b) of AWs in an Argon plasma for two different plasma peak densities  $n = 4.1 \cdot 10^{19} \text{ m}^{-3}$  and  $n = 3.7 \cdot 10^{18} \text{ m}^{-3}$ .

$B_0$ [mT]	$n$ [ $\text{m}^{-3}$ ]	$v_A$ [m/s]	$v_{\text{meas}}$ [m/s]
77	$3.71 \cdot 10^{18}$	$1.38 \cdot 10^5$	$1.70 \cdot 10^5$
77	$1.55 \cdot 10^{17}$	$6.77 \cdot 10^5$	$7.60 \cdot 10^5$

Table 4.2: Phase velocities of the excited waves for different plasma densities in an Argon plasma.

#### 4.1.6 Influence of ion mass on phase velocity

The working gas has an influence on  $v_A$  via the ion mass density. Three different gases, Argon, Helium, and Hydrogen are used. Since the helicon discharge is sensitive to the working gas, a density variation is unavoidable. For Hydrogen, a discharge could only be operated for a gas mixture with 55 % helium, but a helicon discharge mode could not be established. The radial plasma density profile is hollow and not any more peaked. As for the other cases with helicon discharge, the peak plasma density is used to determine the Alfvén velocity. The result of the measurement is shown in Fig. 4.6.

The dispersion relation for Argon plasma is already discussed above. The dispersion relation in Helium plasma is similar to that in Argon plasma with a different frequency scale. A frequency range of constant phase velocity and a roll-over point at about 200 kHz are found, which is below the ion-cyclotron frequency  $\omega_{ci}/2\pi$ . This was previously observed in the same device [25]. From the linear range, the low-frequency phase velocity of the wave is determined. The situation is more difficult

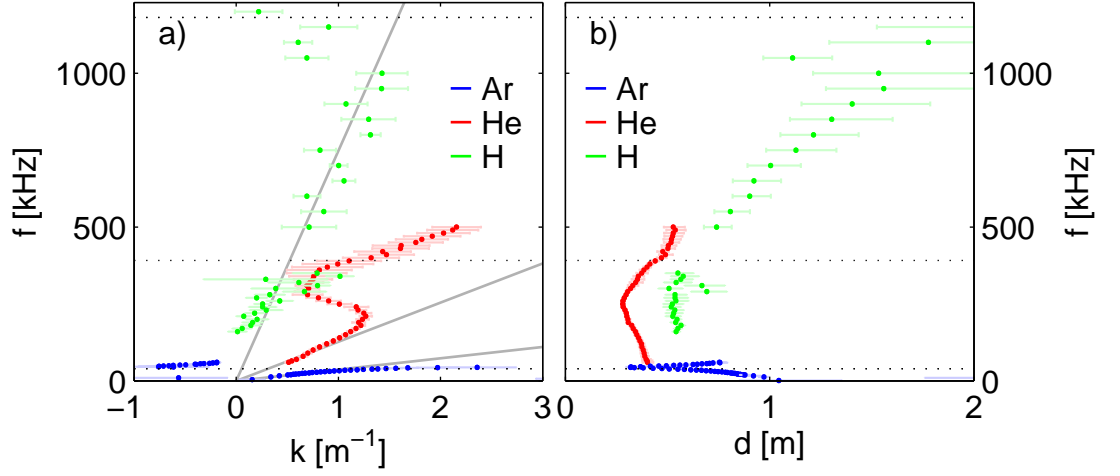


Figure 4.6: Dispersion (a) and damping (b) of AWs in plasmas of different gases: blue — argon discharge, red — helium discharge, green — discharge in mixture of 45 % hydrogen and 55 % helium. The ion-cyclotron resonance frequencies for each gas (39.2 kHz, 392 kHz, 1.18 MHz) are included as dashed lines.

$B_0$ [mT]	gas	$n$ [m <sup>-3</sup> ]	$v_A$ [m/s]	$v_{\text{meas}}$ [m/s]
102	argon	$4.07 \cdot 10^{18}$	$1.75 \cdot 10^5$	$2.35 \cdot 10^5$
102	helium	$4.12 \cdot 10^{18}$	$5.50 \cdot 10^5$	$8.00 \cdot 10^5$
77	45 % H / 55 % He	$4.35 \cdot 10^{17}$	$2.60 \cdot 10^6$	$4.70 \cdot 10^6$

Table 4.3: Wave velocities for different working gases

to interpret for Hydrogen plasma because waves are excited in a gas mixture [102]. At low frequencies, there is no range of equal phase and group velocity. A linear run of the dispersion relation is observed for frequencies exceeding 500 kHz. A significant influence of Helium in the dispersion relation up to  $f_{ci}^{\text{He}} = 392$  kHz is expected and above this frequency, the presence of Helium ions will also influence the wave propagation. The measured plasma density and the phase velocity for different ion species and different  $B_0$  are compiled in Tab. 4.3.

The expected ratio of phase velocities in Argon and Helium is 1 : 3.14, which agrees well with the measured ratio of 1 : 3.40. A wave with 14.6 times higher phase velocity is expected for Hydrogen. The measured velocity ratio is 20.0. The error of 25 % is consistent with the large error bars of the wave number determination in the Hydrogen/Helium plasma. One reason is the increased signal-to-noise ratio of the excitation-detection system at the high frequencies around 1 MHz as discussed in Sec. 2.5.

## 4.2 Currents of Alfvén waves

The experimentally obtained dispersion relations reasonably agree with the expected dispersion behavior of AWs in the low frequency limit. For frequencies close to the ion-cyclotron resonance  $\omega_{ci}$ , the run of the measured dispersion curves is in-between the branches for shear AWs and fast AWs. A resonance  $\omega_{ci}$  is not observed. A possible explanation is a superposition of shear AWs and fast AWs. It is possible to distinguish both by the different rotation directions of their field and current patterns.

### 4.2.1 Currents parallel and perpendicular to $B_0$

Far away from the excitation antenna the fluctuating magnetic fields are solely generated by the wave currents. Fig. 4.7 shows the fluctuation amplitude of the three magnetic components  $b_x$ ,  $b_y$  and  $b_z$  at a distance  $\Delta z = 1900$  mm from the antenna. To exclude any effects from the excitation system the shown amplitudes are corrected for the frequency response of the excitation system, a nominal excitation amplitude of  $b_{exc} = 100 \mu\text{T}$  is assumed. As already found for low frequencies  $\omega \leq 0.75 \omega_{ci}$ , the perpendicular components ( $b_x$ ,  $b_y$ ) have similar magnitudes and the parallel one ( $b_z$ ) is one order of magnitude smaller. The amplitudes of all three components increase with frequency in the low frequency range. If  $\omega_{ci}$  is approached, the three magnetic field components behave differently: While  $b_y$  and  $b_z$  are decreasing until a minimum is reached at 43 kHz and 46 kHz, respectively, the component  $b_x$  has no pronounced

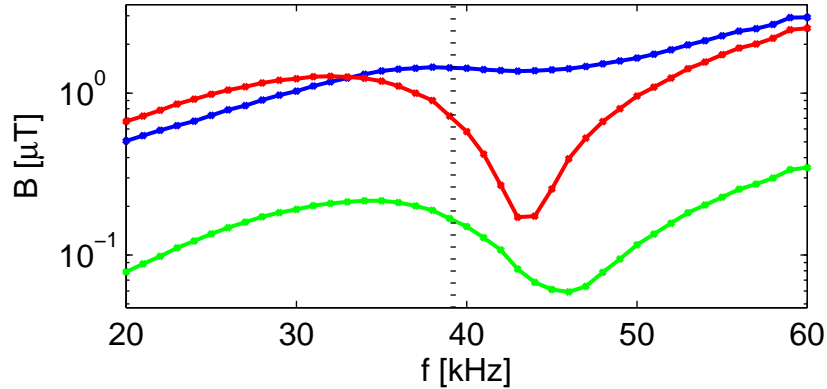


Figure 4.7: Fluctuating magnetic field of AW in an Argon plasma,  $\Delta z = 1900$  mm away from the antenna. Absolute amplitudes for  $b_x$  (blue),  $b_y$  (red) and  $b_z$  (green) are corrected for the frequency response of the excitation system with a nominal excitation amplitude of  $100 \mu\text{T}$ . Included as dashed line is the ion-cyclotron frequency of  $f_{ci} = 39.2$  kHz.

minimum. Such a different behavior of the magnetic field components was already found in the discussion of the measured dispersion curves.

Currents and magnetic field, possibly fluctuating in time and space, are connected via Ampère's law

$$\mu_0 \vec{j} = \vec{\nabla} \times \vec{b} . \quad (4.5)$$

$\vec{\nabla} \times \vec{b}$  are spatial derivatives of the magnetic field components that are not directly available from the measurement. If outside the plasma vanishing  $b$ -fluctuations are assumed, the measured magnetic field components must have spatial gradients. In this way, the existence of currents can be concluded.  $\vec{b}(\omega)$  increases about equally with frequency for  $\omega \leq 0.75\omega_{ci}$  in all components. This makes it possible to separate the magnetic field as  $\vec{b}(\omega) = f(\omega)\vec{b}_0$  with a fixed  $\vec{b}_0$  and a unique function  $f(\omega)$ . Inserting this into (4.5) yields a monotonically increasing current density of the form  $j = f(\omega)j_0$ . The reason for that is the increasing plasma current induced by the exciter antenna with increasing frequency. Due to Faraday's law (cf. Eq. A.4) the induced electric potential for an excitation at  $\omega$  is

$$U_{\text{ind}} = -b_{\text{exc}}\omega \cos \omega t . \quad (4.6)$$

If the resistivity of the plasma is assumed to be constant, the magnitude of the induced currents is proportional to  $\omega$ . This dependence is fully attributed to the excitation and is not a wave property. The frequency dependence of  $\vec{b}$  around  $\omega_{ci}$ , however, actually reflects the dynamics of the wave.

In Sec. 3.1 the dispersion relation for shear AWs was derived [cf. Eq. (3.20)]. It can be written in the form

$$k_z^2 v_A^2 = \frac{\omega^2}{1 - \omega/\omega_{ci}} = \frac{1}{1/\omega^2 - 1/\omega\omega_{ci}} . \quad (4.7)$$

The parallel wave number is a function of the frequency  $k_z = k_z(\omega)$ , the perpendicular ones are not  $k_x \neq k_x(\omega), k_y \neq k_y(\omega)$ . The partial derivatives of the rotation in (4.5) can be explicitly obtained from the plane wave ansatz (3.4), the frequency dependence enters via the dispersion relation (4.7)

$$\begin{aligned} \partial b_x / \partial y &= k_y & i b_{x0} e^{i(\vec{k}\vec{r} - \omega t)} \\ \partial b_y / \partial x &= k_x & i b_{y0} e^{i(\vec{k}\vec{r} - \omega t)} \\ \partial b_x / \partial z &= k_z(\omega) & i b_{x0} e^{i(\vec{k}\vec{r} - \omega t)} \\ \partial b_y / \partial z &= k_z(\omega) & i b_{y0} e^{i(\vec{k}\vec{r} - \omega t)} \end{aligned} . \quad (4.8)$$

Here a wave excitation in the coordinate origin with only perpendicular fluctuating field components  $b_{z0} = 0$  is assumed. For small propagation angles  $\angle(\vec{k}, \vec{B}_0) \ll 1$  the

perpendicular wave numbers  $k_x$  and  $k_y$  are small, resulting in small perpendicular derivatives in (4.8). The parallel wave number is large for frequencies approaching the ion-cyclotron frequency, since  $\lim_{\omega \rightarrow \omega_{ci}} k_z = \infty$  in (4.8). This results in large parallel derivatives in (4.8). The parallel current density  $j_z$  is obtained in Ampère's law (4.5) from the difference of perpendicular derivatives, so it has a finite value around  $\omega_{ci}$ . In contrast the perpendicular components  $j_x$  and  $j_y$  diverge around  $\omega_{ci}$  due to the diverging parallel derivatives  $\partial b_x / \partial z$  and  $\partial b_y / \partial z$ . Hence, close to the ion cyclotron resonance smaller parallel currents combine with large perpendicular currents to a 3-dimensional current pattern. The perpendicular current components are derived in explicit form with (3.6)

$$j_x = -\frac{i\omega E_x}{\mu_0 v_A^2} \equiv \frac{nm_i}{B_0^2} \dot{E}_x(t) \quad j_y = -\frac{i\omega E_y}{\mu_0 v_A^2} \equiv \frac{nm_i}{B_0^2} \dot{E}_y(t) . \quad (4.9)$$

The perpendicular currents are proportional to the time derivatives of the respective components of the electric field and to the mass density. They are inversely proportional to the square of the ambient magnetic field. This is exactly the definition of the ion polarization current.

### 4.2.2 Idealization: parallel current filaments

In the experiment, the parallel currents are found to be localized in distinct regions of the azimuthal plane (cf. Sec. 4.3), as already reported in previous studies [19]. To develop a physical picture of the self-consistent current system of shear AWs, the parallel currents are described in this section as current filaments with small extent perpendicular to  $B_0$ . The perpendicular currents will be considered as result of the parallel currents in a second step.

The exciter used in the experiment draws a parallel current of  $I_{\text{fil}} \approx 10 \text{ mA}$  at a frequency of  $f = f_{ci}/2 = 20 \text{ kHz} \approx \omega_{ci}/2$  in an argon discharge (cf. Sec. 4.3). The displacement current in Ampère's law (cf. Eq. A.3) can be neglected at those low frequencies. In this case the Biot-Savart law holds, it is used to calculate the magnetic field of the current filament. A filament with infinite extent in  $z$ -direction is assumed instead of the finite parallel wave length  $\lambda_z$ . This approximation holds well for small perpendicular distances  $\vec{r}_\perp \ll \lambda_z$ .

$$\vec{b}(\vec{r}) = I_{\text{fil}} \frac{\mu_0}{2\pi} \frac{1}{x^2 + y^2} \begin{pmatrix} y \\ -x \end{pmatrix} \quad \text{with} \quad \vec{r} = \begin{pmatrix} x \\ y \end{pmatrix} . \quad (4.10)$$

The AW's dynamic electric field is derived analytically using (3.9)

$$\vec{E}_\perp(\vec{r}) = v_A \sqrt{1-f} \begin{pmatrix} b_y \\ -b_x \end{pmatrix} \quad (4.11)$$

$$= -I_{\text{fil}} v_A \sqrt{1-f} \frac{\mu_0}{2\pi} \frac{1}{x^2 + y^2} \begin{pmatrix} x \\ y \end{pmatrix} . \quad (4.12)$$

The ratio  $\omega/k_z$  in (3.9) has been replaced by the dispersion relation of shear AWs from (3.20) considering the normalization  $f = \omega/\omega_{ci}$  introduced in (3.11).  $\vec{E}_\perp$  and  $\vec{b}$  are plotted in Fig. 4.8. As expected for electromagnetic waves,  $\vec{E}_\perp$  and  $\vec{b}$  are oriented perpendicular to each other at all positions. Both fields decrease with distance to the filament as  $\sim 1/r$ . The only source for the shown fields is the initially assumed parallel current filament. Contributions from perpendicular currents are neglected. The ion polarization current in response to temporal changes of  $\vec{E}_\perp$  is obtained

$$j_{\text{pol}} = \frac{nm_i}{B_0^2} \frac{d\vec{E}_\perp(t)}{dt} = \frac{nm_i}{B_0^2} \left( \vec{v} \vec{\nabla} + \frac{\partial}{\partial t} \right) \vec{E} . \quad (4.13)$$

A change in  $\vec{E}_\perp$  is either due to an explicit time dependence of  $\vec{E}_\perp(t)$  or to a moving fluid element, accounted for by the convective derivative in (4.13) ( $v$  is the perpendicular filament velocity). Both the explicit and the convective part will be discussed in the following two sections.

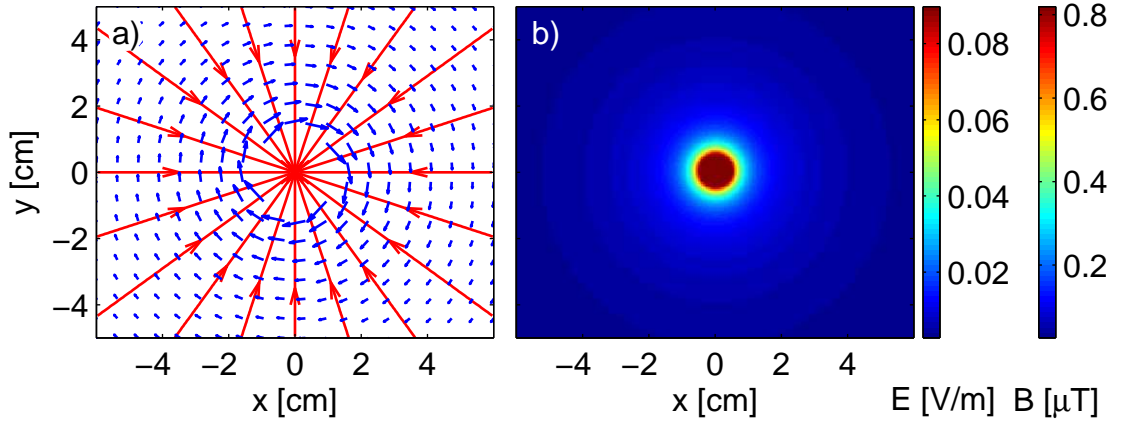


Figure 4.8: Electric and magnetic field of an AW current filament for a current of  $I_{\text{fil}} = 10 \text{ mA}$  at  $\omega = \omega_{ci}/2$ . The direction of the current is out of the plane. The vector field representation (a) includes the magnetic field (blue) and the dynamic electric field (red). Their absolute values shown in (b) differ only by a factor.

### 4.2.3 Explicit time dependence of the current

The current filament is first assumed to be fixed in space at the position  $(x_0, y_0)$  in the azimuthal plane and its amplitude varies sinusoidally  $I_{\text{fil}} = I_{\text{fil}}(t)$ . The time

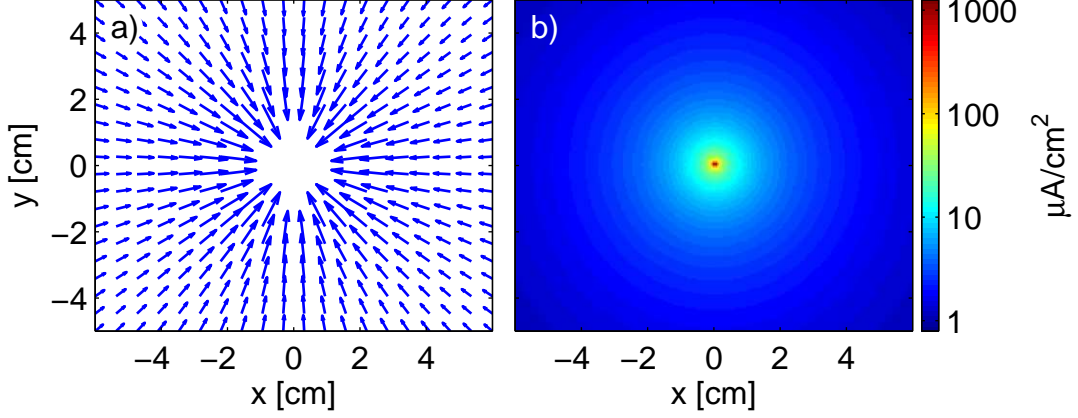


Figure 4.9: Ion polarization current  $\sim \partial E_{\perp} / \partial t$  of a parallel current filament, located at the fixed position  $x = 0$  mm,  $y = 0$  mm. The vector field representation (a) is complemented by the absolute value of  $|j_{\text{pol}}|$  in (b).

dependence of the electrical field is then explicit and the polarization current reads

$$\vec{j}_{\text{pol}} = -\frac{\partial I_{\text{fl}}}{\partial t} \frac{\sqrt{1-\Omega}}{2\pi v_A} \frac{1}{x^2 + y^2} \begin{pmatrix} x \\ y \end{pmatrix}. \quad (4.14)$$

A graphical representation is given in Fig. 4.9. The spatial structure of the currents is obviously the same as for the electric field (cf. Eq. 4.12). The absolute value of the current at a radial distance of 1 cm from the filament is  $8.77 \mu\text{A}/\text{cm}^2$ . Due to the derivative in (4.14), a temporal phase shift of  $\pi/2$  is introduced between the perpendicular currents and the parallel ones. With a plane wave ansatz  $j_{\parallel} \sim \exp(kz - \omega t)$ , the polarization current is phase shifted by  $\lambda/4$  in  $z$ -direction.

A schematic 3-dimensional picture of the currents of a certain time instant is shown in Fig. 4.10. The parallel currents change their amplitude and sign within the wave length  $\lambda$ . The perpendicular polarization currents lead to quasineutrality. For the AW considered here, the total polarization current summed over a half wave length is

$$I_{\text{pol}} = \int_0^{\lambda/2} A_o j_{\text{pol}} \sin(kz) dz = 2\pi r_0 (\lambda/2) j_{\text{pol}} (2/\pi) = 10.0 \text{ mA} \quad , \quad (4.15)$$

using (4.14) with  $f = 1/2$  and  $\lambda = 5.70$  m

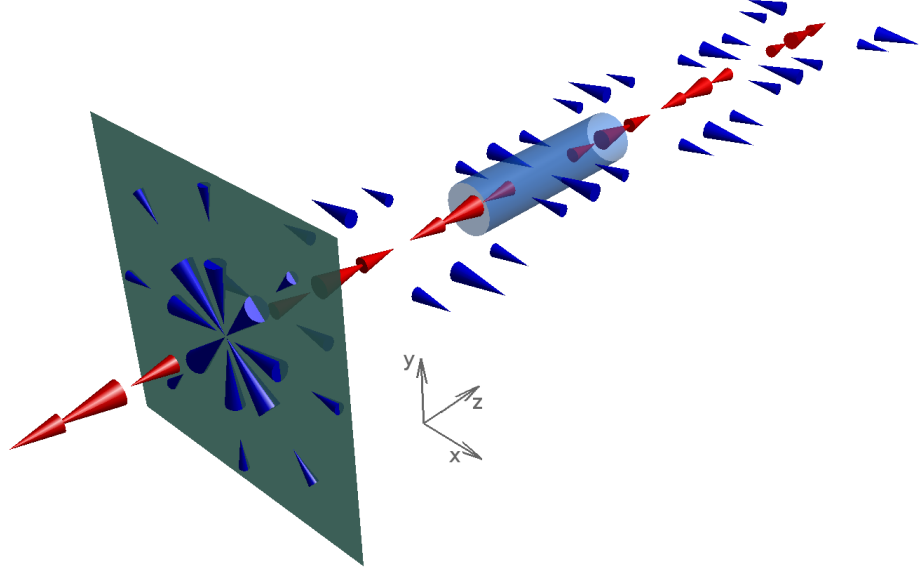


Figure 4.10: Schematic view of an AW with one parallel current filament  $j_{\parallel}(z, t)$  (red) at fixed coordinates  $(x_0, y_0)$  in the azimuthal plane. Perpendicular polarization currents (blue) are central symmetric as shown in the depicted plane, cf. also Fig. 4.9.

#### 4.2.4 Convective derivative for a moving current filament

If the current filament is not fixed in space but moves perpendicular to  $B_0$ , the convective derivative must be taken into account. In the numerically evaluated MHD-solution for AWs the involved field rotate like a rigid body (cf. Fig. 3.6). The parallel currents are concentrated in distinct regions in planes perpendicular to the propagation direction, which allows one to idealize them as current filaments. Without loss of generality, the velocity  $v$  of the current filament is chosen to be in  $y$ -direction. For an electric field pattern of the form  $\vec{E}_{\perp} = (E_0/r^2)\vec{r}$ , the convective derivative yields

$$(\vec{v} \cdot \vec{\nabla})\vec{E}_{\perp} = v_y E_0 \left( \frac{\partial E_x / \partial y}{\partial E_y / \partial y} \right) = \frac{v_y E_0}{(x^2 + y^2)^2} \begin{pmatrix} -2xy \\ x^2 - y^2 \end{pmatrix}. \quad (4.16)$$

Replacing  $E_{\perp}$  with (4.12) results in a polarization current of

$$\vec{j}_{\text{pol}} = -I_{\text{fil}} \frac{\sqrt{1-f}}{v_A} \frac{\mu_0}{2\pi} \frac{v_y}{(x^2 + y^2)^2} \begin{pmatrix} -2xy \\ x^2 - y^2 \end{pmatrix}. \quad (4.17)$$

For an estimate of the amplitude of the polarization current, a velocity value has to be assumed. In experiment rotating field patterns are measured with an off-axis displacement of the maximum current of approximately 2 cm (cf. Sec. 4.3). Assuming

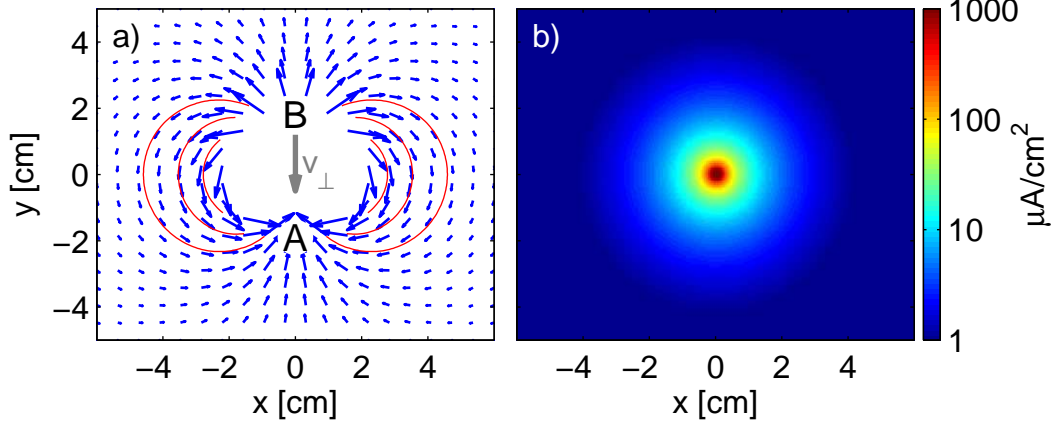


Figure 4.11: Convective part  $\sim (\vec{v} \cdot \vec{\nabla}) \vec{E}_{\perp}$  of the polarization current for a displacement of the parallel current path with  $v_{\perp} = 2500 \text{ m/s}$  in negative  $y$ -direction. (a) shows  $j_{\text{pol}}$  as vector field (blue arrows) and as current paths (red), (b) shows the current amplitude  $|j_{\text{pol}}|$  in color-coded representation.

an AW-frequency  $f_{ci}/2 = 20 \text{ kHz}$  a velocity  $|\vec{v}| = \omega r \approx 2500 \text{ m/s}$  is obtained. The graphical representation of the idealized ion polarization currents for this value is shown in Fig. 4.11. The radial dependence of the polarization current amplitude is

$$|j_{\text{pol}}| \sim \frac{1}{x^2 + y^2} . \quad (4.18)$$

Similar the case of the explicit time dependence in Sec. 4.2.3 the distribution is symmetric around the parallel current filament. A difference it that the convective polarization currents decrease as  $1/r^2$ . Nevertheless, the absolute value for  $x = 1 \text{ cm}$  and  $y = 0 \text{ cm}$  is of the same order of magnitude  $j_{\text{pol}} = 18.2 \mu\text{A}/\text{cm}^2$ . As seen in Fig. 4.11, the vector field of the currents has a fairly complex eddy structure. Tracing the vector field of  $\vec{j}_{\text{pol}}$  allows one to reconstruct the current streamlines. As shown in Fig. 4.11 (a) polarization currents flow along circles as expected for an eddy structure. Relative to the movement of the parallel current, the front region of the filament (A) is connected to the rear (B). In this way, a net current flows upwards in opposite direction to the filament displacement  $\vec{v}_{\perp}$ . Together with the initial parallel component a three-dimensional current pattern is constituted as shown in Fig. 4.12. The perpendicular polarization current is purely carried by ions, the parallel current mostly by electrons due to their higher mobility. The interaction of the two current types is given by the condition of quasineutrality.

To estimate the net polarization current, the current can be integrated along the  $x$ -axis at  $y = 0$ . Since currents flow along circles from the rear to the front of the

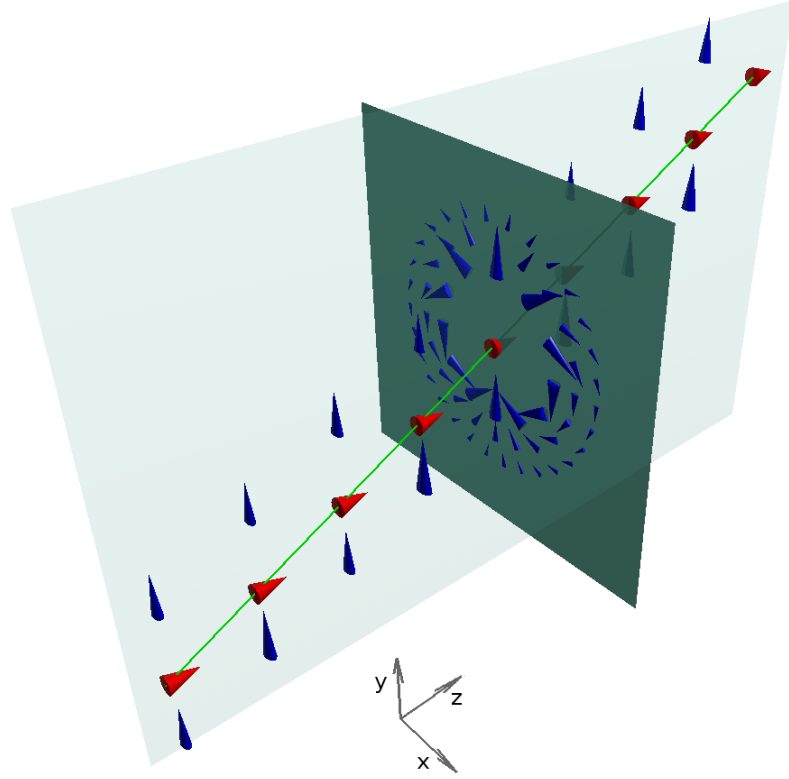


Figure 4.12: Schematic view of a downward moving current filament (red cones) of an AW. The spatial change in the electric field causes a polarization current (blue cones). The detailed view in the depicted plane corresponds to Fig. 4.11. The vertical net current vectorally adds to the initial parallel one, leading to a deflection across the ambient magnetic field. The green line indicates this.

filament, they have to pass this line at some point. At these positions,  $j_{\text{pol}}$  is directed purely in vertical direction and the total current sums up to

$$I_{\text{pol}} = \int_{-\infty}^{+\infty} j_{\text{pol},y} dx = -I_{\text{fil}} v_y \frac{\sqrt{1-f}}{v_A} \frac{\mu_0}{2\pi} \int_{-\infty}^{+\infty} \frac{1}{x^2} dx \longrightarrow \infty. \quad (4.19)$$

This result of an infinite perpendicular current is surprising. It shows that the polarization current estimated in this way is not physical. The reason is the initial assumption that the electric field  $\vec{E}_{\perp}$  as source for  $j_{\text{pol}}$  is only generated by the parallel current filament. In fact, the electric field of the polarization current itself has to be considered as well. Only a self-consistent treatment of the problem will lead to quantitative correct result. It is done in the context of the MHD-description in Sec. 3.1.4. For shear AW, the main outcome in terms of the involved currents is summarized in Fig. 3.7. The parallel current component has a complex structure and

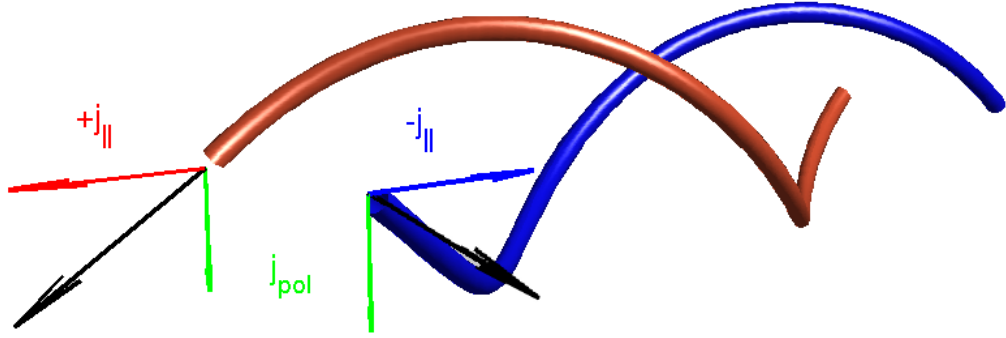


Figure 4.13: Schematic current pattern of an AW for a single time instant. It consists of parallel conduction currents carried by the electrons (red and blue arrows) and perpendicular polarization currents (green arrows) carried by the ions. The superposition (black arrows) yields two twisted current filaments in the form of a helix.

rotates in a plane perpendicular to  $B_0$ . In the regions where the parallel currents are concentrated, the local rotation velocity is opposed to the perpendicular currents. This finding is consistent with the qualitative outcome of idealizing the parallel currents as filament.

#### 4.2.5 3D-current system of a shear Alfvén wave

A description of the current pattern of shear AWs (Fig. 3.7) by two antiparallel current filaments seems to be rather crude, but in fact it is a reasonable approximation, at least for the experimental case. In VINETA the plasma density decreases radially and at  $r = 3\text{ cm}$  it is only half the centre value. The plasma is able to carry AWs only in a narrow plasma tube different from the MHD-model above, where an infinite plasma extent is assumed. This case can be approximated by a convolution of the parallel AW currents from the MHD-description with the radial density profile. The consequence is a dipole-like current pattern with a current filament flowing into the plane and a current filament flowing out of the plane.

The parallel and perpendicular AW currents result in a three-dimensional current pattern with two parallel current filaments and the related perpendicular currents. It rotates in time around the  $z$ -axis. Recall that the fluctuating quantities including the currents are described as plane waves. A change in the distance to the wave excitation point at  $z_0$  along the  $z$ -axis will have the same effect on the plane wave phase as the time. In this way a twisting of the current pattern along  $z$  can be deduced, for the discussed current system of shear AWs this is shown in Fig. 4.13. The two current filaments with opposite signs are twisted to form a helix. They

occur as a result of the superimposed parallel and perpendicular currents.

### 4.3 Rotating current patterns

The AW current pattern described by the MHD-model in Sec. 3.1.4 is based on an unbounded plasma. AWs in VINETA will significantly differ from that due to the finite size of the plasma. In experiments the fluctuating magnetic field is recorded in azimuthal planes to reconstruct the parallel current pattern.

#### 4.3.1 Measurement of parallel currents

The fluctuating magnetic field of a wave in an azimuthal plane is recorded in a similar way as in the radial-axial plane (Sec. 4.1.1). The only difference is the use of a positioning system capable of moving the  $\vec{B}$ -probe along the  $x$  and  $y$  coordinates. The plane is located at a distance of  $\Delta z = 1551$  mm from the excitation antenna. A range of  $x = -85 \dots 90$  mm and  $y = -86 \dots 89$  mm, with a stepsize of 7 mm was chosen. For each point on the grid, a discharge in argon was started for about 1 s. After a transient phase, the plasma is stationary and AWs are excited for 100 ms with an amplitude  $b_y = 1.8$  mT. The wave excitation frequency was  $f = 29.50$  kHz, close to the ion-cyclotron frequency  $f_{ci} = 29.56$  kHz. The ambient magnetic field was set to  $B_0 = 77$  mT. The four probe signals were recorded together with a signal proportional current in the antenna as reference. Conditional averaging (cf. Sec. 2.6) and absolute calibration of the signals of the  $\vec{B}$ -probe (cf. Sec. 2.2.4) result in the three time series  $b_x(t)$ ,  $b_y(t)$ , and  $b_z(t)$ . The perpendicular components ( $b_x, b_y$ ) are shown in Fig. 4.14 (a) and (b) for three time instants, spanning half a wave period. In this representation, the resolution is increased for the color-coded amplitude of  $b_\perp$  and decreased for the vector field plot.

At  $t = 0 \mu\text{s}$ , the wave magnetic field has a peak amplitude in the center of the plane of  $b_\perp = 1.41 \mu\text{T}$ . It has a dipole-like structure tilted by approximately  $45^\circ$ . In the curls of the dipole, the field drops off to  $0.10 \mu\text{T}$ . The structure is counterclockwise rotated at  $t = T/4 = 8.5 \mu\text{s}$  by approximately  $90^\circ$ , as illustrated in Fig. 4.14 (b). The absolute values of  $b_\perp$  in Fig. 4.14 (b) for  $t = 8.5 \mu\text{s}$  are not a rotated version of the pattern at  $t = 0 \mu\text{s}$ . In fact, the field has a more complicated structure and is not similar to the one found for  $t = 0 \mu\text{s}$ . The amplitudes are reduced in the entire plane, the value in the center is  $b_\perp = 0.58 \mu\text{T}$ . After another  $T/4$  at  $t = 17 \mu\text{s}$ , the initial situation recovers and  $b_\perp$  has the same dipole-like structure as for  $t = 0 \mu\text{s}$ , but with reversed field direction in Fig. 4.14 (b). Based on this measurement, the

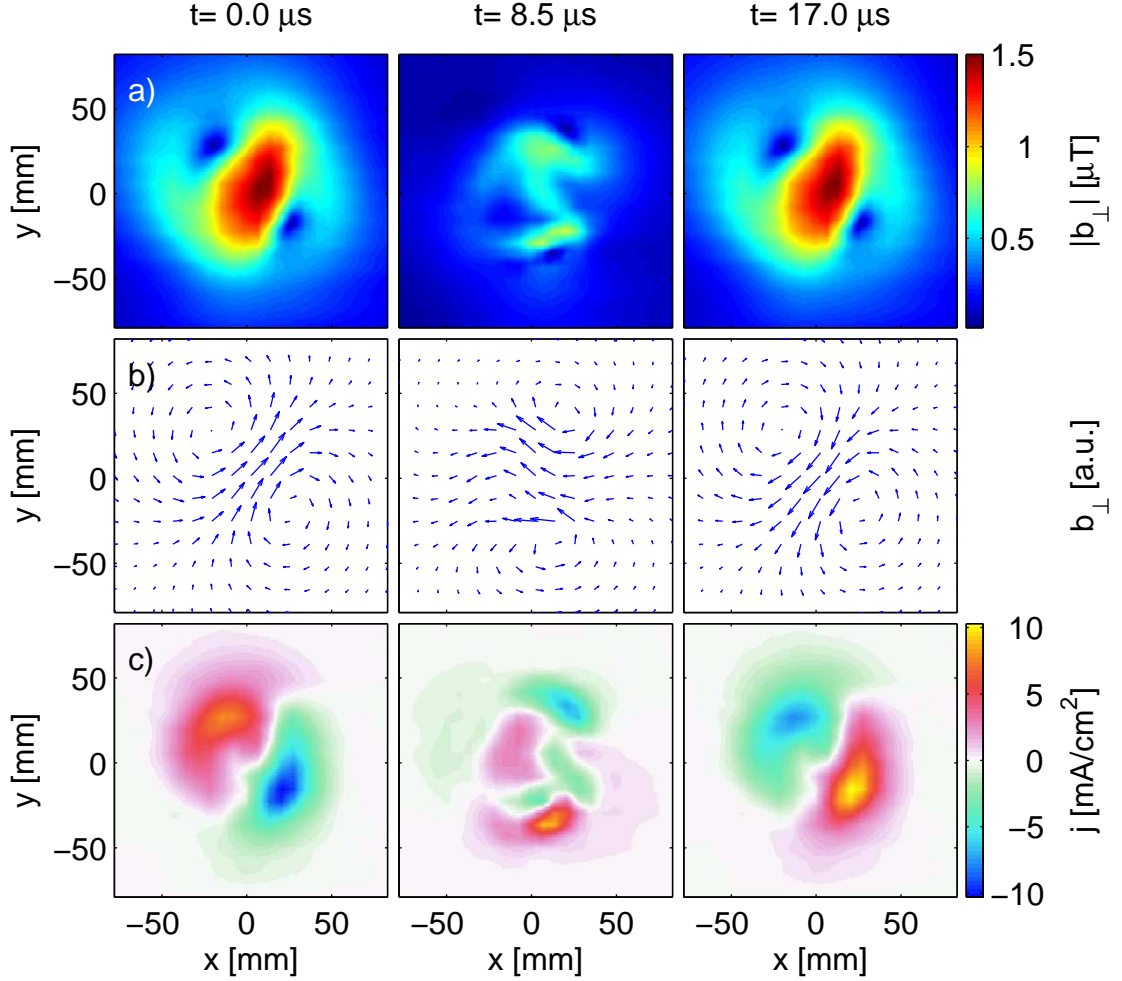


Figure 4.14: Azimuthally resolved measurement of fluctuating magnetic field of a wave excited at  $f = 29.50$  kHz. The plane is located at  $\Delta z = 1551$  mm downstream from the exciter antenna. The ambient magnetic field points into the plane, the ion gyration direction is counterclockwise. The absolute value of  $b_{\perp}$  in (a) is complemented by a vector field representation in (b) and the parallel current density  $j_z$  in (c). The time evolution of the fields and currents is given column-wise as time step of  $\Delta t = f^{-1}/4$ .

parallel current density  $j_z$  was calculated using Ampère's law (3.2). It reads for the parallel component

$$j_z = \frac{\partial b_x}{\partial y} - \frac{\partial b_y}{\partial x} . \quad (4.20)$$

The result is shown in Fig. 4.14 (c). The maximum current density is located at the curls of the magnetic field dipole with changing signs for different curl directions. The location coincides with the minimum of the magnetic field. The parallel current

density vanishes at the maximum of the magnetic field in the center of the plane. The largest value of the parallel current density is  $j_z = 7.8 \text{ mA/cm}^2$  for  $t = 0 \mu\text{s}$ . There is no decrease in amplitude with time different from the magnetic field. In fact, the maximum value is  $j_z = 9.0 \text{ mA/cm}^2$  for  $t = T/4$ . At  $t = T/2$  the parallel current density reoccurs with changed sign compared to  $t = 0 \mu\text{s}$ , which is consistent with the time evolution of the magnetic field structure.

### 4.3.2 Rotational decomposition

A main outcome of the MHD-model described in Sec. 3.1.6 is that the current distribution of AWs can be treated as rotating rigid body. The time dependence of  $\vec{j}(t)$  is fully described by the spatial rotation. There is no explicit time dependence, neither for shear nor for fast AW. In contrast, the measured parallel current pattern cannot be described by a simple rotation in time.

The MHD model has two solutions with rotation in opposite directions. Both solutions can exist simultaneously. A possible explanation of the experimental findings is that more than one wave type is excited and the superimposed currents create the observed current pattern. The hypothesis is supported by the run of the measured dispersion relation (Sec. 4.1.3), which is in-between the two branches for shear and fast AWs.

In linear treatment the simultaneous wave occurrence is described as superposition of all fields and currents. It can be unfolded by a 2D-Fourier decomposition of the time evolution of the current pattern. Clock- and counterclockwise rotating parts can be distinguished as mode numbers with positive and negative signs. With the coordinates of the measured  $j_z(x, y, t)$  transformed to polar coordinates  $j_z(r, \theta, t)$  the Fourier decomposition reads

$$j_z(r, m, \omega_n) = \frac{1}{2\pi T} \int_0^{2\pi} \int_0^T j_z(r, \theta, t) e^{-i\omega_n t} e^{-im\theta} dt d\theta \quad (4.21)$$

$$\omega_n = \frac{2\pi}{T} \cdot n, \quad m = 0, \pm 1, \pm 2, \dots$$

The transform maps the angle  $\theta$  and the time  $t$  to the wave number  $m$  and the frequency  $\omega$  in Fourier space, the radius  $r$  is kept as a parameter.

Fig. 4.15 shows a result for  $r = 25 \text{ mm}$ , based on the data shown in Fig. 4.14. The amplitude of the current density at  $r$  represents a dominant  $m = 1$  mode [Fig. 4.15 (a)]. Interpolating for subsequent time steps along the circle yields the time evolution of  $j_z(r, \theta, t)$  in Fig. 4.15 (b). For  $t = 0 \mu\text{s}$ , the structure of the current density in

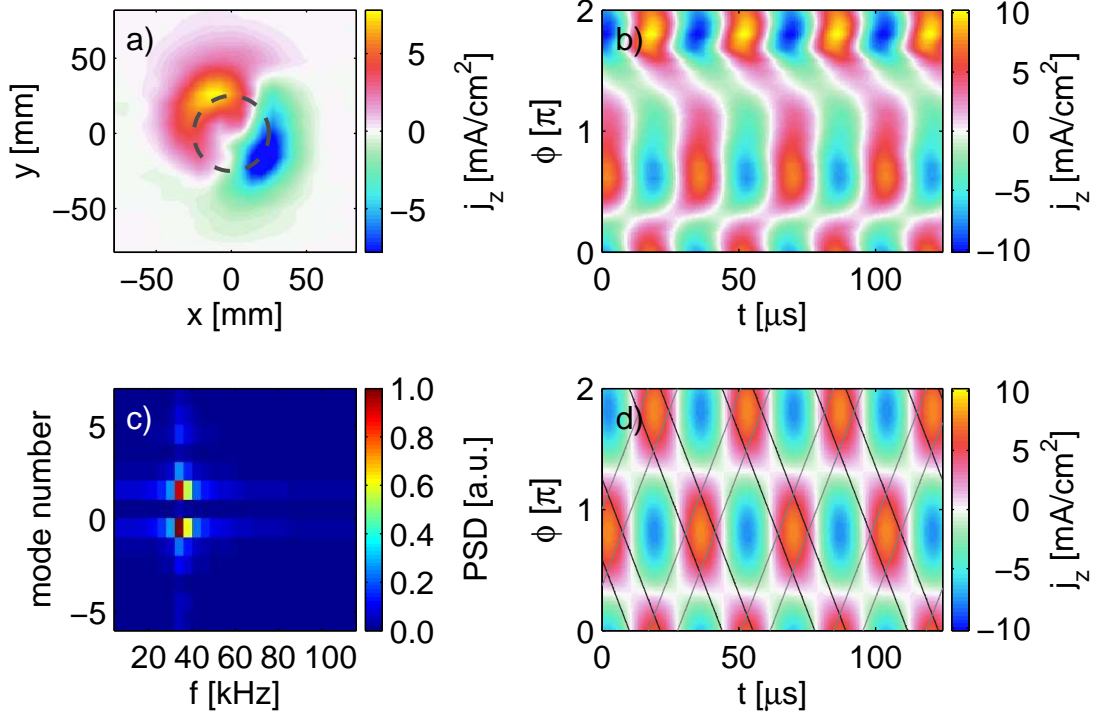


Figure 4.15: Decomposition of  $j_z$  into rotating modes. (a) Current density measured in an azimuthal plane  $\Delta z = 1551$  mm downstream of the excitation antenna, shown for  $t = 0 \mu\text{s}$ . (b) Space-time evolution of the current density along the dashed circle ( $r = 25$  mm) in (a) for  $t = 0 \dots 500 \mu\text{s}$ . (c) The frequency mode-number spectrum of (b), it is dominated by two modes with  $m = \pm 1$  at 29.5 kHz. (d) The reconstructed spatio-temporal current density shows main features of the original  $j_z(t, \phi)$  in (b). The phase fronts of the two superposed modes are indicated with gray lines.

Fig. 4.15 (a) in azimuthal direction has a minimum and a maximum around  $\theta = 1.8\pi$  and  $\theta = 0.7\pi$ , respectively. The absolute values at these points are  $-10.7 \text{ mA/cm}^2$  and  $+7.2 \text{ mA/cm}^2$ . The time evolution of the stripe pattern has a vertical orientation around these extrema. The extrema of the parallel current do not propagate azimuthally, but flip sign after  $T/2$ . The frequency mode-number spectrum is shown in Fig. 4.15 (c). There are two dominating modes of  $j_z(m, \omega)$  with  $m = +1$  and  $m = -1$  at the excitation frequency  $f = 29.5$  kHz. This proves that the space-time evolution in Fig. 4.15 (b) is a superposition of clockwise and counterclockwise rotating ( $|m| = 1$ ) modes. The inverse Fourier transformation taking into account only these two modes reads

$$j_z(r, \theta, t) = j_z(r_0, m = 1, \omega_0)e^{i\theta} + j_z(r_0, m = -1, \omega_0)e^{-i\theta} \quad , \quad (4.22)$$

and yields the space-time pattern in Fig. 4.15 (d). The phase fronts of the two modes

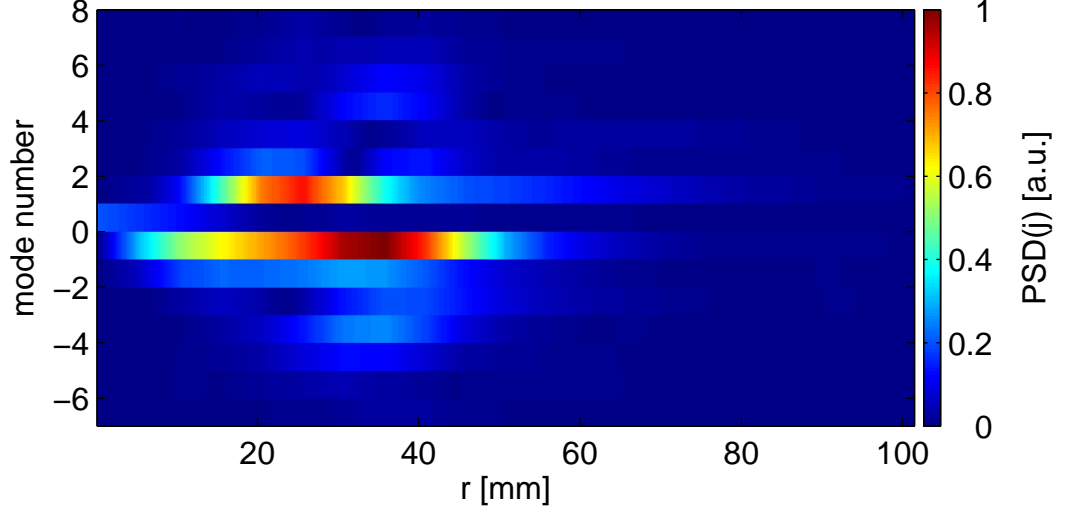


Figure 4.16: Discrete mode spectrum of parallel current  $j_z$  as a function of  $r$ . Positive mode numbers correspond to clockwise rotation, negative ones to counterclockwise rotation. All spectral components are taken at the excitation frequency  $\omega_0$ .

are indicated. Major qualitative and quantitative features of the measured space-time pattern in Fig. 4.15 (b) are reproduced. The amplitudes are slightly reduced to  $\pm 7.1 \text{ mA/cm}^2$  due to the neglected components at larger mode numbers  $|m| > 1$ .

The mode number frequency spectrum in Fig. 4.15 (c) has only one significant frequency peak at the excitation frequency  $\omega_0$ . Considering only components at  $\omega_0$  leads to the radially resolved mode spectrum in Fig. 4.16. It is clearly dominated by the two mode numbers  $m = \pm 1$  for all radii. There is a radial localization of these two modes. The  $m = -1$  mode is dominant with a peak at  $r = 35 \text{ mm}$ . The peak of the  $m = +1$  mode is slightly less in amplitude. It is inward shifted to  $r = 26 \text{ mm}$  and the radial extent is significant smaller.

A reconstruction of the  $m = \pm 1$  modes in the azimuthal cross-section is shown in Fig. 4.17 (b) and (c). The calculation was performed with (4.22) using the complex valued  $\tilde{j}_z(r, \pm 1, \omega_0)$ . The current density structure is sheared with characteristic spiral-like tails, mostly pronounced for the clockwise rotating  $m = +1$  mode in Fig. 4.17 (c). As expected from the distribution of the radial mode spectrum, the  $m = -1$  mode is located at larger radii than the  $m = +1$  mode [Fig. 4.17 (b)]. The latter also has a larger amplitude. The time dependency of the two modes is fully attributed to the rotation of the individual patterns, there is no explicit time dependency (cf. Eq. 4.22). The superposition of the two rotating modes leads to the current density pattern shown in Fig. 4.17 (d). The maximum amplitude is reduced by 35% compared with the measured pattern due to the neglected Fourier

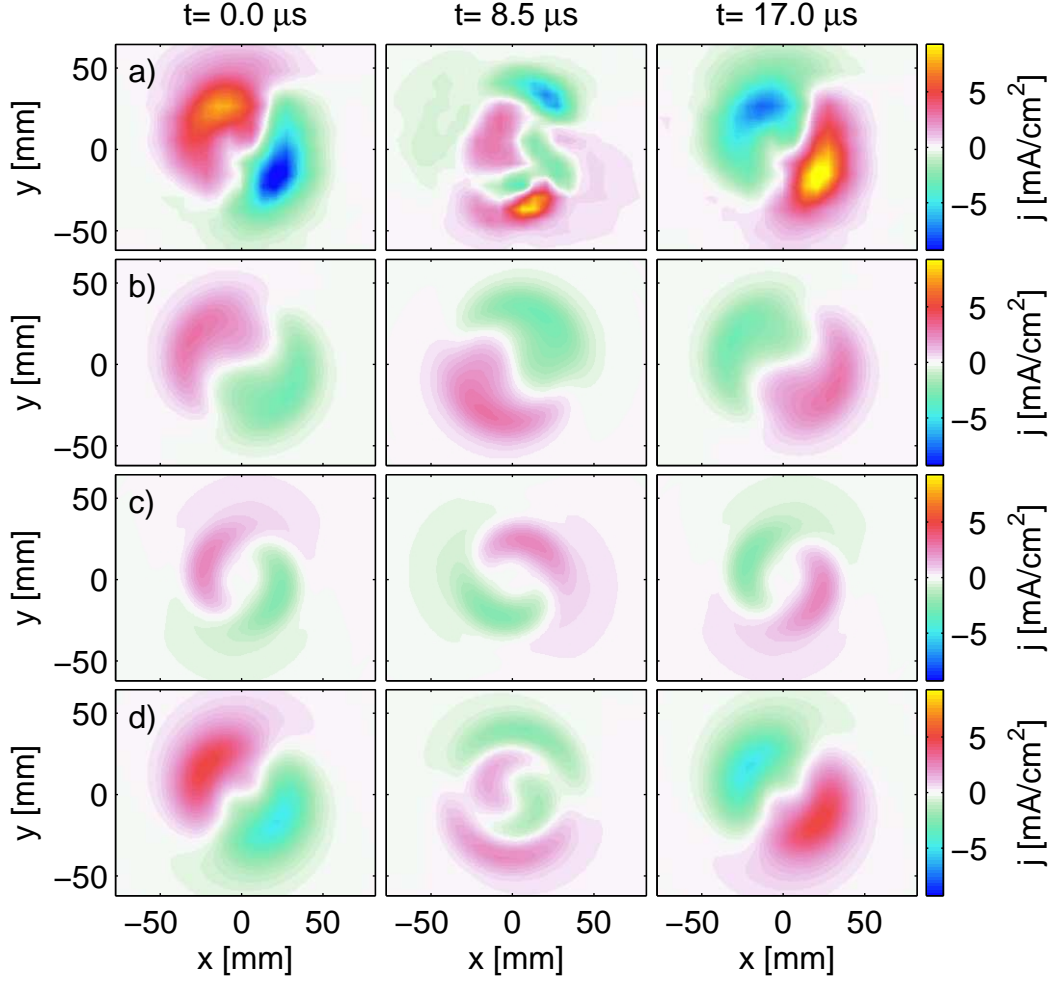


Figure 4.17: Rotational decomposition of current pattern. The measured current density  $j_z(x, y, t) \equiv j_z(r, \theta, t)$  — shown in a) for  $t = 0 \mu\text{s}$  — is 2D-Fourier decomposed with the distance  $r$  to the coordinate origin as parameter. Two modes are dominant, the clockwise rotating  $m = +1$ -mode in (c) and the counterclockwise rotating  $m = -1$ -mode in (b). Superimposing both modes results in the current density in (d) with similar qualitative and quantitative properties as the measured current density in (a).

components. Despite this difference, general features of the current density pattern are well reconstructed. Both patterns have one maximum and one minimum for the first and last time step at  $t = 0 \mu\text{s}$  and  $t = 17 \mu\text{s}$ . These are located roughly at the same locations. For the time instant  $t = 8.5 \mu\text{s}$ , the more complex structure in the measured current density pattern is reproduced to a certain degree as well.

In conclusion, the measured current distribution and is attributed to two simulta-

neously excited waves: one with clockwise rotating wave field and one with counterclockwise rotating field. The dominant  $m = -1$  wave rotates in the direction of ion gyration. It is assumed to be the desired left-hand polarized shear AW that is excited with the above described excitation scheme. It has to be distinguished from the simultaneously excited clockwise rotating wave, e.g. by Fourier decomposition.

### 4.3.3 Polarization decomposition

A rotating wave of the above discussed type is connected to off-axis parallel currents that generate on the axis a magnetic field. If the polarization of the wave is purely circular, the wave magnetic field has a constant amplitude and rotates with angular velocity  $\omega$ . The wave is left-hand polarized if it rotates counterclockwise and  $\vec{k}$  points into the plane. This can be described by a complex field amplitude  $L$ . The time evolution of the field components is

$$b_x^L(t) = \Re(L \cdot e^{-i\omega t}) \quad b_y^L(t) = \Im(L \cdot e^{-i\omega t}) \quad . \quad (4.23)$$

Correspondingly, the clockwise rotating field corresponds to right-hand polarization. With a complex amplitude  $R$ , the time evolution of the field components is:

$$b_x^R(t) = \Re(R \cdot e^{+i\omega t}) \quad b_y^R(t) = \Im(R \cdot e^{+i\omega t}) \quad . \quad (4.24)$$

If the two wave types coexist, the two components of the magnetic field  $b_x$  and  $b_y$  can be written as harmonic functions in terms of complex wave amplitudes  $C$  and  $D$ :

$$b_x(t) = \Re(C \cdot e^{-i\omega t}) \quad b_y(t) = \Re(D \cdot e^{-i\omega t}) \quad . \quad (4.25)$$

This definition differs slightly from (4.23) and (4.24) since only real parts are considered. It is the general definition of an elliptically polarized wave field. There is a one-to-one mapping between  $\{C, D\}$  and  $\{L, R\}$ . The magnetic field fluctuations read as

$$b_x(t) = b_x^L(t) + b_x^R(t) = \Re(L \cdot e^{-i\omega t}) + \Re(R \cdot e^{+i\omega t}) \quad (4.26)$$

$$b_y(t) = b_y^L(t) + b_y^R(t) = \Im(L \cdot e^{-i\omega t}) + \Im(R \cdot e^{+i\omega t}) \quad . \quad (4.27)$$

These equations can be expressed as

$$\Re(C \cdot e^{-i\omega t}) = \Re(L \cdot e^{-i\omega t}) + \Re(R^* \cdot e^{-i\omega t}) \quad (4.28)$$

$$\Re(D \cdot e^{-i\omega t}) = \Re(L \cdot e^{-i(\omega t + \pi/2)}) - \Re(R^* \cdot e^{-i(\omega t + \pi/2)}) \quad . \quad (4.29)$$

This real-valued equation system is a particular solution of the complex-valued system. Dividing by the phase factor yields

$$C = L + R^* \quad D = (L - R^*) e^{-i\pi/2} \quad . \quad (4.30)$$

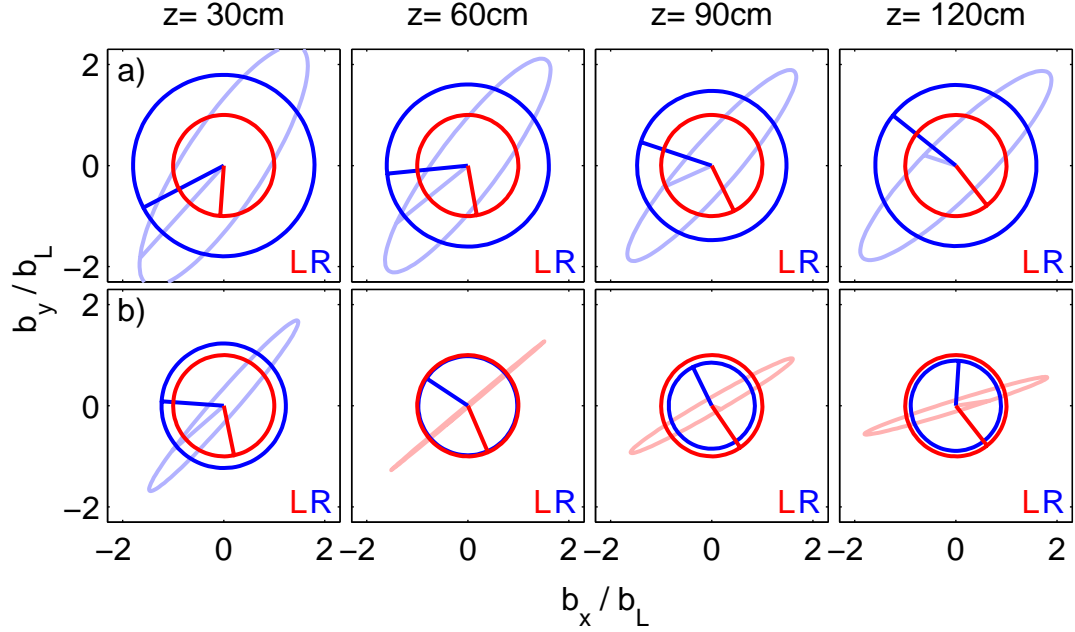


Figure 4.18: Polarization decomposition of dynamic magnetic field on axis at  $x = y = 0$  mm. The measured amplitudes for  $b_x$  and  $b_y$  (light red, light blue) are elliptically polarized. A decomposition into left and right rotating fields is performed (red, blue), with all shown amplitudes normalized to the amplitude of the left rotating field. The figure shows measurements at different  $z$ -positions with an excitation frequency of  $f = 35$  kHz (a) and  $f = 45$  kHz (b). The lines to the coordinate origin indicate the phase for  $t = 0$   $\mu$ s.

If the complex amplitudes of the elliptically polarized wave are measured, the amplitudes of the circular polarized waves are

$$L = \frac{C + D e^{i\pi/2}}{2} \quad R = \frac{C^* + D^* e^{i\pi/2}}{2} . \quad (4.31)$$

This mapping is applied to the wave fields  $b_x$  and  $b_y$  obtained in the AW-dispersion experiments presented in Sec. 4.1.3. Fig. 4.18 shows the result for two frequencies one below and one above  $f_{ci}$ . In the representation the magnetic field is normalized to the amplitude of the L-wave. For  $z = 30$  cm and an excitation frequency of 35 kHz the measured time evolution of the magnetic field  $\vec{b}(t)$  has an ellipse shape and is elongated along the diagonal [Fig. 4.18 (a)]. The described polarization decomposition results in an R-wave with an amplitude 80% larger than the amplitude of the L-wave. Superimposing the two waves results in the measured magnetic field with elliptical polarization for every instant in time. Following the wave axially along

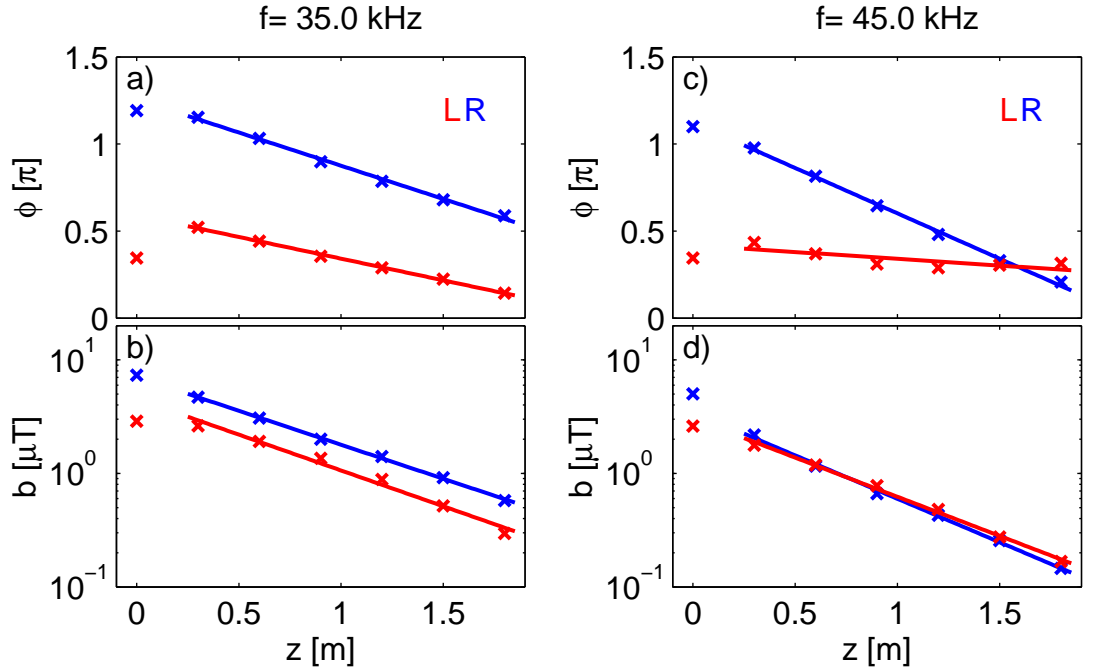


Figure 4.19: Phases and amplitudes of left-hand and right-hand polarized waves along propagation axis  $z$  for  $f = 35$  kHz (a, b) and  $f = 45$  kHz (c, d). The linear and exponential fits (solid lines) were done in the  $z$ -range  $0.3 \dots 1.8$  m outside the short-distance antenna field.

the four shown positions, a smooth evolution of the direction of the magnetic field vector of the two circular waves is observed. For the L-waves the phase change with distance is with slightly smaller than for the R-waves. The amplitude of the R-wave is higher than for the L-wave for all positions. Although there is a decrease of the amplitude ratio for the first 3 positions, this trend does not apply to the entire  $z$ -range. The frequency in Fig. 4.18 (b) is  $f = 45$  kHz  $> f_{ci} = 39.2$  kHz. The measured polarization ellipses are closer to linear polarization. At  $z = 60$  cm the orientation of the ellipse changes, indicated with a different color. The rotation direction is equal to the rotation of the maximum component of the corresponding two circularly polarized waves. Again there is a smooth evolution of the direction of the magnetic field vectors for the two wave types. Compared with  $f = 35$  kHz the phase change with distance is increased for R-waves and decreased for L-waves. The phase slope  $d\phi/dz$  is equal to  $|\vec{k}|$ , see (4.3). The different slopes for L- and R-waves correspond to different wave lengths  $\lambda = 2\pi/k$ . This allows one to distinguish between the dispersion of L- and R-waves.

For a quantitative analysis the complex amplitudes of the L- and R-waves are shown

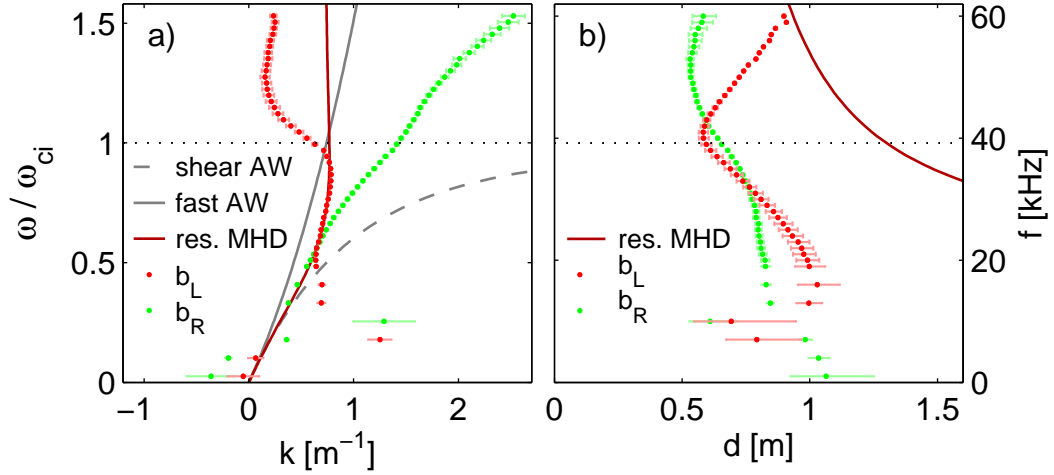


Figure 4.20: Dispersion relation of excited waves after polarization decomposition. Diagram (a) shows the real part of the dispersion  $k(\omega)$  and (b) the damping length  $d(\omega) = 1/k_i(\omega)$ . The theoretical dispersion curves from Hall-MHD description for shear and fast AWs (dashed and solid grey line) as well as the dispersion curve and damping from the resistive Hall-MHD theory for shear AWs with a normalized resistivity  $R = 0.93$  as fit parameter (solid red line) are included.

in Fig. 4.19 in another representation with the axial runs of the phases and amplitudes. For  $f = 35$  kHz the R-wave is the dominant one. The damping length  $d$  is calculated from the slope in the semilogarithmic plot. The first position at  $z = 0$  cm is omitted because of antenna near-field effects (cf. Sec. 4.1.1). For the driver frequency  $f = 35$  kHz damping length is  $d_L = 69$  cm for the L-wave and  $d_R = 73$  cm for the R-wave. For  $f = 45$  kHz, the absolute amplitudes of the two circularly polarized waves are almost equal. The determined damping lengths are  $d_L = 63$  cm and  $d_R = 57$  cm. The phase as function of  $z$  [Fig. 4.19 (a) and (b)] yields slopes of  $45^\circ/\text{m}$  (35 kHz) and  $69^\circ/\text{m}$  (45 kHz) for L-waves and  $69^\circ/\text{m}$  (35 kHz) and  $94^\circ/\text{m}$  (45 kHz) for R-waves.

### Dispersion relation of L- and R-waves

A polarization decomposition into L- and R-wave is done for all frequencies in the range of  $f = 5 \dots 60$  kHz of the experimental data in Sec. 4.1.3. From the slope of  $\phi(z)$  the modulus of the wave vector  $k(\omega)$  is calculated. The decrease of the amplitudes during propagation  $b_{L/R}(z)$  yields the damping length  $d(\omega)$ . The resulting dispersion relations for the two wave types are shown in Fig. 4.20 (a) and (b). The dispersion of the L-wave starts for the lowest frequency 5 kHz with  $k_z \approx 0 \text{ m}^{-1}$ . For

frequencies up to 19 kHz, the wave vectors show a spread and are scattered in the range  $k = 0 \dots 1.25 \text{ m}^{-1}$ . For frequencies higher than 19 kHz the dispersion relation has a smooth run. The maximum wave vector  $k = 0.79 \text{ m}^{-1}$  is found at 34 kHz, followed by a minimum  $k = 0.16 \text{ m}^{-1}$  at 50 kHz. The dispersions of R-wave and L-wave differ significantly. The dispersion curve of the R-wave is mostly linear. It starts with a negative  $k = -0.36 \text{ m}^{-1}$  at 5 kHz and increases up to  $k = 2.53 \text{ m}^{-1}$  at 60 kHz. There are small deviations from linear dispersion, the measured  $k$  values are shifted towards higher values at  $f = 38 \text{ kHz}$  and towards lower values at  $f = 48 \text{ kHz}$ . The damping length of the L-wave is dominated by a clearly defined minimum  $d = 0.58 \text{ m}$  at 41 kHz, very close to the ion-cyclotron frequency. The damping length increases up to 90 cm at 60 kHz and 103 cm at 16 kHz. For lower frequencies  $\leq 16 \text{ kHz}$ , the damping lengths of both L- and R-waves have a broader spread. The spread in the dispersion relation and the damping length below  $f = 19 \text{ kHz}$  is most likely caused by drift waves. Drift waves have a similar frequency range and can directly interact with the excited Alfvén waves, as described in Sec. 5.3. The parallel wave length of the drift waves is typically close to the machine length of  $l = 4.5 \text{ m}$  [42]. The experimentally observed wave length in the frequency range of the spread is  $\lambda = 5m$ .

To compare the measured dispersion relations with theory three calculated dispersion relations are included in Fig. 4.20. These are the dispersion curves for shear and fast AWs as obtained from Hall MHD (3.19) and the dispersion curve for left-hand polarized shear AWs as obtained from resistive Hall MHD. The resistivity  $R$  (3.27) is used as fit parameter and one obtains  $R = 0.93$ . The resulting damping curve is included in Fig. 4.20 (b). Fig. 4.20 (a) demonstrates that the measured dispersion relations of the circular polarized waves differ significantly from the Hall-MHD model. The resistive Hall-MHD model fits the L-wave dispersion below  $\omega_{ci}$  quite well. No good agreement is observed for the damping as the predicted damping lengths are systematically higher than the observed ones.

All MHD-models used here assume an unbounded plasma, however, boundary effects play a role in experiment. Since the observed damping lengths are in the range  $d = 1 \text{ m}$ , locally launched waves will hardly reach the end plates of the device. The amplitude of the reflected wave is therefore low and has negligible influence on the launched wave. Furthermore, in the low-frequency limit the group velocity  $v_g$  is well aligned to the ambient magnetic field. We can conclude that the low-frequency shear AW is not significantly influenced by the radial or axial plasma boundaries.

Close to the ion-cyclotron resonance  $\omega_{ci}$  this reasoning is not correct any more. As shown in Fig. 3.5 in the low-frequency limit phase and group velocity are equal and

vanish for perpendicular propagation:

$$v_{\text{ph}} = \frac{\omega}{k} = v_{\text{gr}} = \frac{\partial \omega}{\partial k} \xrightarrow{\theta \rightarrow 90^\circ} 0 . \quad (4.32)$$

This means that shear AWs propagate only parallel to the ambient magnetic field. On the other hand, for frequencies close to  $\omega_{ci}$  the group velocity has a pole  $v_{\text{gr}} \rightarrow \infty$ . Shear AWs with frequencies close to  $\omega_{ci}$  propagate also perpendicular to the ambient magnetic field and cannot be described by simple theory. The same applies to fast AWs at any frequency. They propagate both parallel and perpendicular to the ambient magnetic field (cf. Sec. 4.1.3). The discrepancy between theory and measurement of the damping length can be attributed to a neglected parallel resistivity  $\eta_{\parallel} = 0$  in (3.25). As shown in Sec. 4.2.1, the main currents of AWs in the low frequency range  $\omega \ll \omega_{ci}$  are parallel currents. Hence, the calculated damping lengths in the low frequency range are systemtically overestimated.

## Chapter 5

# Experimental drift wave investigations

In the magnetized plasmas of VINETA plasma density fluctuations of up to 15 % are observed. They are localized in the radial gradient region. These fluctuations are either coherent drift wave modes [53] with mode numbers  $m = 1 \dots 9$  or weakly developed drift wave turbulence [94]. In both cases drift waves are associated with propagating density structures [43, 103]. For coherent drift modes, linear theory and experiment agree quite well [42, 104].

### 5.1 Basic properties of drift waves in VINETA

The main features of the observed density fluctuations are compiled in Fig. 5.1. The radial density profile  $n(r)$  has a peak in the center, as it is typical for helicon discharges. In the center it is  $5.3 \cdot 10^{18} \text{ m}^{-3}$  and decreases radially by about one order of magnitude to  $4.7 \cdot 10^{17} \text{ m}^{-3}$ . The radial density gradient extends over  $\pm 20 \dots 50 \text{ mm}$ . At the maximum gradient at  $r = \pm 40 \text{ mm}$  the density fluctuation amplitude peaks at  $\tilde{n}/n \approx 16 \%$  [cf. Fig. 5.1 (a)]. In the center of the plasma one has only  $\tilde{n}/n \approx 0.8 \%$ . The localisation of the density fluctuations indicate a gradient-driven instability, e.g. drift waves.

Fig. 5.1 (b) shows the power spectral density for two sets of slightly different discharge parameters. In the first case, a broad spectrum is found. Towards high frequencies there is a power law decay of 4.4 dB per octave. At 1.1 kHz, a coherent signal is superimposed on the broad band with four higher harmonics. This is a typical example for weakly developed drift wave turbulence. A change of pressure  $p$  and

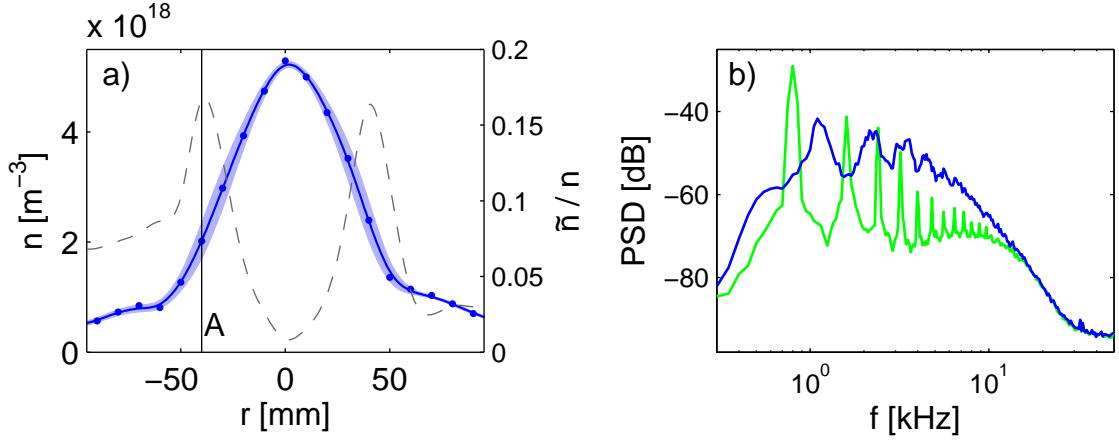


Figure 5.1: Radial profile of plasma density fluctuations in an argon discharge at a neutral gas pressure of  $p_{\text{Ar}} = 0.17 \text{ Pa}$  and an ambient magnetic field of  $B_0 = 92 \text{ mT}$ . The time-averaged radial plasma density profile  $n_0$  in (a) (blue line) is superimposed over the normalized amplitude of density fluctuations as  $n + \sigma(n(t))$ . It is illustrated as light blue range  $(n - \tilde{n}) \dots (n + \tilde{n})$  and as relative fluctuation amplitude  $\tilde{n}/n_0$  (dashed line). For the radial position marked with  $A$  at the maximum fluctuation amplitude, the power spectral density of  $n(t)$  is presented in (b) (blue). Changing the discharge parameters slightly to  $p_{\text{Ar}} = 0.28 \text{ Pa}$  and  $B_0 = 77 \text{ mT}$  has only little influence on the time-averaged profile, but significantly alters the fluctuation spectrum (green).

magnetic field  $B_0$  acts on the drift wave dynamics via the drift scale  $\rho_s \sim 1/B_0$  and the collisionality  $\nu$ . A spectrum for slightly changed discharge parameters is shown in Fig. 5.1 (b). Here, a coherent drift mode is destabilized. The mode frequency is  $800 \text{ Hz}$ , with a large number of higher harmonics. For frequencies  $f \geq 15 \text{ kHz}$ , again a power law decay is observed. It has the same slope and the same magnitude as in the weakly developed drift wave turbulence. The regime of weakly developed drift wave turbulence is determined by the motion of ions, mainly perpendicular to the ambient magnetic field. Therefore an inverse energy cascade between modes is expected, similar to 2D-fluids [105], transferring energy from small to high scale structures. Given by the DW dispersion relation (cf. Fig. 3.10) this is equivalent to an energy transfer from high to low frequencies. Experimental evidence for the inverse energy transfer is found by a bicoherence analysis for experimental DW fluctuation data from VINETA [106].

## 5.2 Parallel currents of drift waves

As outlined in Sec. 3.2, the dynamics of drift waves are intrinsically 3-dimensional. The associated currents of the parallel electron response are measured as for Alfvén waves in Sec. 4.2. The azimuthal  $(x, y)$ -plane is scanned on a grid with  $27 \times 19$  points using a  $\vec{B}$ -probe and a Langmuir probe. The spatial distance between the  $\vec{B}$ -probe and the Langmuir pin is considered as offset in the coordinates. A second Langmuir probe is used as a phase reference, it is located in the density gradient region of the plasma. At each grid point, the ion saturation current of the two probes and the magnetic signals are recorded during a discharge. The calibrated probes (cf. Sec. 2.2) yield time series of the fluctuating magnetic components  $b_x(t)$ ,  $b_y(t)$ , and  $b_z(t)$ . By conditional averaging fluctuating structures in the azimuthal plane are reconstructed. The spatio-temporal fields  $\tilde{n}(x, y, t)$ ,  $b_x(x, y, t)$ ,  $b_y(x, y, t)$ , and  $b_z(x, y, t)$  of an  $m = 3$  drift mode are shown in Fig. 5.2 for three time instants.

The density fluctuation structure Fig. 5.2(a) has three maxima and minima. The mode pattern rotates at a frequency of  $f = 2.8$  kHz in the electron diamagnetic drift direction, the frequency recorded at a fixed position is  $3f = 8.3$  kHz. The fluctuating magnetic field distribution Fig. 5.2(b) is dominated by six vortices in the vector field with consecutive left- and right-hand orientation. The parallel current  $j_{\parallel}$  is calculated with Ampère's law (4.20) from the perpendicular magnetic field  $b_{\perp}(x, y)$ . The resulting current density is depicted in Fig. 5.2(c). The pattern of the parallel current correlates well with the one of the density fluctuations. For a quantitative analysis the local minima and maxima of the current and density structures are detected. Absolute values are compiled in Tab. 5.1. Although the measurement error is rather high, a small spatial displacement was observed between the extrema of current and density. The same measurement was done for a  $m = 2$  drift mode, the spatio-temporally resolved density and currents are shown in Fig. 5.3, absolute values are compiled in Tab. 5.1 as well. The maximum fluctuation amplitudes are smaller compared with the  $m = 3$  mode. Although less significant, a small spatial displacement between the extremas of current and density was also found for the  $m = 2$  mode. The parallel currents are spatially displaced relative to the density fluctuations towards the plasma edge and slightly ahead of them into the drift direction.

The density fluctuations are located in the region of steepest radial density gradient. The current patterns show a displacement relative to the density, most significant in the radial direction. In the drift wave model, the currents respond to plasma potential fluctuations. Unstable drift waves require a small phase shift between potential and density, with the density developing ahead of the potential while propagating in drift direction [107, 108]. As mentioned above the measured phase

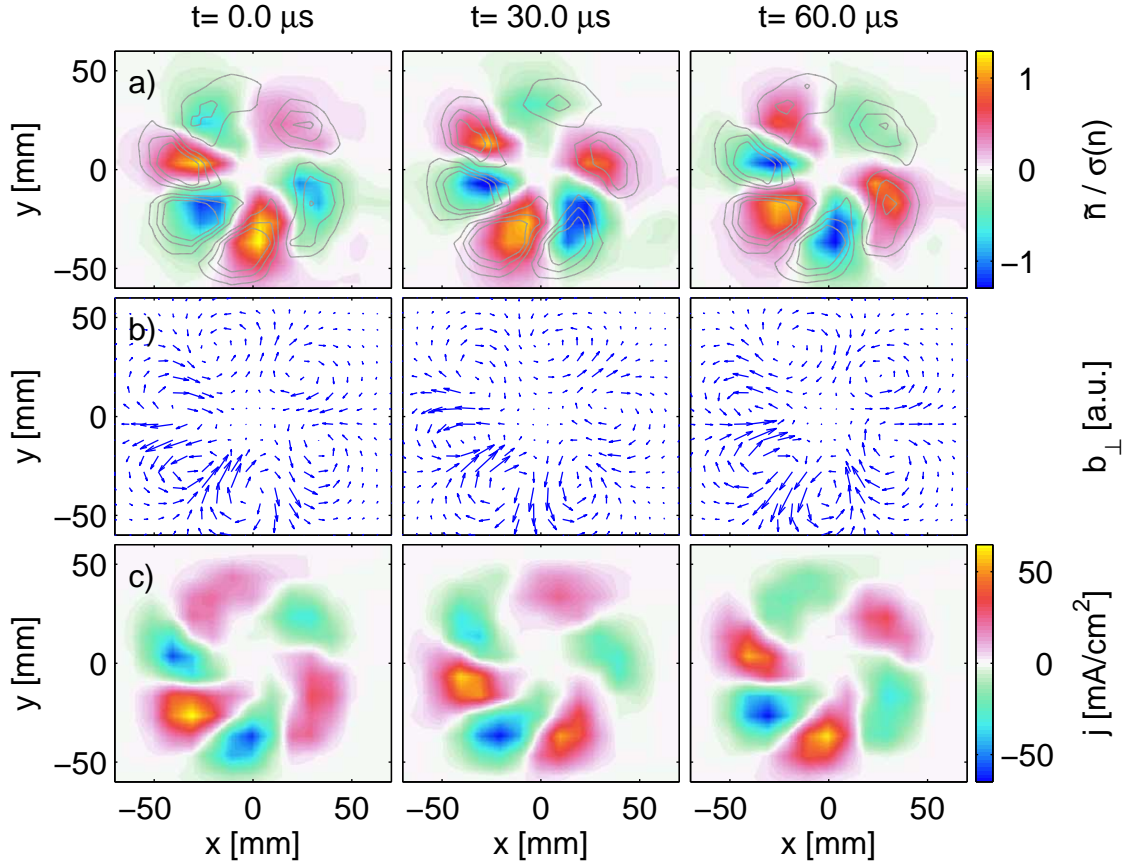


Figure 5.2:  $m = 3$  drift wave mode in azimuthal plane. The discharge parameters are  $p_{Ar} = 0.21$  Pa and  $B_0 = 81$  mT. The ambient magnetic field points into the plane with a clockwise electron diamagnetic drift direction. Fields and currents are shown for three time instants with  $\Delta t = T/4$ . The density fluctuation density (a) is superposed on the isolines of the parallel current density  $j_{\parallel}$  (c) at the levels  $-30, -20, \dots, +20$  mA/cm<sup>2</sup>. The current density  $j_{\parallel}$  is calculated via the rotation of the measured magnetic field components  $b_x$  and  $b_y$ , shown in (b).

shift between  $j_{\parallel}(\vec{r})$  and  $n(\vec{r})$  shows that  $j_{\parallel}$  flows ahead of the density. Both density and current pattern are located at larger radii for higher mode numbers, which is in qualitative agreement with dispersion calculations of drift waves in cylindrical coordinates [87].

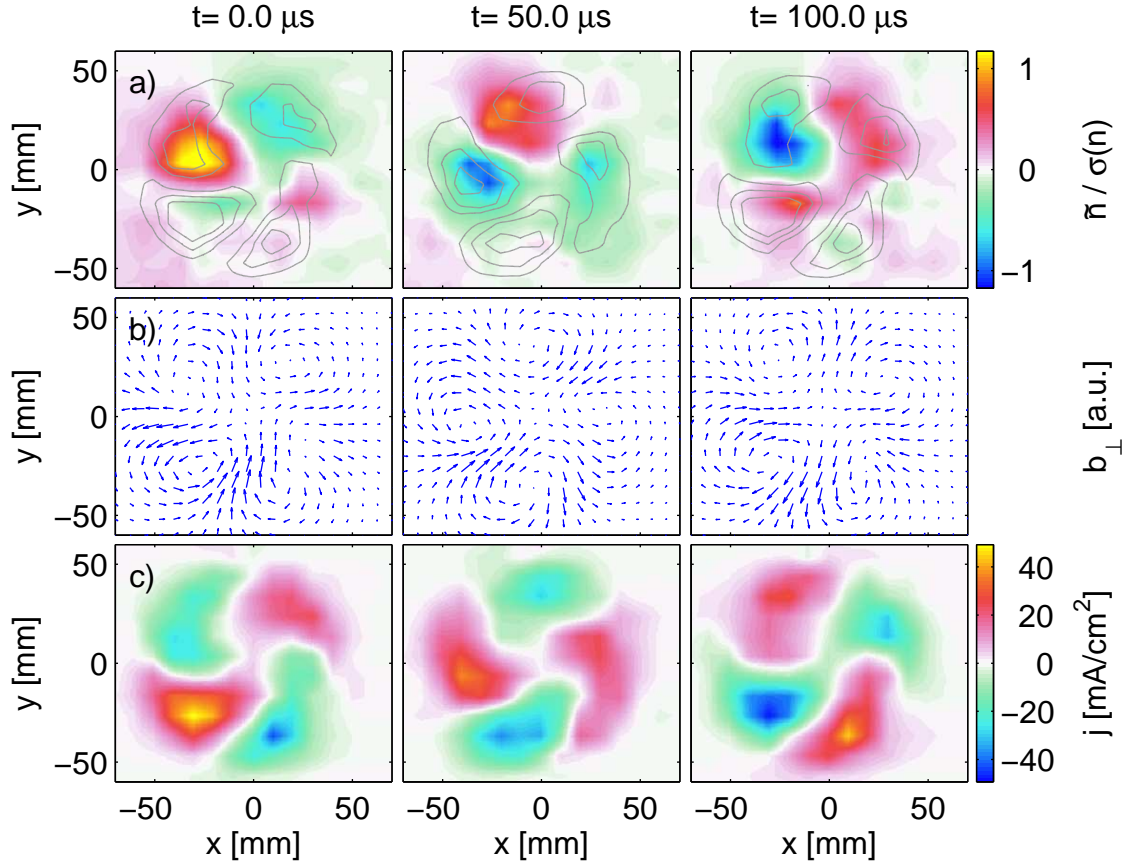


Figure 5.3: Drift wave mode  $m = 2$  in the azimuthal plane in the same representation as in Fig. 5.2. The discharge parameters are  $p_{Ar} = 0.21$  Pa and  $B_0 = 75$  mT.

### 5.3 Interaction of drift waves and Alfvén waves

Of major interest in electromagnetic drift waves investigations is the associated transport. Holt et al. [109] have done a detailed experimental analysis including temperature fluctuations. For the collisional drift wave regime and the Alfvén wave regime both a wave-induced plasma transport in the range of the Bohm diffusion [110] was observed. Hence, the investigation of electromagnetic drift waves is of special interest with regard to turbulent transport in fusion experiments [111].

A criterion for the onset of electromagnetic effects in drift dynamics in terms of the plasma- $\beta$  is obtained by comparing the two terms impeding the parallel electron motion in (3.44). For collisionless plasmas, such effects are dominant if  $\beta > m_e/m_i$

Table 5.1:  $m = 2$  and  $m = 3$  drift mode: spatial positions of current and density

mode $m$	$j_{  } [\text{mA/cm}]^2$	$r_j [\text{mm}]$	$r_n [\text{mm}]$	$\Delta r [\text{mm}]$	$\Delta \phi [\text{deg}]$
2	64.8	$35.6 \pm 2.8$	$29.7 \pm 3.5$	$7.7 \pm 4.9$	$7.6 \pm 7.9$
3	44.0	$38.3 \pm 3.0$	$30.5 \pm 3.1$	$6.9 \pm 4.2$	$7.8 \pm 6.4$

[112]. In collisional plasmas, the condition is altered as [53]

$$\beta > \frac{m_e \nu_e}{m_i \omega} \quad (5.1)$$

with the electron collision frequency  $\nu_e$  and the drift wave frequency  $\omega$ . Experimental investigations of electromagnetic drift dynamics with this criterion fulfilled have been presented recently [65]. In VINETA, the right-hand side of (5.1) is typically  $10^{-3}$ , compared to a peak plasma- $\beta$  of  $5 \cdot 10^{-4}$ . Thus, drift waves develop as collisional electrostatic drift waves.

With respect to the involved currents, DWs and AWs are quite similar. The only perpendicular current for both wave types is the ion polarization current (cf. Sec. 3.2.3 and 3.1.2). It is the response to parallel currents and ensures quasineutrality  $\nabla j = 0$ . The two wave types have been discussed using different pictures. While AWs can be described in the MHD picture, DWs exist only in the two-fluid description. Taking the induction term in the parallel force balance (3.44) into account, AWs also exist in the two-fluid description. A general dispersion relation for electromagnetic waves was derived by Mikhailovskii [113, p.141]. In addition to the conventional drift wave branch, it also has an Alfvén branch at higher frequencies. Different from DWs, the growth rate of AWs is found to be negative. However, resistivity gradients may lead to destabilization of the Alfvén branch [114]. A further source of destabilization is a stationary parallel plasma current [115]. Here, a parallel electric field builds up due to the finite resistivity of the plasma. This enters the electron parallel force balance and impedes electron motion in parallel direction. It is therefore equivalent to a friction force, which leads to a phase shift between potential and density and, consequently, to an amplification of the wave. An experimental observation of this effect has been reported in a cylindrical arcjet discharge [116, 117]. The excited waves were identified as Alfvén wave by dispersion measurements. The mode structure of the observed unstable AWs was a  $m = 1$  mode, rotating in electron diamagnetic drift direction [118]. The destabilization of AWs in response to a parallel plasma current has also been reported in other experiments [119].

### 5.3.1 Observation of drift-Alfvén wave interaction

Self-consistent electromagnetic DWs or drift-Alfvén waves (DAWs) are observed only if the  $\beta$ -criterion (5.1) is satisfied. This is the case in the experiments reported by Morales et al. [120]. Destabilization of the wave has been accomplished by steep density and temperature gradients in elongated filaments of a density depletion in an elsewhere homogeneous plasma. Electromagnetic DWs occurred as coherent modes in the low-frequency range  $\omega < \omega_{ci}$  and show a broad spectrum of higher frequencies, the latter being interpreted as Alfvénic turbulence. In the work of Sun et al. [65, 121], the  $\beta$ -criterion is met as well. Here the electromagnetic DWs are destabilized with an axial electric field in the intermediate region of a two-chamber helicon-discharge [122]. The wave properties are found to be in good agreement with a two-fluid model.

A different situation is found in the VINETA plasma. As shown in Sec. 5.2, the parallel electron dynamics is governed by friction and not by induction and the  $\beta$ -criterion is not met. To overcome this limitation, a similar approach as proposed by Tang et al. [118, 123] has been chosen. In that study, a constant parallel plasma current is used to destabilize an AW. The AW interacts with coexistent electrostatic drift waves if the condition

$$\omega^* = k_{\parallel} v_A \quad (5.2)$$

is met. In Tang's work the AW was primarily influenced while the DWs remained almost unaffected. This situation is reconsidered here with special attention to actively influencing properties of the DW.

To investigate the interaction between AWs and DWs in VINETA, an AW is excited by an external periodic drive (cf. Sec. 2.5) in a plasma where a coherent drift mode propagates. The AW frequency is chosen to be in the vicinity of the DW frequency to match the condition (5.2). Figs. 5.4 (a) and (b) illustrate the interaction of a  $m = 3$  drift mode (frequency  $f = 11.3$  kHz) with an AW. In the space-time diagram (a), the drift mode occurs as a tilted stripe pattern with three periods in azimuthal direction. The frequency-mode number spectrum [Fig. 5.4 (b)] peaks at mode number  $m = 3$ . Further components with mode numbers  $m \geq 4$  are observed at frequencies  $f \geq 12$  kHz. Switching the AW excitation on ( $f_{\text{AW}} = 11.78$  kHz) leads to the occurrence of an additional  $m = 4$  mode [Fig. 5.4 (d)]. The  $m = 3$  mode is slightly reduced in amplitude. In the space-time diagram [Fig. 5.4 (c)], the two modes result in a beat wave structure with occasional phase defects (green circles). Further, an increase of small components at larger mode numbers  $m > 4$  is observed while the AW-drive is switched on. After switching the AW-drive off [Fig. 5.4 (e) and (f)], the  $m = 3$  mode is reestablished and the component at  $m = 4$  vanishes. This situation is even more coherent than the initial one. The strong coherent mode is accompanied in the

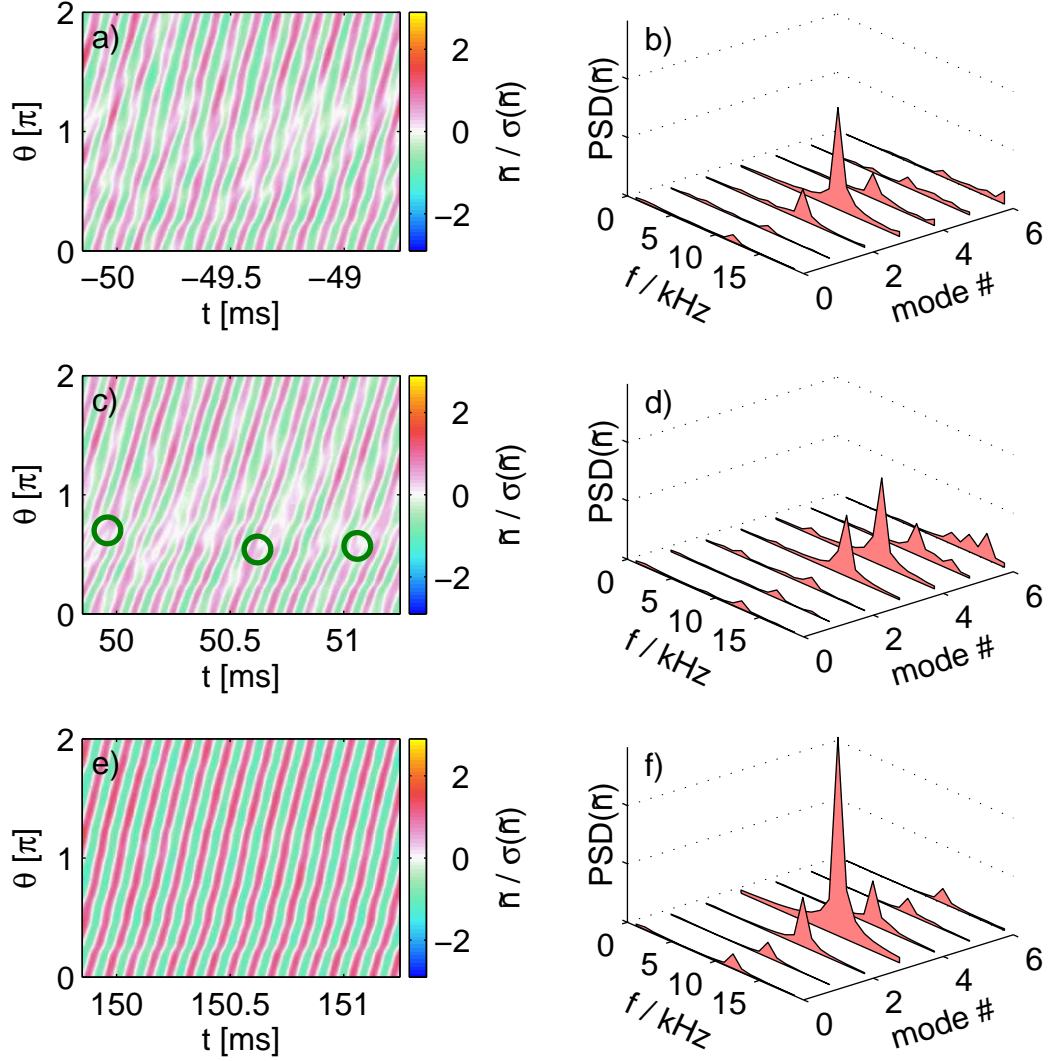


Figure 5.4: Drift-Alfvén wave coupling experiment. The spatio-temporal diagram of the fluctuating density (a, c, e) is complemented by the 2D-frequency-modenumbers spectrum (b, d, f). The Alfvén wave excitation is switched on at 0 ms and operated for 100 ms. The three shown time instants correspond to a situation before, during, and after launching the Alfvén wave. The discharge parameters are  $B_0 = 85$  mT and  $p = 0.39$  Pa, the wave excitation frequency is  $f = 11.78$  kHz. The red circles in (c) indicate phase defects.

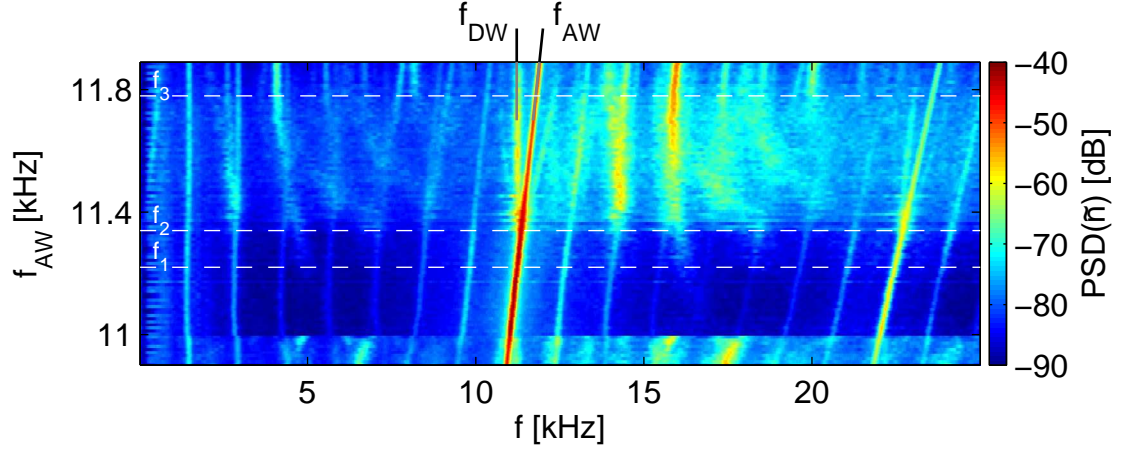


Figure 5.5: Spectrogram of drift wave - Alfvén wave coupling experiment. The power spectral density of the density fluctuations is shown for different frequencies of the excited Alfvén wave. The indicated excitation frequencies  $f_1 \dots f_3$  are analyzed in detail in Fig. 5.6, where  $f_1$  corresponds to  $f_{AW} = f_{DW}$ .

spectrum by components at  $m \neq 3$ . These are numerical artifacts due to spectral leakage. The measurement was repeated 100 times with AW excitation frequencies in the range  $f_{AW} = 10.9 \dots 11.9$  kHz, close to the DW frequency of  $f_{DW} = 11.3$  kHz. It is found that the initial state of the DW is indifferent from discharge to discharge. However, after switching on and off the AW, a coherent  $m = 3$  mode as shown in Fig. 5.4 (e) and (f) is always observed.

The power spectral density of the density fluctuations for each AW frequency in the range  $f_{AW} = 10.9 \dots 11.9$  kHz is shown in Fig. 5.5. If the AW and DW frequencies are equal  $f_{DW} = f_{AW} = 11.3$  kHz (indicated by the line  $f_1$ ), the power spectral density essentially shows the combined frequency peak of the two waves and the first harmonic at 22.6 kHz. A weak frequency component is observed at  $1.41$  kHz  $= f_{DW}/8$ , up to three higher harmonics are clearly seen. To either side of the main frequency peak, spectral components are found with a frequency shift  $\Delta f = \pm 1.41$  kHz, equal to the observed low-frequency component. These side bands also occur to either sides of the second harmonic of the main frequency peak.

There are two separated frequency intervals:

- (A) DWs and AWs coexist at large frequency mismatch.
- (B) At small frequency mismatch ( $f_{AW} = 11.00 \dots 11.37$  kHz) frequency pulling is observed, i.e., DWs and AWs have the same frequencies and are shifted according

by the AW driver frequency.

The frequency-mode number spectral analysis reveals a coherent  $m = 3$  mode at all driver frequencies, cf. Fig. 5.6 (b). The frequency pulling range  $\Delta f = f_{\text{DW}} - 0.30 \dots f_{\text{DW}} + 0.07 \text{ kHz}$  is asymmetric as observed for DW synchronization using a mode-selective control scheme [124]. Outside the frequency pulling range, the situation changes. Here, AWs and DWs can be distinguished as two peaks in the frequency spectrum. The amplitude of the AW is stronger than the DW amplitude. The background noise is significantly higher, which can be attributed to weak turbulence. At a larger positive frequency mismatch, a new peak occurs in the frequency spectrum at about 16 kHz. Its frequency depends on the driver frequency, the slope equals the slope the driver frequency in Fig. 5.5.

The mode numbers related to all described frequency components can be inferred from Fig. 5.6. Without frequency mismatch, the frequency spectra for an unperturbed DW and for a DW with simultaneously launched AW are identical [Fig. 5.6 (a)]. The main component at  $f = 11.30 \text{ kHz}$  and the side bands at  $\pm 1.41 \text{ kHz}$  are clearly seen. In the corresponding frequency-mode number spectrum in Fig. 5.6 (b) the low frequency components at  $f_{\text{DW}}/8 = 1.41 \text{ kHz}$  correspond  $m = -1$ , a rotation into the opposite direction of the main component with  $m = 3$ . For a frequency mismatch  $\Delta f = +0.04 \text{ kHz}$  the frequency spectrum shows a shift of all components by  $\Delta f$  [Fig. 5.6 (c)]. The amplitudes as well as the mode structures remain essentially unchanged [Fig. 5.6 (d)]. Outside the pulling range at a mismatch of  $\Delta f = 0.48 \text{ kHz}$  the two frequency components of the DW and the AW are clearly separated [Fig. 5.6 (e)]. In comparison to the unperturbed case the amplitude of the DW is reduced by -25 dB. The small change in the DW frequency is related to slight variations in the discharge parameters. The frequency components around 16 kHz have mode numbers  $m = 6 \dots 8$ , they are the higher harmonics in  $k$ -space of the dominant mode numbers  $m = 3, 4$  [Fig. 5.6 (f)].

Both DWs and AWs cause fluctuating magnetic wave fields. Fig. 5.7 shows three radial scans of the magnetic fluctuation amplitude  $b_{\perp}(r)$  for DWs (1) and AWs (2) individually and DW-AW-coupling (3). In case (2) the AW is driven clearly separated from the DW-frequency range at  $f_{\text{AW}} = 20 \text{ kHz}$ , in case (3) at the same frequency as the DW. In case (2) and (3) the magnetic fluctuation amplitudes are shown at the frequencies of the AWs, in case (1) at the frequency of the DW. The discharge parameters were always the same as in the interaction experiment (Fig. 5.5).

The radial fluctuation profile for AWs is symmetric with a maximum in the plasma center. The amplitude decreases to both sides until a minimum is reached at  $r = \pm 28 \text{ mm}$ . After a second maximum at  $r = \pm 41 \text{ mm}$  the fluctuating magnetic field finally vanishes outside the plasma. This shape is a radial cross-section of the

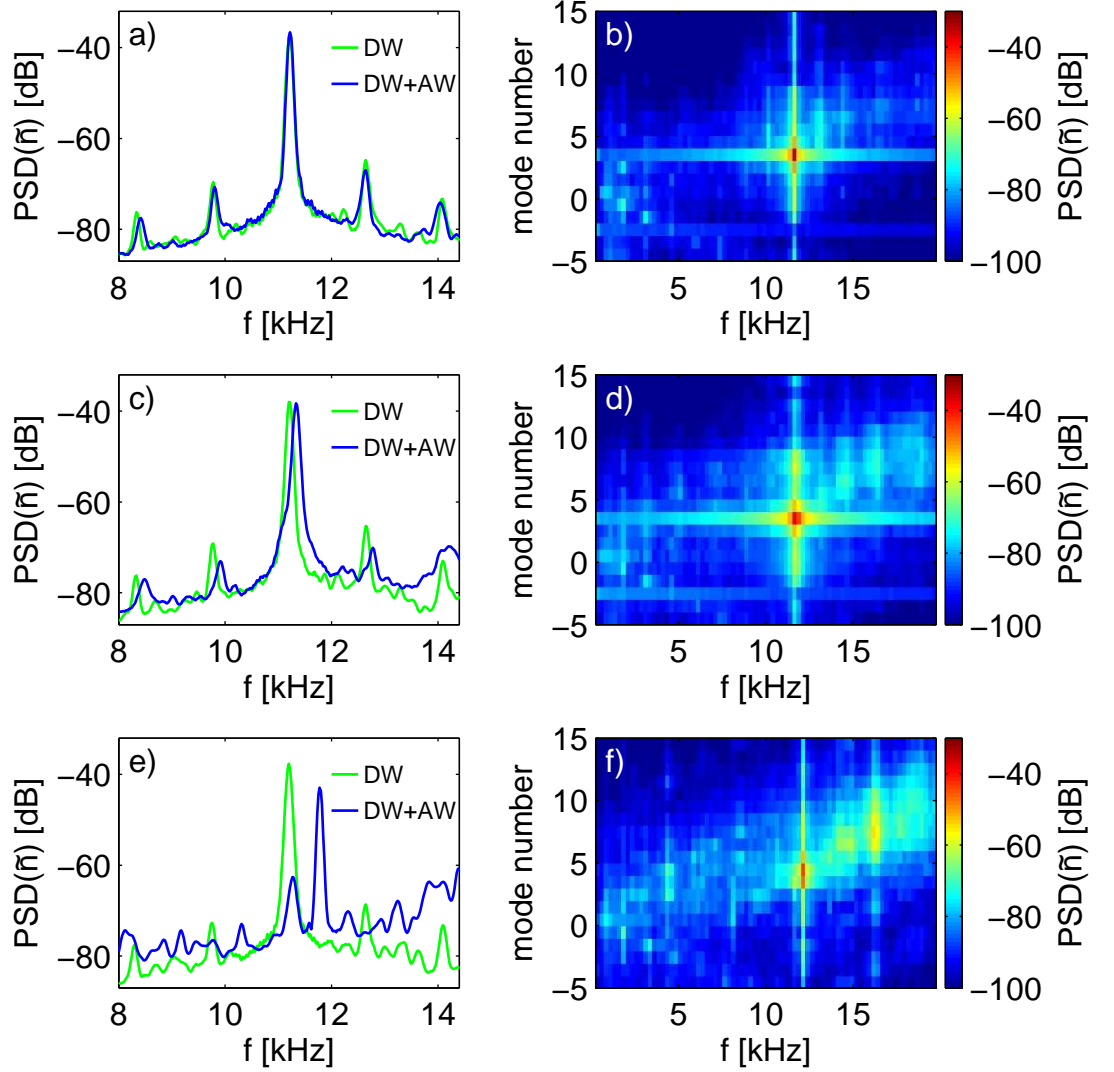


Figure 5.6: Power spectral density of plasma density fluctuations of DWs and AWs. The frequency spectra (a), (c), and (e) are complemented by the frequency-modenumbers spectra (b), (d), and (f). In (a, b) the frequency of the externally driven Alfvén wave matches the drift wave frequency ( $f_1$  in Fig. 5.5), in (c, d), it is slightly shifted in the frequency pulling range ( $f_2$  in Fig. 5.5), and in (e, f) the frequency mismatch is higher with no locking of the waves ( $f_3$  in Fig. 5.5).

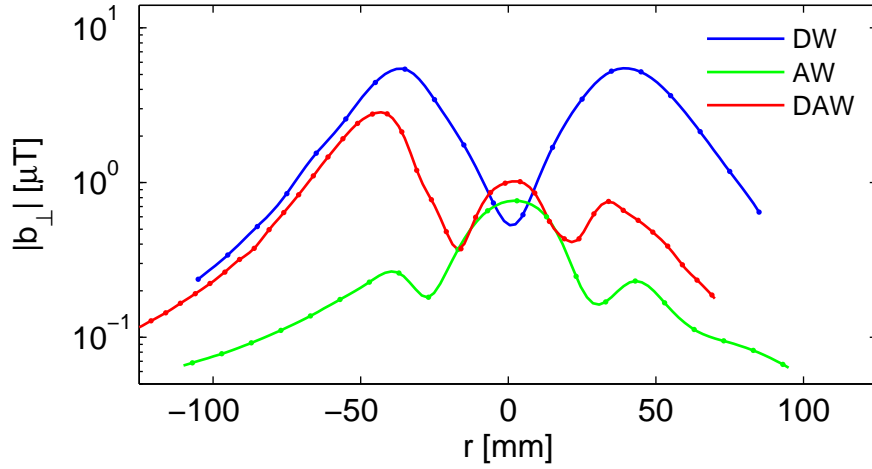


Figure 5.7: Radial magnetic fluctuation amplitude for a drift wave ( $f_{\text{DW}} = 11.7$  kHz), an Alfvén wave ( $f_{\text{AW}} = 20.0$  kHz), and a coupled drift-Alfvén wave ( $f_{\text{DAW}} = 11.3$  kHz). The components of the two wave types have been separated by their frequency.

$m = 1$  mode already shown in Fig. 4.14, which is also predicted by the MHD-model in Sec. 3.1.6. The minima of the fluctuating magnetic field correspond to the radial locations of the parallel current filaments in the center of the perpendicular magnetic field curls. For DWs, the radial fluctuation profile  $|b_{\perp}(r)|$  is a radial cross-section of the measurement shown in Fig. 5.2. Two maxima are found in the maximum density gradient region at  $r = \pm 38$  mm. In the center, the fluctuation amplitude decreases. The slope of the fluctuation profile at the edge is larger for DWs than for AWs. The reason could be the larger mode number of the DW ( $m = 3$ ) compared to the AW ( $m = 1$ ) and thus the increased spatial decay of the associated multi-pole fields. The magnetic fluctuation amplitude of DW is larger than that of AWs since the associated parallel currents are larger for DWs (cf. Fig. 5.2 and Fig. 4.17). In case of interacting DWs and AWs, the radial fluctuation profile has a three-hump structure. The obvious asymmetry is a perturbation of the plasma by the  $\dot{B}$ -probe. The shape of  $|b_{\perp}|(r)$  can be simply interpreted as a superposition of the magnetic fluctuation profiles of DWs and AWs. The combined profile is dominated by the stronger DWs near the plasma edge and by the centrally peaked AWs in the plasma center. In the intermediate range with similar fluctuation amplitudes, the resulting field is not a sum of the individual waves  $|b_{\perp}| \neq |\vec{b}_{\text{AW}}| + |\vec{b}_{\text{DW}}|$ , which might be due to phase mixing of the two waves.

To compare electrostatic with the magnetic measurements, an experiment similar to the interaction experiment in Fig. 5.6 was done in a wider frequency range 5...30 kHz. The magnetic field fluctuations  $b(t)$  and the density fluctuations

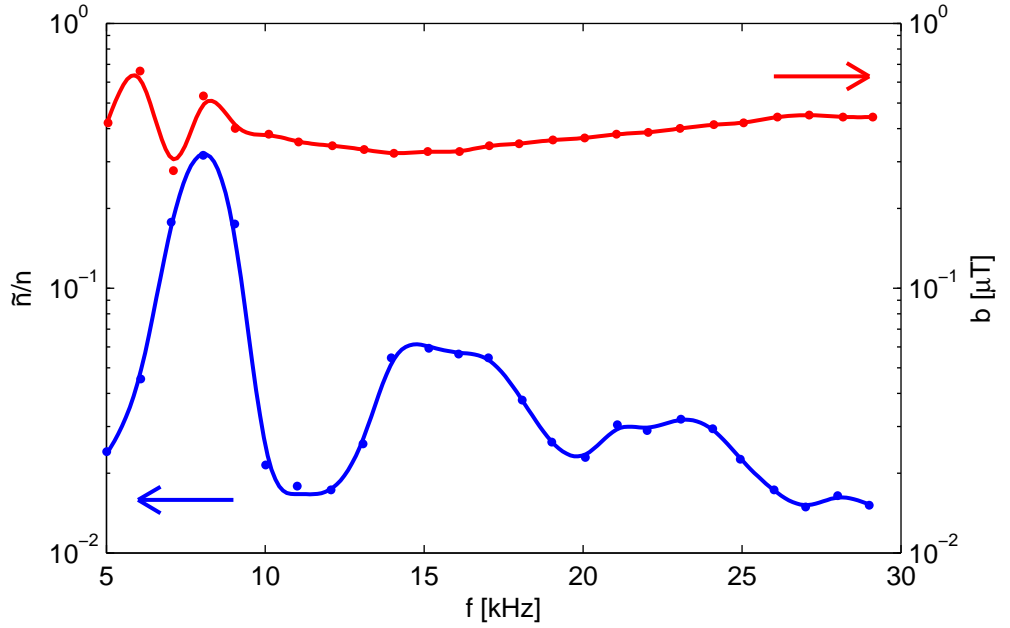


Figure 5.8: Density fluctuations associated with Alfvén waves. The fluctuating magnetic field amplitude  $b$  (red curve) and the density fluctuation amplitude  $\tilde{n}/n_0$  (blue curve) are simultaneously recorded.

$\tilde{n}(t)/n$  were simultaneously recorded at fixed positions in the density gradient region (Fig. 5.8), 1900 mm downstream from the AW driver antenna. Since the magnetic fluctuation amplitude is almost constant for all frequencies, the AW can be considered to have a constant amplitude. Remaining variations can be attributed to a change in the damping length and slight variations of the excitation amplitude, both frequency-dependent effects. The density fluctuations  $\tilde{n}/n$  vary on a wide range from 1.5 % ... 30 %. Frequency ranges of large fluctuations are followed by ranges of small fluctuations. The highest amplitudes are observed below 10 kHz, the DW range in VINETA. The observed dependence of the density fluctuations on the driver frequency is not correlated with the magnetic field fluctuation dependence.

### 5.3.2 Interpretation of the observations

Our experiments yield a rather complex picture of density and magnetic field fluctuations at different frequencies and wave modes. In particular, the interaction of two wave types is observed as frequency pulling of the DW by the AW (cf. Fig. 5.5). The key question is which mechanism leads to the interaction.

Density fluctuations at the AW frequency are observed in the interaction experiment. In the Hall-MHD model of AWs no density fluctuations occur. In the two-fluid description of AWs the wave electric field causes  $E \times B$  convection which in the presence of density gradients leads to density fluctuations [107]. A estimate of the electric field at typical plasma parameters in VINETA (Sec.3.1.5) yields  $\tilde{E}_\perp \approx 0.3 \text{ V/m}$ . For drift waves, the perpendicular electric field can be estimated to be

$$\tilde{E}_\perp \approx \frac{\tilde{\phi}}{L_\perp} \approx \phi_0 \frac{\tilde{n}}{n} \kappa_n = 30 \text{ V/m} . \quad (5.3)$$

The plasma potential  $\phi_0$  is assumed to be 10 V, the fluctuation degree  $\tilde{n}/n$  to be 10 % and  $\kappa_n = 30$  (cf. Fig.3.1). We find that the perpendicular electric field of AWs is two orders of magnitude smaller than that of DWs and density fluctuations  $\ll 1\%$  are expected. This is clearly supported by measurement. While the AW has an  $m = 1$  mode structure, the density fluctuation at the AW driver frequency corresponds to an  $m = 3$  mode, cf. Fig.5.6 (b) and (d). Hence, the fluctuating density at  $f_{\text{AW}}$  cannot be attributed directly to the externally driven AW.

Common to both wave types is the parallel current, which was experimentally observed for AWs in Sec.4.2 and for DWs in Sec.5.2. Magnetic field fluctuations are associated with these currents. The  $|b_\perp|(r)$  in Fig.5.7 indicates that the magnetic field fluctuations of the unstable DWs and the driven AW are just superimposed. This fact and the different mode structures lead to the conclusion that both wave types exist independent from each other, even in the case of frequency pulling.

The interaction of the two wave types occurs most likely via their parallel currents. Launching an AW generates  $j_z^{\text{AW}}(t)$  at radial locations that overlap with the DW current locations in the density gradient region. The finite parallel resistivity results in an additional fluctuating parallel electric field and must be taken into account in the parallel force balance for the electrons (3.44). The AW thus impedes the electron motion, leading to a shift between the fluctuating potential and density and, consequently, to an increased growth rate of the DW. This mechanism is similar to the destabilization of DWs and AWs by drawing a constant axial current through the plasma [115, 118]. The main difference in our experiment is the use of an alternating plasma current driven by the AW antenna at the frequency  $f_{\text{AW}}$ . This limits the destabilization of DWs to the AW excitation frequency  $f_{\text{DW}} = f_{\text{AW}}$ . The introduced axial currents are quite small. The measured value for DWs is  $j_\parallel \approx 65 \text{ mA/cm}^2$ , the additional introduced current density of AWs is  $j_\parallel \approx 9.0 \text{ mA/cm}^2$ , changing the force balance for the electrons is only slightly. The condition (5.1) for the occurrence of electromagnetic drift waves, on the other hand, remains unchanged for interacting DW and AW since the electromagnetic force term in (3.44) is negligible. In this linear picture, the influence of an externally driven AW on DWs is limited to a small

change in the growth rate of the existing DW.

If the linear DW dispersion relation predicts positive growth rates for more than one DW mode, they will not exist as superposition. Rather, the modes compete for the available free energy that stems from the density gradient. As shown in Fig. 5.4, the drift waves there seem to be in an indifferent state with a dominant  $m = 3$  mode and several smaller modes and frequency components. After switching the AW-excitation on and off there is only a coherent  $m = 3$  mode. If an AW is launched at a frequency close to that of the DW, the DW frequency might be shifted by a hysteresis in the frequency pulling that establishes the new status. Note that the mode number of the launched AW  $m = 1$  does not match the mode number of the frequency locked DW  $m = 3$  (cf. Fig. 4.15 and Fig. 5.6). In the excitation spectrum in Fig. 1.2 the modulation level of density fluctuation has a strong frequency dependence for an AW with an almost equal amplitude in the observed range. These two experimental findings might be considered as indicator that the observed density fluctuations are not directly generated by the AW. Rather, they could be associated with a DW destabilized at the AW frequency.

To conclude, the above described experiments suggest that DWs and AWs do not interact via the induction term in the parallel force balance for electrons, as it would be the case for electromagnetic drift waves, but via the electric field associated to the parallel currents. Since the influence of these additional currents on the drift dynamics is small, linear wave interaction is most likely.

# Chapter 6

## Summary and conclusions

In VINETA, the most frequently observed waves in the low-frequency range below the ion-cyclotron frequency are (stable) Alfvén waves and (unstable) drift waves. Hitherto, Alfvén waves were mostly investigated by measuring the fluctuating magnetic field, drift waves by measuring the fluctuating plasma density. A more integral approach is pursued in the present work. Both wave types drive parallel conduction currents. These currents are measured with high resolution in both space and time. This is done with a magnetic sensor as  $\dot{B}$ -probe, designed to measure low-frequency  $f = 100 \text{ Hz} \dots 2 \text{ MHz}$  magnetic field fluctuations with high signal-to-noise ratio (e.g. 100 dB for  $b = 1 \mu\text{T}$  at  $f = 1 \text{ kHz}$ ). The sensor simultaneously records the three magnetic fluctuation components  $b_x(t)$ ,  $b_y(t)$ , and  $b_z(t)$ . Any misalignment of the three sensor coils is considered in the calibration. Via Ampère’s law the current pattern is determined from spatially resolved magnetic field fluctuation measurements.

To drive stable Alfvén waves, a magnetic wave excitation system was developed. It is capable of perturbing the ambient magnetic field  $B_0$  up to  $b/B_0 \approx 1\%$ . The driven magnetic waves are well accessible with the magnetic probe even though they are strongly damped. The main findings are:

**i) Wave polarization:** The externally excited magnetic field perturbations are perpendicular to  $B_0$  in  $y$ -direction, which corresponds to linear polarization. The magnetic field fluctuations caused by the launched waves are usually elliptically polarized. The decomposition into one left- and one right-hand circular polarized component reveals different propagation properties of the two wave components. The right-hand polarized (R) wave has the same phase velocity over the entire frequency range below and above the ion cyclotron frequency  $\omega_{ci}$ . The dispersion relation of the left-hand polarized (L) wave shows a bending below  $\omega_{ci}$  with smaller phase velocities than the R-wave. However, the L-wave dispersion does not match

the expected dispersion relation of shear Alfvén waves in the simple Hall-MHD picture. Good agreement is obtained by taking the plasma resistivity into account.

**ii) Currents:** The parallel component of the current density  $j_{\parallel}$  is clearly localized in the plane perpendicular to the wave propagation. This observation agrees well with the experimental studies of Gekelman et al. [125], where a similar diagnostic technique is used. The current system of the externally driven Alfvén waves in VINETA consists mainly of two current filaments with opposite sign, which are identified as modes with  $m = \pm 1$ . This is different from Ref. [125]. The reason is the different excitation system used there [73], which generates a rotational symmetric mode with  $m = 0$ .

**iii) MHD-model for Alfvén waves:** In the low frequency limit  $\omega \ll \omega_{ci}$  the excited waves are Alfvén waves propagating with phase velocity  $v_A$ . The wave propagation is investigated for both L- and R-waves, in particular the parameter dependency on the ambient magnetic field  $B_0$  and on the mass density  $n_0$ . L- and R-waves have the same phase velocity  $v_A$  only in the low-frequency limit, as expected from the Hall-MHD model. For higher frequencies but still well below  $\omega_{ci}$ , different dispersion properties are expected for the two different wave components. This is seen in the experiment, with higher phase velocity for the R-wave than for the L-wave, as also observed in other works [64, 126, 127]. Approaching the ion-cyclotron resonance  $\omega_{ci}$ , the measurements deviate considerably from the Hall-MHD calculations. These deviations are most likely due to the high plasma resistivity with collision frequencies of  $\nu/\omega_{ci} \gtrsim 30$ , which becomes most significant in the short-wavelength limit  $\lambda \rightarrow 0$  close to the resonance point. The introduction of an additional term for the plasma resistivity in the MHD-model gives very good agreement with experiment, in particular the space and time evolution of the parallel current density: The calculated current density has a rotating pattern and is helically twisted, exactly as observed in the experiments.

**iv) Coupling of Alfvén and drift waves:** Electric probes are the standard diagnostic tool to investigate drift waves [103]. Probe arrays give access to the spatio-temporal propagation properties of drift waves [41]. In the present work, drift waves are additionally characterized by their parallel currents. The location of the parallel current filaments matches the maximum of the plasma density fluctuations. This is consistent with the drive of parallel electron currents by parallel pressure gradients. Because of the similarities in the parallel current patterns for both drift- and Alfvén waves, coupling experiments were conducted, similar to the approach proposed by Tang et al. [118]. It is observed that the Alfvén wave dynamics is strongly affected by drift waves, e.g. deviation from the linear dispersion relation. In addition, a nonlinear coupling with drift waves is observed, mostly visible in frequency pulling

---

of the drift wave by the (externally driven) Alfvén wave. This demonstrates the sensitivity of the perpendicular drift wave dynamics to the parallel electrons, the latter altered by the inductively driven currents of the Alfvén wave.

# Appendix A

## Dispersion relation for resistive Alfvén waves

The basic equations for describing Alfvén waves as resistive MHD waves for the frequency range  $0 < \omega \leq 10\omega_{ci}$  are the fluid equation of motion and the generalized Ohms law

$$\rho \frac{\partial \vec{u}}{\partial t} = \vec{j} \times \vec{B} \quad (\text{A.1})$$

$$\vec{E} + \vec{u} \times \vec{B} = \hat{\eta} + \frac{1}{ne} \vec{j} \times \vec{B} . \quad (\text{A.2})$$

This system is closed by the Maxwells curl equations

$$\nabla \times \vec{b} = \mu_0 \vec{j} \quad (\text{A.3})$$

$$\nabla \times \vec{E} = -\frac{\partial \vec{b}}{\partial t} . \quad (\text{A.4})$$

Three terms are neglected from the complete set of equations [128]. Firstly, no temperature effects are taken into account, which leads to vanishing  $\nabla p$  in both equations since  $p = k_B T$ . Secondly, the electron inertia term  $\rho/(en)^2 \cdot \partial \vec{j} / \partial t$  is neglected, leading to the frequency range restriction well below the electron-cyclotron frequency  $\omega \ll \omega_{ce}$ . Finally, quasineutrality is assumed  $(n_i - n_e)e\vec{E} = 0$ .

This system of four coupled linear differential equations can be solved by the plane wave ansatz

$$b_x = b_{x0} e^{i(\vec{k} \cdot \vec{x} - \omega t)} , \quad (\text{A.5})$$

with  $b_x$  being replacable by any of the components of  $\vec{E}$ ,  $\vec{u}$  or  $\vec{j}$ . Inserting this into

---

(A.1) yields

$$\begin{aligned} -i\omega\rho u_x &= j_y B_0 & E_x + u_y B_0 &= \eta j_x + (1/ne)j_y B_0 \\ i\omega\rho u_y &= j_x B_0 & E_y - u_x B_0 &= \eta j_y - (1/ne)j_x B_0 \\ u_z &= 0 & E_z &= 0 \end{aligned} \quad . \quad (\text{A.6})$$

The fluctuating magnetic field components are written in lower case. All components of the electric field and the current density are fluctuating quantities.  $B_0$  is the ambient magnetic field, which is aligned along the  $z$ -coordinate without loss of generality. By combining the first two equations of each block, the components  $u_x$  and  $u_y$  of the velocity can be eliminated. After some manipulations, this leads to

$$\begin{aligned} j_y - \frac{v_A^2}{\omega_{ci}} j_x - \frac{E_y}{\mu_0} &= 0 \\ j_x + \frac{v_A^2}{\omega_{ci}} j_y - \frac{E_x}{\mu_0} &= 0 \end{aligned} \quad . \quad (\text{A.7})$$

Here, the Alfvén velocity is introduced as  $v_A = B_0/\sqrt{\mu_0\rho}$ . The Maxwell curl equations can be used to express  $j_x$  and  $j_y$  in terms of the electric field. Using the plane wave ansatz yields

$$\begin{aligned} \mu_0 j_x &= i(k_y b_z - k_z b_y) & -k_z E_y &= \omega b_x \\ \mu_0 j_y &= i(k_z b_x - k_x b_z) & k_z E_x &= \omega b_y \\ \mu_0 j_z &= i(k_x b_y - k_y b_x) & k_x E_y - k_y E_x &= \omega b_z \end{aligned} \quad . \quad (\text{A.8})$$

The magnetic field can be eliminated from these equations, resulting in

$$\left(\frac{\eta}{\mu_0} - \frac{v_A^2}{i\omega}\right) j_x = \frac{i}{\omega\mu_0} (k_x k_y E_y - k_y^2 E_x - k_z^2 E_x) \quad (\text{A.9})$$

$$\left(\frac{\eta}{\mu_0} - \frac{v_A^2}{i\omega}\right) j_y = \frac{i}{\omega\mu_0} (k_x k_y E_x - k_x^2 E_y - k_z^2 E_y) \quad . \quad (\text{A.10})$$

This is the relation between the current density and the electric field, needed for (A.7). Replacing  $j$  yields

$$\begin{aligned} \left(\frac{\eta}{\mu_0} - \frac{v_A^2}{i\omega}\right) (k_x k_y E_x - (k_x^2 + k_z^2) E_y) - \frac{v_A^2}{\omega_{ci}} (k_x k_y E_y - (k_y^2 + k_z^2) E_x) - \frac{\omega}{i} E_y &= 0 \\ \left(\frac{\eta}{\mu_0} - \frac{v_A^2}{i\omega}\right) (k_x k_y E_y - (k_y^2 + k_z^2) E_x) + \frac{v_A^2}{\omega_{ci}} (k_x k_y E_x - (k_x^2 + k_z^2) E_y) - \frac{\omega}{i} E_x &= 0 \end{aligned} \quad . \quad (\text{A.11})$$

At this point, a simplification is achieved by introducing the normalized quantities [18]

$$\alpha = \frac{v_A k}{\omega_{ci}} \quad f = \frac{\omega}{\omega_{ci}} \quad R = \frac{\eta \omega_{ci}}{\mu_0 v_A^2} \quad . \quad (\text{A.12})$$

The normalization for the wave vector is valid for each component, in particular  $\alpha_x = v_A k_x / \omega_{ci}$ . Both Eqs. (A.11) can be brought into a form  $(E_x/E_y) = \dots$ . They read to be

$$\frac{E_x}{E_y} = \frac{\alpha_x \alpha_y + i[ f(\alpha_x^2 + \alpha_z^2) - Rf\alpha_x \alpha_y ]}{\alpha_y^2 + \alpha_z^2 - f^2 + i[ f\alpha_y \alpha_x - Rf(\alpha_y^2 + \alpha_z^2) ]} \quad (\text{A.13})$$

$$\frac{E_y}{E_x} = \frac{\alpha_x \alpha_y + i[ -f(\alpha_x^2 + \alpha_z^2) - Rf\alpha_x \alpha_y ]}{\alpha_x^2 + \alpha_z^2 - f^2 + i[ -f\alpha_y \alpha_x - Rf(\alpha_x^2 + \alpha_z^2) ]} \quad (\text{A.14})$$

For the special case of propagation parallel to the magnetic field ( $\alpha_x = 0, \alpha_y = 0$ ) and no resistivity ( $R = 0$ ), the ratio of the perpendicular electric field components simplifies to

$$\frac{E_x}{E_y} = i \frac{\alpha_z^2 f}{\alpha_z^2 - f^2} \quad (\text{A.15})$$

In the general case of propagation along and across the field, the elimination of  $E_x/E_y$  leads to a condition for  $\omega$  and  $\vec{k}$  with no fluctuating quantities left. After some lengthy but straightforward manipulations, the result is

$$f^4 + f^3 i R (\alpha^2 + \alpha_z^2) - f^2 (\alpha^2 \alpha_z^2 + \alpha^2 + \alpha_z^2 + R^2 \alpha^2 \alpha_z^2) - f \cdot 2i R \alpha^2 \alpha_z^2 + \alpha^2 \alpha_z^2 = 0 \quad (\text{A.16})$$

If satisfied, the plane wave ansatz (A.5) is a solution of the initial equation system. Such relationship  $f(\omega, \vec{k}) = 0$  is referred to as dispersion relation.

# Bibliography

- [1] P. A. Davidson. *An Introduction to Magnetohydrodynamics*. Cambridge Univ. Press, 2001.
- [2] A. Sommerfeld. *Mechanik der deformierbaren Medien*. Verlag Harry Deutsch, 1992.
- [3] H. Saleem and Q. Haque. Role of quasineutrality in drift waves. *Physics of Plasmas*, 8(1):368–369, 2001.
- [4] O. Engvold. The fine structure of prominences. I: Observations — H-Alpha filtergrams. *Solar Physics*, 49(2):283–295, 1976.
- [5] G. A. Gary and R. L. Moore. Eruption of a multiple-turn helical magnetic flux tube in a large flare: Evidence for external and internal reconnection that fits the breakout model of solar magnetic eruptions. *Astrophysical Journal*, 611(1):545–556, 2004.
- [6] R. Michard. The sun and its corona. *Science Progrès Découverte*, no.3428: 33–41, 1970.
- [7] O. G. Badalyan and V. N. Obridko. To the problem of solar coronal heating. *Astronomy Letters. A Journal of Astronomy and Space Astrophysics*, 33(3): 182–191, 2007.
- [8] B. H. Mauk and C. E. McIlwain. Magnetic field-aligned electrodynamics of Alfvén ion-cyclotron waves. *Journal of Geophysical Research — Space Physics*, 98(A11):19435–19441, 1993.
- [9] B. H. Mauk and R. L. McPherron. An experimental test of the electromagnetic ion-cyclotron instability within the earths magnetosphere. *Physics of Fluids*, 23(10):2111–2127, 1980.
- [10] H. Alfvén. Existence of electromagnetic-hydrodynamic waves. *Nature*, 150: 405–406, 1942.

- [11] W. Gekelman. Review of laboratory experiments on Alfvén waves and their relationship to space observations. *Journal of Geophysical Research — Space Physics*, 104(A7):14417–14435, 1999.
- [12] Y. I. Kolesnichenko, S. Yamamoto, K. Yamazaki, V. V. Lutsenko, N. Nakajima, Y. Narushima, K. Toi, and Y. V. Yakovenko. Interplay of energetic ions and Alfvén modes in helical plasmas. *Physics of Plasmas*, 11(1):158–170, 2004.
- [13] D. Sundkvist and S. D. Bale. Characteristic parameters of drift vortices coupled to Alfvén waves in an inhomogeneous space plasma. *Physical Review Letters*, 101(6), 2008.
- [14] B. D. Scott. Three-dimensional computation of drift Alfvén turbulence. *Plasma Physics and Controlled Fusion*, 39(10):1635–1668, October 1997.
- [15] B. D. Scott. The character of transport caused by  $E \times B$  drift turbulence. *Physics of Plasmas*, 10(4):963–976, April 2003.
- [16] B. D. Scott. Edge turbulence and its interaction with the equilibrium. *Contributions to Plasma Physics*, 46(7-9):714–725, 2006.
- [17] B. D. Scott. Computation of electromagnetic turbulence and anomalous transport mechanisms in tokamak plasmas. *Plasma Physics and Controlled Fusion*, 45:A385–A398, December 2003.
- [18] Neil F. Cramer. *The Physics of Alfvén Waves*. WILEY-VCH Verlag Berlin GmbH, 2001.
- [19] W. Gekelman, S. Vincena, and D. Leneman. Experimental observations of shear Alfvén waves generated by narrow current channels. *Plasma Physics and Controlled Fusion*, 39:A101–A112, 1997.
- [20] C. Watts and J. Hanna. Alfvén wave propagation in a partially ionized plasma. *Physics of Plasmas*, 11(4):1358–1365, April 2004.
- [21] R. H. Huddleston and S. L. Leonhard. *Plasma Diagnostic Techniques*, chapter 3: Magnetic probes (R. H. Lovberg). Academic Press, 1965.
- [22] A. Piel. *Einführung in die Plasmaphysik*. Institut für Experimentalphysik, Christian-Albrechts-Universität zu Kiel, 1999.
- [23] M.-B. Kallenrode. *Space Physics*. Springer-Verlag Berlin, 1998.

- 
- [24] N. Cornilieu-Wehrlin, H. Alleyne, K. Yearby, B. D. de Vaux, A. Meyer, O. Santolik, M. Parrot, G. Belmont, L. Rezeau, O. Le Contel, A. Roux, D. Attie, P. Robert, V. Bouzid, D. Herment, and J. Cao. The STAFF-DWP wave instrument on the DSP equatorial spacecraft: description and first results. *Annales Geophysicae*, 23(8):2785–2801, 2005.
- [25] A. Stark. *Ion dynamics in magnetized plasmas*. PhD thesis, Ernst-Moritz-Arndt-Universität Greifswald, 2006.
- [26] R. W. Boswell. Very efficient plasma generation by whistler waves near the lower hybrid frequency. *Plasma Physics and Controlled Fusion*, 26(10):1147–1162, 1984.
- [27] F. F. Chen and R. W. Boswell. Helicons — The past decade. *IEEE Transactions on Plasma Science*, 25(6):1245–1257, 1997.
- [28] R. W. Boswell and F. F. Chen. Helicons — The early years. *IEEE Transactions on Plasma Science*, 25(6):1229–1244, 1997.
- [29] F. F. Chen. Plasma ionization by helicon waves. *Plasma Physics and Controlled Fusion*, 33(4):339–364, 1991.
- [30] V. F. Virko, K. P. Shamrai, Y. V. Virko, and G. S. Kirichenko. Wave phenomena, hot electrons, and enhanced plasma production in a helicon discharge in a converging magnetic field. *Physics of Plasmas*, 11(8):3888–3897, August 2004.
- [31] F. F. Chen, J. D. Evans, and G. R. Tynan. Design and performance of distributed helicon sources. *Plasma Sources Science and Technology*, 10(2):236–249, 2001.
- [32] J. Hanna and C. Watts. Alfvén wave propagation in a helicon plasma. *Physics of Plasmas*, 8(9):4251–4254, September 2001.
- [33] A. J. Perry, D. Vender, and R. W. Boswell. The application of the helicon source to plasma processing. *Journal of Vacuum Science and Technology B*, 9(2):310–317, 1991.
- [34] J. P. Squire, F. R. Chang-Diaz, T. W. Glover, V. T. Jacobson, G. E. McCaskill, D. S. Winter, F. W. Baity, M. D. Carter, and R. H. Goulding. High power light gas helicon plasma source for VASIMR. *Thin Solid Films*, 506:579–582, 2006.
- [35] A. V. Arefiev and B. N. Breizman. Theoretical components of the VASIMR plasma propulsion concept. *Physics of Plasmas*, 11(5):2942–2949, 2004.

- [36] K. P. Shamrai and V. B. Taranov. Resonances and anti-resonances of a plasma-column in a helicon plasma source. *Physics Letters A*, 204(2):139–145, 1995.
- [37] M. M. Balkey, R. Boivin, J. L. Kline, and E. Scime. Ion heating and density production in helicon sources near the lower hybrid frequency. *Plasma Sources Science and Technology*, 10(2):284–294, 2001.
- [38] M. Light and F. F. Chen. Helicon wave excitation with helical antennas. *Physics of Plasmas*, 2(4):1084–1093, April 1995.
- [39] C. M. Franck, O. Grulke, and T. Klinger. Mode transitions in helicon discharges. *Physics of Plasmas*, 10(1):323–325, January 2003.
- [40] O. Grulke, A. Stark, T. Windisch, J. Zalach, and T. Klinger. Plasma profiles in a cylindrical helicon discharge with converging magnetic source field. *Contributions to Plasma Physics*, 47(3):183–189, 2007.
- [41] A. Latten, T. Klinger, A. Piel, and T. Pierre. A probe array for the investigation of spatiotemporal structures in drift-wave turbulence. *Review of Scientific Instruments*, 66(5):3254–3262, May 1995.
- [42] C. Schröder, O. Grulke, T. Klinger, and V. Naulin. Drift waves in a high-density cylindrical helicon discharge. *Physics of Plasmas*, 12(4):042103, April 2005.
- [43] T. Windisch, O. Grulke, and T. Klinger. Propagating structures in drift-wave turbulence. *Physica Scripta*, T122:15–18, 2006.
- [44] K. Rahbarnia, E. Holzhauer, N. Mahdizadeh, M. Ramisch, and U. Stroth. Experimental study of the electromagnetic component of drift-wave turbulence. *Plasma Physics and Controlled Fusion*, 50(8):085008, 2008.
- [45] J. Lenz and A. S. Edelstein. Magnetic sensors and their applications. *IEEE Sensors Journal*, 6:631–649, 2006.
- [46] J. Lenz. A review of magnetic sensors. *Proceedings of the IEEE*, 78:973–989, 1990.
- [47] I. Duran, J. Stockel, G. Mank, K. H. Finken, G. Fuchs, and G. V. Oost. Measurements of magnetic field fluctuations using an array of Hall detectors on the TEXTOR tokamak. *Review of Scientific Instruments*, 73(10):3482–3489, October 2002.

- [48] Y. H. Liu, D. A. Maurer, G. A. Navratil, and N. Rivera. High spatial resolution Hall sensor array for edge plasma magnetic field measurements. *Review of Scientific Instruments*, 76(9):093501, September 2005.
- [49] T. L. Francis, O. Mermer, G. Veeraraghavan, and M. Wohlgenannt. Large magnetoresistance at room temperature in semiconducting polymer sandwich devices. *New Journal of Physics*, 6:185, 2004.
- [50] H. M. Mott-Smith and I. Langmuir. The theory of collectors in gaseous discharges. *Physical Review*, 28:727, 1926.
- [51] V. I. Demidov, S. V. Ratynskaia, and K. Rypdal. Electric probes for plasmas: The link between theory and instrument. *Review of Scientific Instruments*, 73(10):3409 – 3439, 2002.
- [52] A. Stark, O. Grulke, and T. Klinger. Propagation and ion dynamics of waves in amplitude modulated helicon plasmas. *Plasma 2005*, 812:141 – 144, 2006.
- [53] C. Schröder. *Experimental Investigations on Drift Waves in a Linear Magnetized Plasma*. PhD thesis, Ernst-Moritz-Arndt-Universität Greifswald, 2004.
- [54] K. U. Riemann. The Bohm criterion and sheath formation. *Journal of Physics D: Applied Physics*, 24:493 – 518, 1991.
- [55] M. J. Druyvesteyn. Der Niedervoltbogen. *Zeitschrift für Physik*, 64:781, 1930.
- [56] V. I. Demidov, S. V. Ratynskaia, R. J. Armstrong, and K. Rypdal. Probe measurements of electron energy distributions in a strongly magnetized low-pressure helium plasma. *Physics of Plasmas*, 6(1):350 – 358, 1999.
- [57] T.H. Stix. *Waves in Plasmas*. AIP, New York, 1992.
- [58] H.-J. Hartfuss. *Mikrowellendiagnostik*. Ernst-Moritz-Arndt-Universität Greifswald, 2005.
- [59] S. M. Kay and S. L. Marple. Spectrum analysis — A modern perspective. *Proceedings of the IEEE*, 69(11):1380 – 1419, 1981.
- [60] R. J. Adrian. Conditional eddies in isotropic turbulence. *Physics of Fluids*, 22(11):2065 – 2070, 1979.
- [61] S. Lundquist. Experimental investigations of magneto-hydrodynamic waves. *Physical Review*, 76(12):1805 – 1809, 1949.
- [62] S. Lundquist. Experimental demonstration of magneto-hydrodynamic waves. *Nature*, 164(4160):145 – 146, 1949.

- [63] B. Lehnert. Magneto-hydrodynamic waves in liquid sodium. *Physical Review*, 94(4):815–824, 1954.
- [64] G. Müller. Experimental study of torsional Alfvén waves in a cylindrical partially ionized magnetoplasma. *Plasma Physics and Controlled Fusion*, 16(9): 813–822, 1974.
- [65] X. Sun, C. Biloiu, and E. Scime. Observation of resistive drift Alfvén waves in a helicon plasma. *Physics of Plasmas*, 12(10):102105, October 2005.
- [66] F. Sahraoui, B. Grison, G. Belmont, J. F. Panis, and L. Rezeau. On wave modes, structures and turbulence in space plasmas: Cluster results. *Turbulence and Nonlinear Processes in Astrophysical Plasmas*, 932:102–110, 2007.
- [67] A. Tjulin, E. A. Lucek, and I. Dandouras. Characterization of waves in the vicinity of an interplanetary directional discontinuity. *Journal of Geophysical Research — Space Physics*, 112(A12), 2007.
- [68] V. M. Chmyrev, S. V. Bilichenko, O. A. Pokhotelov, V. A. Marchenko, V. I. Lazarev, A. V. Streltsov, and L. Stenflo. Alfvén vortices and related phenomena in the ionosphere and the magnetosphere. *Physica Scripta*, 38(6):841–854, 1988.
- [69] S. Vincena and W. Geckelman. Visualizing shear Alfvén wave currents near the ion-cyclotron frequency. *IEEE Transactions on Plasma Science*, 33(2): 552–553, 2005.
- [70] S. Ohsaki and S. M. Mahajan. Hall current and Alfvén wave. *Physics of Plasmas*, 11(3):898–902, 2004.
- [71] S. M. Mahajan and Z. Yoshida. A collisionless self-organizing model for the high-confinement (H-mode) boundary layer. *Physics of Plasmas*, 7(2):635–640, 2000.
- [72] S. M. Mahajan, R. Miklaszewski, K. I. Nikol’skaya, and N. L. Shatashvili. Formation and primary heating of the solar corona: Theory and simulation. *Physics of Plasmas*, 8(4):1340–1357, 2001.
- [73] W. Geckelman, D. Leneman, J. Maggs, and S. Vincena. Experimental observation of Alfvén wave cones. *Physics of Plasmas*, 1:3775–3783, 1994.
- [74] F. F. Cap. *Handbook on Plasma Instabilities*. Academic Press, 1983.
- [75] S. P. Gary. Plasma instabilities in the terrestrial magnetosphere — A review of recent theoretical research. *Physica Scripta*, T18:179–187, 1987.

- [76] D. L. Jassby. Transverse velocity shear instabilities within a magnetically confined plasma. *Physics of Fluids*, 15(9):1590–1604, 1972.
- [77] F. W. Perkins and D. L. Jassby. Velocity shear and low-frequency plasma instabilities. *Physics of Fluids*, 14(1):102–115, 1971.
- [78] H. W. Hendel, T. K. Chu, and P. A. Politzer. Collisional drift waves – identification stabilization and enhanced plasma transport. *PHYSICS OF FLUIDS*, 11(11):2426–2439, 1968.
- [79] W. Horton. Nonlinear drift waves and transport in magnetized plasma. *Physics Reports, Reviews Section of Physics Letters*, 192(1-3):1–177, August 1990.
- [80] W. Horton. Drift waves and transport. *Reviews of Modern Physics*, 71(3):735–778, Apr 1999.
- [81] E. Mazzucato. Small-scale density fluctuations in adiabatic toroidal compressor. *Physical Review Letters*, 36(14):792–794, 1976.
- [82] P.C. Liewer. Measurements of Microturbulence in Tokamaks and Comparisons with Theories of Turbulence and Anomalous Transport. *Nuclear Fusion*, 25(5):543–621, 1985.
- [83] J. Weiland. *Collective Modes in Inhomogeneous Plasma*. Institute of Physics Publishing, Bristol, Philadelphia, 2000.
- [84] N. Dangelo. Low-frequency oscillations in cesium thermionic converters. *Physics of Fluids*, 4(8):1054–1055, 1961.
- [85] N. Dangelo and R. W. Motley. Low-frequency oscillations in a potassium plasma. *Physics of Fluids*, 6(3):422–425, 1963.
- [86] H. Lashinsky. Universal instability in a fully ionized inhomogeneous plasma. *Physical Review Letters*, 12(5):121–123, February 1964. printed.
- [87] R. F. Ellis and E. Mardenmarshall. Comparison of local and nonlocal theories of the collisional drift instability. *Physics of Fluids*, 22(11):2137–2139, 1979.
- [88] S. I. Braginskii. *Reviews of Plasma Physics*, chapter Transport Processes in a Plasma, pages 205–311. Consultants Bureau, New York, 1965.
- [89] Jenko, F. *Numerische Modellierung von stoßfreier Driftwellenturbulenz*. PhD thesis, Technische Universität München, 1998.
- [90] W. Baumjohann and R. A. Treumann. *Basic Space Plasma Physics*. Imperial College Press, 1996.

- [91] B. D. Scott. Nonlinear polarization and dissipative correspondence between low-frequency fluid and gyrofluid equations. *Physics of Plasmas*, 14(10):102318, October 2007.
- [92] A. Hasegawa and K. Mima. Stationary spectrum of strong turbulence in magnetized nonuniform plasma. *Physical Review Letters*, 39(4):205–208, 1977.
- [93] F. F. Chen. *Plasma Physics and Controlled Fusion*. Plenum Press, New York and London, 1984.
- [94] T. Windisch. *Intermittent events and structure propagation in plasma turbulence*. PhD thesis, Ernst-Moritz-Arndt-Universität Greifswald, 2007.
- [95] A. Hasegawa and M. Wakatani. Plasma Edge Turbulence. *Physical Review Letters*, 50(9):682–686, 1983.
- [96] A. Hasegawa and K. Mima. Pseudo-3-dimensional turbulence in magnetized nonuniform plasma. *Physics of Fluids*, 21(1):87–92, 1978.
- [97] V. Naulin, T. Windisch, and O. Grulke. Three-dimensional global fluid simulations of cylindrical magnetized plasmas. *Physics of Plasmas*, 15:012307, 2008.
- [98] P. Terry and W. Horton. Stochasticity and the random phase approximation for 3 electron-drift waves. *Physics of Fluids*, 25(3):491–501, 1982.
- [99] P. Terry and W. Horton. Drift wave turbulence in a low-order K-space. *Physics of Fluids*, 26(1):106–112, 1983.
- [100] Tilman Butz. *Fouriertransformation für Fußgänger*. B.G. Teubner Stuttgart, Leipzig, 2000.
- [101] L. C. Woods. Hydromagnetic waves in a cylindrical plasma. *Journal of Fluid Mechanics*, 13(4):570–586, 1962.
- [102] K. Rahbarnia, S. Ullrich, A. Stark, O. Grulke, and T. Klinger. Alfvén waves in multi-component plasmas. *Journal of Plasma and Fusion Research*, 2008.
- [103] C. Schröder, O. Grulke, T. Klinger, and V. Naulin. Spatial mode structures of electrostatic drift waves in a collisional cylindrical helicon plasma. *Physics of Plasmas*, 11(9):4249–4253, September 2004.
- [104] R. F. Ellis, E. Mardenmarshall, and R. Majeski. Collisional drift instability of a weakly ionized argon plasma. *Plasma Physics and Controlled Fusion*, 22(2):113–131, 1980.

- [105] M. Lesieur. *Turbulence in Fluids*, page 290. Kluwer Academic Publishers, 1997.
- [106] F. Brochard, T. Windisch, O. Grulke, and T. Klinger. Experimental evidence of mode coupling in drift wave intermittent turbulence using a wave number bicoherence analysis. *Physics of Plasmas*, 13(12):122305, 2006.
- [107] F. F. Chen. Resistive overstabilities and anomalous diffusion. *Physics of Fluids*, 8(5):912–919, 1965.
- [108] B. D. Scott. *Low frequency fluid drift turbulence*. Habilitation thesis, Heinrich-Heine Universität Düsseldorf, 2000.
- [109] J. L. Holt, N. C. Luhmann, and J. T. Tang. Measurement of temperature-fluctuations and wave-induced losses associated with Drift-Alfvén instability in a finite-beta-collisional plasma. *Journal of Applied Physics*, 47(10):4467–4474, 1976.
- [110] J. Maggs, T. A. Carter, and R. J. Taylor. Transition from Bohm to classical diffusion due to edge rotation of a cylindrical plasma. *Physics of Plasmas*, 14(5):052507, 2007.
- [111] J. L. Terry, S. J. Zweben, K. Hallatschek, B. La Bombard, R. J. Maqueda, B. Bai, R. W. Boswell, M. Greewald, D. Kopon, W. M. Nevins, C. S. Pitcher, B. N. Rogers, D. P. Stotler, and X. Q. Xu. Observations of the Turbulence in the Scrape-off-Layer of Alcator C-Mod and Comparisons with Simulation. *Physics of Plasmas*, 10(5):1739–1747, 2003.
- [112] A. B. Mikhailovskii and L. I. Rudakov. The stability of a spatially inhomogeneous plasma in a magnetic field. *Soviet Physics JETP-USSR*, 17(3):621–625, 1963.
- [113] A. B. Mikhailovskii. *Theory of Plasma Instabilities*, volume 2: Instabilities of an Inhomogeneous Plasma. Consultants Bureau, 1974.
- [114] B. B. Kadomtsev. Turbulent loss of particles from a discharge in a strong magnetic field. *Soviet Physics — Technical Physics*, 6(10):882–888, 1962.
- [115] L. C. Woods. Plasma instabilities induced by resistivity gradients. *Physics of Fluids*, 6(5):729–736, 1963.
- [116] J. T. Tang, N. C. Luhmann, Y. Nishida, and K. Ishii. Destabilization of hydromagnetic drift-Alfvén waves in a finite-beta, collisional plasma. *Physical Review Letters*, 34(2):70–73, 1975.

- [117] J. T. Tang, N. C. Luhmann, J. Turechek, and D. L. Jassby. Steady-state high-density magnetized arcjet plasma column. *Journal of Applied Physics*, 46(8):3376–3380, 1975.
- [118] J. T. Tang and N. C. Luhmann. Destabilization of hydromagnetic drift-Alfvén waves in a finite pressure, collisional plasma. *Physics of Fluids*, 19(12):1935–1946, 1976.
- [119] R. Hatakeyama, M. Inutake, and T. Akitsu. Observations of broad-band shear Alfvén-wave instabilities. *Physical Review Letters*, 47(3):183–186, 1981.
- [120] G. J. Morales, J. Maggs, A. T. Burke, and J. R. Penano. Alfvénic turbulence associated with density and temperature filaments. *Plasma Physics and Controlled Fusion*, 41:A519–A529, 1999.
- [121] C. Biloiu, E. Scime, X. Sun, and B. Mc Geehan. Scanning internal probe for plasma particle, fluctuation, and LIF tomographic measurements. *Review of Scientific Instruments*, 75(10):4296–4298, 2004.
- [122] X. Sun, C. Biloiu, R. Hardin, and E. Scime. Parallel velocity and temperature of argon ions in an expanding, helicon source driven plasma. *Plasma Sources Science and Technology*, 13(3):DOI 10.1088/0963-0252/13/3/001|PII S0963-0252(04)78818-0, 2004.
- [123] Y. Nishida and K. Ishii. Observation of coupled mode of a collisional drift wave and an Alfvén wave. *Physical Review Letters*, 33(6):352–355, 1974.
- [124] C. Brandt, O. Grulke, and T. Klinger. Comparison of electrostatic and electromagnetic synchronization of drift waves and suppression of drift wave turbulence in a linear device. *Plasma Physics and Controlled Fusion*, 52:055009, 2010.
- [125] W. Gekelman, H. Pfister, Z. Lucky, J. Bamber, D. Leneman, and J. Maggs. Design, construction, and properties of the large plasma research device — the LAPD at UCLA. *Review of Scientific Instruments*, 62(12):2875–2883, 1991.
- [126] C. A. Kletzing, S. R. Bounds, J. Martin-Hiner, W. Gekelman, and C. Mitchell. Measurements of the shear Alfvén wave dispersion for finite perpendicular wave number. *Physical Review Letters*, 90(3):035004, January 2003.
- [127] W. Gekelman, S. Vincena, D. Leneman, and J. Maggs. Laboratory experiments on shear Alfvén waves and their relationship to space plasmas. *Journal of Geophysical Research — Space Physics*, 102(A4):7225–7236, April 1997.

- [128] U. Stroth. *Einführung in die Plasmaphysik*. Institut für Plasmaforschung, Universität Stuttgart, 2007.

# List of Publications

## Refereed Journal Articles

1. K. Rahbarnia, S. Ullrich, K. Sauer, O. Grulke, and T. Klinger, Alfvén wave dispersion behaviour in single- and multicomponent plasmas, *Physics of Plasmas*, **17**: 032102, 2008
2. O. Grulke, S. Ullrich, T. Windisch, and T. Klinger, Laboratory studies of drift waves: nonlinear mode interaction and structure formation in turbulence, *Plasma Phys. Control. Fusion* **49**:B247–B257, 2007
3. N. Sydorenko, O. Grulke, K. Matyash, R. Schneider, S. Ullrich, and T. Klinger, Negative Ions in Helicon Oxygen Discharges, *Contrib. Plasma Phys.* **49**(1): 27–35, 2009

## Conference Articles

1. O. Grulke, S. Ullrich, T. Windisch, and T. Klinger, *Spatiotemporal dynamics of drift wave turbulence in a helicon discharge*, Plasma 2007 **993** (2008) 87-92

## Non-refereed Journal Articles

1. S. Ullrich, H.-J. Hartfuss, M. Hirsch, and H. Laqua, *140GHz Testchamber for stray electron cyclotron radiation*, stellarator news **98** (may 2005) 1-4

## Conference Oral Presentations

1. S. Ullrich, O. Grulke, and T. Klinger, *Nichtlineare Kopplung von Drift- und Alfvénwellen*, Frühjahrstagung der Deutschen Physikalischen Gesellschaft, Darmstadt, Germany, P 6.5 (2008).

## Conference Poster Presentations

1. K. Rahbarnia, S. Ullrich, O. Grulke, and T. Klinger, *Experimentelle Untersuchungen zum Dispersionsverhalten von Alfvénwellen*, Frühjahrstagung der Deutschen Physikalischen Gesellschaft, Greifswald, Germany, P9.5 (2009)
2. K. Rahbarnia, S. Ullrich, O. Grulke, and T. Klinger, *Alfvénwellen in Mehrkomponentenplasmen*, Frühjahrstagung der Deutschen Physikalischen Gesellschaft, Darmstadt, Germany, PIV.7 (2008)
3. S. Ullrich, O. Grulke, and T. Klinger, *Experimentelle Untersuchungen zur Wechselwirkung von Drift- und Alfvénwellen*, Frühjahrstagung der Deutschen Physikalischen Gesellschaft, Düsseldorf, Germany, P16.4 (2007)
4. S. Ullrich, O. Grulke, T. Klinger, and C. Brandt, *Diagnostik zum Nachweis der Drift-Alfvén-Kopplung*, Frühjahrstagung der Deutschen Physikalischen Gesellschaft, Augsburg, Germany, P4.27 (2006)
5. S. Ullrich, S. Cirant, V. Erckmann, F. Gandini, H.-J. Hartfuss, M. Hirsch, and H. Laqua, *ECRH Stray Radiation Material Test Chamber 140GHz*, German-Polish Conference on Diagnostics of Plasmas, Cracow, Poland, PIN120(T10) (2004)
6. S. Ullrich, C. Wilke, R. Kosakov, H. Testrich, *Parameter Ranges for Ionisation-Waves*, Frühjahrstagung der Deutschen Physikalischen Gesellschaft, Kiel, Germany, P17.7 (2003)

### **Eidesstattliche Erklärung**

Hiermit erkläre ich an Eides statt, dass diese Arbeit bisher von mir weder der Mathematisch-Naturwissenschaftlichen Fakultät der Ernst-Moritz-Arndt-Universität Greifswald noch einer anderen wissenschaftlichen Einrichtung zum Zwecke der Promotion eingereicht wurde.

Ferner erkläre ich, dass ich diese Arbeit selbstständig verfasst und keine anderen als die darin angegebenen Hilfsmittel benutzt habe.

Greifswald, im November 2010

---

(Stefan Ullrich)

# Curriculum Vitae

Stefan Ullrich  
Jungstraße 10  
CH-4056 Basel  
Switzerland



Date of birth: 26.09.1978  
Marital status: unmarried

## Professional life

- |                   |  |
|-------------------|--|
| since 04/2010     | Product development group for bipolar devices at ABB Semiconductors, Lenzburg/CH                                       |
| 11/2008 – 03/2010 | Quality assurance engineer at ABB Semiconductors, Lenzburg/CH  |
| 04/2005 – 10/2008 | Doctoral thesis about “Elektromagnetic Drift Waves” at the Max-Planck-Institute for Plasma Physics (IPP) in Greifswald |

## University Education

- |                   |   |
|-------------------|---|
| 03/2004 – 04/2005 | Diploma thesis at the IPP in Garching/Greifswald                |
| 04/2002 – 02/2004 | Continued studies at the University of Greifswald               |
| 10/2000 – 03/2002 | Studies at the Saint Petersburg State University, Russia        |
| 10/1998 – 09/2000 | Foundational studies in Physics at the University of Greifswald |

## School Education

- |                   |  |
|-------------------|--|
| 09/1991 – 06/1997 | Secondary school “Alexander von Humboldt” in Greifswald, grades 7 – 12; finished with school’s honorary “Humboldt” award |
|-------------------|--|

## Extracurricular activities

- |                   |  |
|-------------------|--|
| 05/2005 – 12/2007 | Active collaboration at “Greifswald International Students Festival e. V.”, acoustic and light engineering |
|-------------------|--|

## Acknowledgements

Finally, this thesis is almost about to be printed: time to review the last five years and acknowledge the contributions of the many people who made this possible. After working alone on my diploma thesis, it was a novel experience to join the VINETA-team. I had already been in touch with this group as a student assistant when Thomas Klinger was the group leader. Therefore, I knew I was facing an interesting challenge when Olaf Grulke and Thomas offered me this topic. Since electronic design and development have always been my favorite pastime, I can justly say that the topic of this thesis suited me perfectly. I would like to thank Thomas and Olaf for giving me this opportunity, and for their support during the whole time. As group leader, Olaf managed to motivate me in the right moments, guiding the project from the physical point of view and giving me much freedom in the technical implementation of the proposed experiments. Especially during the writing phase, Olaf spent a lot of his time for detailed feedback, without which I would have ended up with a weird text that would hardly be readable. In the experimental phase, I received great support from the experience of each member of the VINETA group in discussions of physics and other matters. Without diminishing the contributions of the other group members, I want to point out three persons: Most of the Alfvén-wave related experiments were conducted in close cooperation with Kian Rahbarnia, who shared his rich experience with me. Albrecht Stark managed to keep the VINETA-laboratory usable for everyone, which sometimes was a really tough job. Although this included quite painful experiences for me — Hundreds of sorted transistors were simply thrown away! — the benefit of Albrecht's work is obvious when one compares the working conditions with other laboratories. Almost simultaneously, Christian Brandt worked on a similar topic. Although we always competed who would complete his thesis first (he won) we spent a lot of time in fruitful discussions, not only of physics.

I would never have been able to finish this thesis without the continuous help and encouragement from my family and friends. This was essential in at least two situations. About one year after I started, the experimental work became so exhausting that only Katja, my friend and former girlfriend, managed to motivate me and kept me going on. The second hard time was writing-up, a completely new experience for me. Without the great support and motivation of my girlfriend Tanja I probably would have gone mad! Technically, I benefitted from two friends of mine. When the workshop of the institute was not able to prepare parts for my probes since they were too tiny, Sven Grempler did it in his hobby workshop. He first machined a set of adapted tools, which he then used to prepared all the probes I used. Finally, my lector Andreas Schmidt helped me to include the remarks from my supervisors. I am grateful to everybody mentioned — and the many people that remain unnamed.